Estimation of particle size distributions in mineral process systems using acoustic techniques

Francois Swanepoel

January 2000

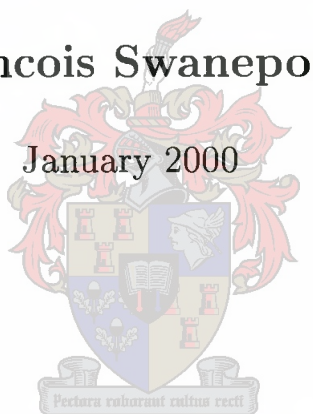

Thesis presented in partial fulfilment
of the requirements for the degree of
Master of Electronic Engineering
at the
University of Stellenbosch

Study Leader: **D.M. Weber**

Declaration

I, the undersigned, hereby declare that the work contained in this thesis is my own original work and has not previously in its entirety or in part been submitted at any university for a degree.

Signature :

Date : January 20, 2000

Abstract

A desire to increase the efficiency of the comminution process in mineral process systems has led to the need of determining the size distribution of ore particles at various stages in the system. The objective of this research is to investigate the feasibility of the use of an acoustic sensor for measuring particle size distribution. The acoustic signal generated when the particles impact on a cantilever bar is analysed using digital signal processing techniques. As rocks fall onto a metal bar, the bar vibrates. The vibrations contain information that is extracted to determine the size of particles that impacted on the bar.

The bar is modelled as a linear system which is excited by impulses (impact of particles). The response of the bar is deconvolved from the acoustic signal to obtain an impulse whose amplitude is proportional to the energy of the impact. In order to improve size estimates, deconvolution is performed using a statistical model of the impulse sequence (Bernoulli-Gaussian) and then estimated using MAP estimation.

Size estimates are not only a function of the mass of particles, but also on the exact position of impact on the bar. Since there is always a variation in the position of impact, size estimates are erroneous. It was found that the position of impact can be determined as to reduce variances dramatically. Due to physical sampling in space, the sensor has a bias towards larger particles. We show how this can be represented mathematically and removed.

This project is mainly concerned with rocks in the +8-25mm (+0,7-22 gram) size range.

Opsomming

Vergruising van erts in die mineraalbedryf verg groot hoeveelhede energie. Daar is 'n behoefte geïdentifiseer om hierdie proses meer effektief te maak. Aangesien die effektiwiteit van 'n meul 'n funksie is van die ertsgroottes wat gemaal word, kan partikel grootte inligting aangewend word om effektiwiteit te bevorder.

Die doel van hierdie tesis is om die lewensvatbaarheid van 'n akoestiese sensor vir die doel van partikelgrootte estimasie, te ondersoek. Erts partikels wat val vanaf 'n vervoerband op 'n kantelbalk, veroorsaak dat die balk vibreer. Deur hierdie vibrasies te meet en verwerk, kan inligting aangaande partikel grootte verkry word.

Die stelsel word gemodelleer as 'n lineêre sisteem met impulse as intree. Die geobserveerde sein is die konvolusie tussen die intree impulse en die impulsweergawe van die sisteem. Deur gebruik te maak van 'n statistiese model en MAP-estimasie, word die effek van die sisteem gedekonvuleer vanaf die geobserveerde sein om 'n benadering van die intree impuls sein te verkry. Die amplitudes van die impulse word gebruik as 'n aanduiding van partikel massa.

Partikelgroottes soos benader deur die stelsel, is 'n funksie van die die posisie waar die partikel die balk tref. Deur van patroonherkenning tegnieke gebruik te maak, word die posisie van impak bepaal om sodoende grootte benaderings aan te pas en die variansie van grootte verspreidings te verminder.

As gevolg van die feit dat partikels gemonster word deurdat slegs 'n klein persentasie van die hele omvang van partikels ondersoek word, onstaan daar 'n oorhelling ("bias") na groter partikels. Die kans dat groter partikels die balk tref is groter as vir klein partikels. 'n Wiskundige model vir hierdie verskynsel word voorgestel en gewys hoe die die oorhelling geneutraliseer kan word.

Hierdie projek het te doen met ertsgroottes +8-25mm (+0,7-22 gram).

Acknowledgements

Many thanks to all the following:

- Dave. A cool boss is a good boss.
- Gunter Metzner and De Beers Consolidated Mines Ltd, for supporting my financial needs.
- And also all the others I don't mention here. I truly appreciate it.

Contents

1 Introduction **1**

1.1 Research Overview 3

1.2 Alternative Techniques 6

1.3 Relevant Concepts to Particle Size Measurements 7

1.3.1 Particle Size Characteristics 7

1.3.2 Particle Size Distributions 8

1.3.3 Statistical Concepts 9

1.3.4 Methods of Data Presentation 12

1.3.5 Instrument Selection 13

1.4 Research Objectives 14

1.5 Contribution 14

1.6 Thesis Outline 15

2 Transducer Dynamics **16**

2.1 Transducer Properties 16

2.1.1 Cantilever Bar Configuration 16

2.1.2 Wave Equation 17

2.2 Bar Vibration Measurement Hardware 21

2.2.1 Strain Gauge Application 22

2.2.2 The Wheatstone Bridge 24

2.2.3 Anti-aliasing Filter 25

2.2.4 Analogue to Digital Converter 26

2.3 Simulations 26

2.4 Summary 27

3 System Modelling **30**

3.1 Representation 30

3.1.1 Sensor Representation 31

3.1.2 Input Signal Representation 32

3.2 Measurement 35

3.3 Estimation 35

3.3.1 Sensor Response Estimation: Autoregressive 36

3.3.2 Model Order Selection 38

3.3.3 Estimating Input Impulse Sequence 41

3.3.3.1 Simple Deconvolution 43

3.3.3.2 Maximum A Posteriori (MAP) Deconvolution 44

3.3.3.3 Principles of Maximum A Posteriori (MAP) Estimation . 45

3.3.3.4 MAP Deconvolution – Application To Particle Size Estimation 46

3.3.3.5 Impact Event Detection 48

3.4 Validation 50

3.5 MAP Amplitude Estimation vs Simple Deconvolution 53

3.6 Summary 58

4 Impact Energy Compensation **59**

4.1 Impact Position Compensation (IPC) 60

4.1.1 Determination of Impact Position 61

4.1.2 Karhunen-Loève Transformation 64

4.1.3 Feature Space Trajectory 64

4.1.4 Theoretical Validation 67

4.2 Height Compensation 67

4.3 Angle Compensation 68

4.4 Summary 70

5 Experiments and Results **71**

5.1 Experimental Setup 71

5.1.1 Experimental Hardware 71

5.1.2 Particle Holding Device 73

5.1.3 Test Particles and Test Procedures 73
5.1.4 Data Acquisition 74
5.2 Relationship Between Particle Size and Impulse Amplitude 74
5.3 Height Compensation 76
5.4 Empirical Results - Round Bar 77
5.4.1 Impact Position Compensation (IPC) 78
5.4.2 Angle of Impact Compensation (AOIC) 79
5.4.3 Particle Size Distribution Estimation 79
5.5 Empirical Results - Square Bar 82
5.5.1 Impact Position Compensation (IPC) 83
5.5.2 Angle of Impact Compensation (AOIC) 83
5.5.3 Particle Size Distribution Estimation 83
5.6 Comparison Between Round and Square Bar Size Estimates 85
5.7 Spike Temporal Resolution 85
5.8 Floating Point Operations 87
5.9 Sampling of Particulate Material 88
5.9.1 Biased Nature of Bar Sampling 93
5.10 Summary 95

6 Conclusions **97**

A Hardware Circuit Diagram **103**

List of Figures

1.1 Particles falling on a metal cantilever bar cause it to vibrate. These vibrations contain information that can be used to estimate the particle size distribution. . . . 3

1.2 The system is modelled as an AR process $H(z)$ with impulses $u(n)$ as input. Observed sequence $x(n)$ is deconvolved with $\hat{H}(z)$ to obtain an estimate $\hat{u}(n)$. Also shown are typical signals at different stages in the system. . . . 4

1.3 Block diagram showing the steps involved during estimation of the size distribution. . . . 5

1.4 Typical histogram of milled particles . . . 10

1.5 Histogram and cumulative plot. . . . 12

2.1 Square and round cantilever bars with strain gauges. . . . 17

2.2 Transverse displacement of a vibrating cantilever bar. . . . 18

2.3 Frequency of the fundamental mode vs. bar length for a square bar with cross-sectional width $a = 14$mm. . . . 19

2.4 Shapes of the first five characteristic functions for a vibrating bar clamped at one end and free at the other . . . 21

2.5 Block diagram illustrating steps involved before sampling the acoustic signal for (a) the vertical component of vibration and (b) the horizontal component. . . . 22

2.6 (a) Cantilever in bending in response to a force generated by the impact of a particle. (b) Strain gauges r_1, r_2, r_3 and r_4 are used in a set to measure strain in the vertical direction. . . . 23

2.7 Wheatstone Bridge with balancing circuitry. . . . 24

2.8 Time sequence and magnitude of the frequency response for simulated data. 28

2.9 Time sequence and magnitude of the frequency response for experimental data. Note from the time signal how the high-frequency components of resonance decay quickly while the fundamental persists for a much longer time. 28

3.1 The bar can be installed to be at an angle α from the horizontal. This will reduce the occurrences of rebounces. 31

3.2 Discrete-time convolutional model. 33

3.3 Filter for generating the random process $x(n)$ from white noise $w(n)$. . . 36

3.4 Normalised error criteria used to determine model order. 41

3.5 Observed signal $x(n)$ is "filtered" to obtain an estimate $\hat{u}(n)$ of $u(n)$. *A priori* information about the system is used to improve estimation results. 42

3.6 Gaussian density for a typical particle size distribution. 50

3.7 Wavelet and generated BG input sequence used for simulations. 51

3.8 Deconvolution results for SNR of 40 dB 54

3.9 Deconvolution results for SNR of 35 dB 55

3.10 Deconvolution results for SNR of 32.5 dB 56

3.11 (top) Simulated BG input signal $u(n)$. (bottom) Absolute errors for MAP estimation and simple deconvolution. The RMS error for simple deconvolution is 16.785 and the RMS error for MAP deconvolution is 2.856. . . . 57

4.1 Diagram of bar showing possible variance in position of impact in x and z dimension. 59

4.2 Normalised particle size estimate vs. impact position along the length of the bar. 61

4.3 Z-plane pole position due to characteristic frequency, w_i. 62

4.4 Amplitude frequency response of cantilever bar vibrations with bar excited at different impact positions. 63

4.5 The second and sixth characteristic functions of a cantilever bar both have a node at $0.77 \times l$ where l is the length of the bar. 63

4.6 2-D representation of reflection coefficients after dimension reduction using KLT. Different colours show different impact positions along the length of the bar. Class positions for dimension 1 vs. 2 are depicted in (a) and (b) shows the positions for dimension 2 vs. 3 66

4.7 3-D feature space trajectory for 11 impact position classes. 66

4.8 3-D feature space trajectory for 11 impact position classes using simulated data. 67

4.9 Overlaid front view for round and square bar with impact angles due to impact position in the x direction. 68

4.10 Vector representation of vertical & horizontal energies. Total impact energy E_r is the vector sum of the vertical and horizontal components. . . 69

4.11 Normalised particle size estimates for both the round bar and square bars. 70

5.1 A photograph of the experimental setup showing a cantilever bar bolted to a wall, the particle holding device and the data acquisition hardware. 72

5.2 The particle holding device consists of an arm with an electromagnet. It enables us to generate accurate experimental results by dropping test particles onto precise locations on the bar. 72

5.3 Particle mass vs. estimated impulse amplitudes. 75

5.4 Estimated impulse amplitudes vs. particle falling height. 76

5.5 Raw impulse amplitude estimates for the round bar vs. position of impact. Vertical component amplitudes are depicted in (a) and horizontal amplitudes in (b). 78

5.6 Round bar particle size estimates after impact position compensation. . . 79

5.7 Round bar particle size estimates after impact position and angle of impact compensation. 79

5.8 Histograms displaying estimated particle size distributions using a round bar. (a) Size distribution using raw data. (b) Size distribution after impact position compensation. (c) Size distribution after combined impact position and angle of impact compensation. 81

5.9 Raw impulse amplitude estimates for the square bar vs. position of impact. Vertical component amplitudes are depicted in (a) and horizontal amplitudes in (b). 82

5.10 Square bar particle size estimates after impact position compensation. . . 83

5.11 Square bar particle size estimates after impact position and angle of impact compensation. 84

5.12 Histograms displaying estimated particle size distributions using a square bar. (a) Size distribution using raw data. (b) Size distribution after impact position compensation. (c) Size distribution after combined impact position and angle of impact compensation. 84

5.13 Three spikes in a time window $\Delta t = 3.6$ms were successfully located by the detector. 86

5.14 The number of FLOPS used for MAP estimation vs. the number of particles in the window for a window length $N = 1000$. The number of FLOPS increases exponentially with the number of particles in the window. . . . 89

5.15 Top view of conveyor belt and cantilever bar underneath it. 91

5.16 Front view of the round bar and particle at the moment of impact at an angle of impact $\theta = 60°$. The effective radius r_{eff} is indicated. 92

5.17 The sensor samples particles with a bias towards larger particles. It has a cubed-root dependence on particle mass. 95

A.1 Schematic diagram for instrumentation amplifier and Wheatstone bridge. 104

A.2 PC board layout for instrumentation amplifier circuit. 105

A.3 Wheatstone bridge connections PC board layout. 105

List of Tables

2.1 Comparison between simulated frequencies and experimental results for the first seven modes of vibration in a steel cantilever bar. Frequencies are given in Hertz. 27

3.1 RMS errors between estimated impulse amplitudes and true amplitudes for different SNR's. 53

5.1 Test particle sizes in gram. 73

5.2 Means and variances of round bar size estimates for raw data, after impact position compensation and after combined impact position and angle of impact compensation. Indicated values are for a uniform particle mass of 19.1g. 81

5.3 Means and variances of square bar size estimates for raw data, after impact position compensation and after combined impact position and angle of impact compensation. Indicated values are for a uniform particle mass of 19.1g. 85

5.4 Means and variances of size estimates for raw data, after impact position compensation and after combined impact position and angle of impact compensation for both the round and square bar. 86

5.5 Number of floating point operations performed during 1 second for different stages of the algorithm. Values correspond to a sampling rate $f_s = 40$kHz with 300 particles per second. 87

Acronyms

AR	Autoregressive
ACF	Auto-correlation function
AOIC	Angle of impact compensation
BG	Bernoulli-Gaussian
DC	Direct current
FFT	Fast Fourier transform
FIR	Finite-duration impulse response
FLOPS	Floating point operations
HPF	High pass filter
IIR	Infinite-duration impulse response
IPC	Impact position compensation
KLT	Karhunen-Loève Transformation
LPF	Low pass filter
LTI	Linear time-invariant
MAP	Maximum *a posteriori*
ML	Maximum-likelihood
MSE	Mean square error
PHD	Particle holding device
PPM	Parts per million
PSD	Power spectrum density
RMS	Root mean square
SNR	Signal-to-noise ratio
WSS	Wide-sense stationary

Notation

AR(p)	Autoregressive process of order p
$x(n)$	Discrete-time sequence
$X(z)$	Z-transform of $x(n)$
p[$\cdot$]	Probability density function of $\cdot$
$\delta(n)$	Unit sample sequence
ln($\cdot$)	Natural logarithm
P[$\cdot$]	$\ln p[\cdot]$
I	Identity matrix
Pr($\cdot$)	Probability of $\cdot$

Chapter 1

Introduction

Metallurgical accounting is an essential feature of all efficient metallurgical operations. Not only is it used to determine the distribution of the various products of a mill, and the values contained in them, but it is also used to control the operations, since values obtained from the accounting procedure are indications of process efficiency.

The current emphasis in metallurgical research is to improve the efficiency of existing processes, optimise their performance, and seek innovative techniques which not only reduce losses, but are more economical [1].

Size analysis of the various products of a mill constitutes a fundamental part of metallurgical accounting. It is of great importance in determining the quality of grinding and in establishing the degree of liberation of the values from the waste rock surrounding ore at various particle sizes. Size analysis of the products is used to determine the optimum size of the feed to the process for maximum efficiency and to determine the size range at which any losses are occurring in the plant [1].

In practice it is essential to carry out the investigation with minimal impact on the plant [2]. Since it is best to minimise manipulation of the sample, an instrument which will measure the distribution directly should be sought. If this is not possible, the method of collecting the sample and presenting it to the instrument must be such that the sample integrity is maintained [3]. It is important that the sample taken must be representative of the entire

batch.

Grinding circuits are notoriously unstable and unwanted fluctuations in particle size, pulp density and volume flow rates can lead to the inefficient use of grinding capacity and to poor extraction of the valuable mineral [4]. According to Stanley [5], the efficiency of the mill depends on the size distribution of particles being ground. For these reasons, it would be beneficial to be able to measure particle sizes on-line.

Particle sizes can be monitored on-line or off-line.

- Off-line measurements abstract a sample of the bulk material. Sampling is the process whereby a small amount of material is taken from the main bulk in such a manner that it is representative of the larger amount. Most automatic samplers operate by moving a collecting device through the material as it falls from a conveyor. The sample is then taken away for analysis in a laboratory. The problems that arise here are the obtaining of a representative sample from the bulk and finding a rapid method of particle size assessment.
- On-line methods analyse directly from the bulk material, thus reducing sampling problems. If only a part of the bulk material is analysed on-line, sampling problems still arise. On-line analysis enables a change of quality to be detected and corrected rapidly and continuously. This method also frees skilled staff for more productive work than testing of routine samples. Being able to present information on a rapid and consistent basis, on-line analysis is the ideal method.

Various image processing techniques have been investigated [6]. However, these methods have not been very successful to date, especially since small irregular particles tend to be obscured by larger ones. The distribution of rocks on a conveyor belt is typically such that there is a thin layer of fine material with a few larger rocks positioned on top of it. Also the high dust content present in a plant makes a vision system problematic since external surfaces like camera lenses get clogged up quickly.

This work is an investigation into the feasibility of making use of acoustic techniques for determining ore particle size distributions.

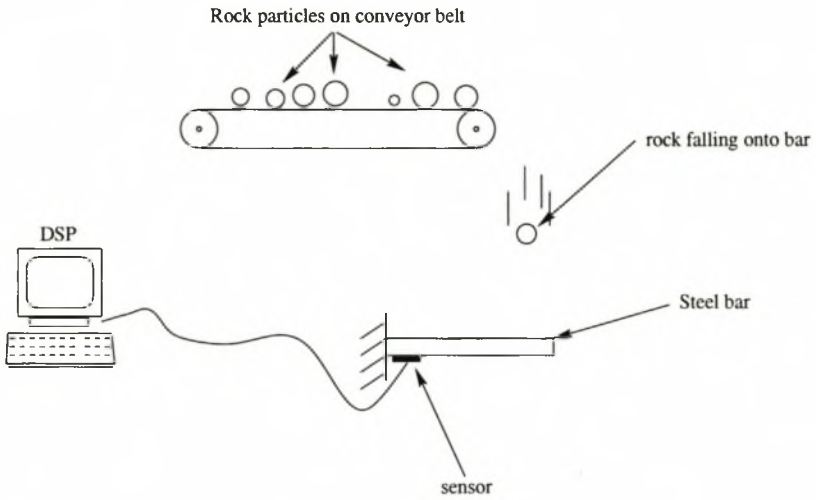

Figure 1.1: Particles falling on a metal cantilever bar cause it to vibrate. These vibrations contain information that can be used to estimate the particle size distribution.

1.1 Research Overview

The aim of this work is to develop a new method for estimating ore particle size distributions for the purpose of control and optimisation of mills. The simplicity and availability of acoustic techniques motivated the idea of investigating the feasibility of using acoustic methods. Much research has been done in the field of acoustics, mainly for speech/speaker recognition and digital communication. Digital processing tools developed for these applications are available and well understood. Also techniques used for reflection seismology[1] are well suited for application to this work.

A schematic diagram of the system can be seen in Figure 1.1. As rocks fall off a conveyor onto a metal cantilever bar, they cause the bar to vibrate. Because of the difference in height between the conveyor and metal bar, the particle has potential energy that is converted to kinetic energy during the fall. At the time of impact, this energy is transferred to the cantilever bar. The amplitude of vibration is proportional to this transferred energy and thus to the size of the particle. An acoustic signal is obtained from strain gauges which

[1]Reflection seismology generates a picture of the subsurface of the earth from surface measurements. Waves reflected at interfaces owing to the impedance mismatches between different geological layers, are recorded by sensors. An image of subsurface reflectors can then be produced.

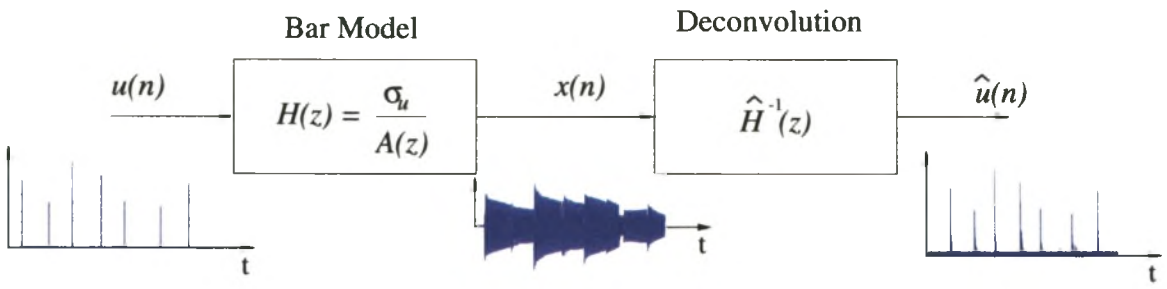

Figure 1.2: The system is modelled as an AR process $H(z)$ with impulses $u(n)$ as input. Observed sequence $x(n)$ is deconvolved with $\hat{H}(z)$ to obtain an estimate $\hat{u}(n)$. Also shown are typical signals at different stages in the system.

measure the deflection of the bar. This signal is processed to determine an estimate of the size of the particle that impacted on the bar.

We begin by modelling the impact of a particle at some point on the bar as an impulse-like function with an amplitude proportional to the energy of the collision. This model is depicted in Figure 1.2. The energy in the collision is directly proportional to the mass of the particle. Assuming a uniform particle density for the bulk material, the mass is then proportional to the size of the particle.

The impact causes the bar to vibrate according to well known principles. If the particles impact on approximately the same part of the bar then the response of the bar to an impact can be modelled as an autoregressive (AR) and thus linear process which is excited by impulses.

The parameters of the AR process can be estimated and used to compute an inverse filter to deconvolve the response of the bar from the observed acoustic signal, $x(n)$. By doing this we obtain an estimate of the input signal $u(n)$. This estimate, $\hat{u}(n)$, consists of impulses separated in time with amplitudes proportional to the mass of the particle.

Although particles are guided to impact more or less on the same part of the bar, near the free end, there will still always be a certain variance present in the exact position of impact. Size estimates are not only a function of the mass of the particle but also of the exact position on the bar where the particle strikes. Any variance in the position of

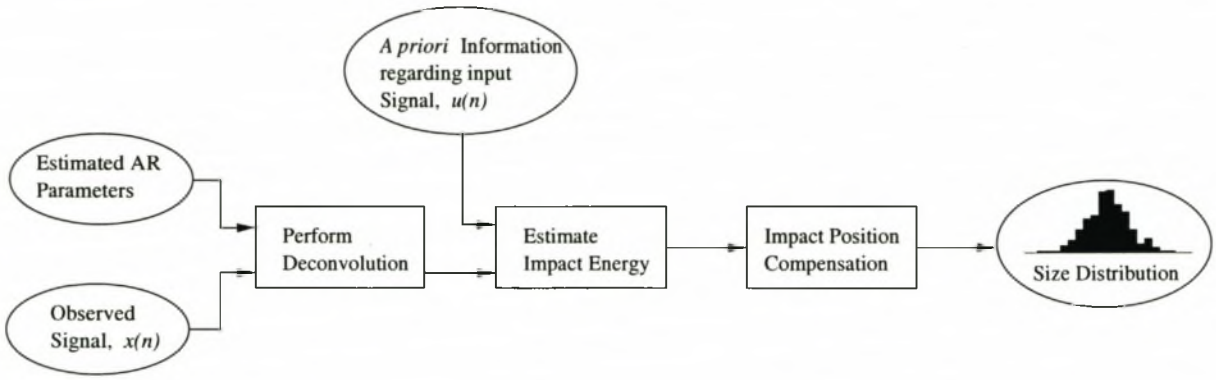

Figure 1.3: Block diagram showing the steps involved during estimation of the size distribution.

impact on the bar will therefore result in erroneous size estimates. Fortunately, additional analysis of the observed signal can reveal the position of impacts. This impact position information can then be used to compensate for size estimates. There are two components to this positional compensation:

1. As shown in Section 4.1 the estimated spike amplitudes are a function of the impact position along the length of the bar. The frequency response of the bar and thus the reflection coefficients, change as the impact position changes. Using the reflection coefficients and pattern recognition techniques the position of impact along the length of the bar can be determined and used to compensate for estimated amplitudes.

2. As many particles may not impact directly on the upper surface of the bar (i.e. a glancing blow), an impact is measured in terms of the vertical and horizontal components of the force of the impact. By using the vertical and horizontal components of the impulse, the angle of impact on the bar can be computed, which allows compensation for impact energy lost due to glancing blows.

The steps involved in determining the size estimates of particles are shown in Figure 1.3. During initially setup the measuring system is calibrated and an estimate of the AR parameters of the bar is obtained. The AR coefficients are used to deconvolve the response of the bar from the observed signal, $x(n)$. Knowing that the input signal $u(n)$ is sparse,

this *a priori* information is used to estimate the energy in the impact of the particle on the bar. The last step is to compensate for any variance in the position of impact on the bar to obtain the distribution of particle sizes.

1.2 Alternative Techniques

Several techniques for determining particle size distributions are currently in use or being investigated [1,3,4,6,7]. A short description of some of the more common methods follows.

Off-line techniques

- Sieving is probably the simplest and most widely used method of determining particle size distributions. It is accomplished by shaking a known weight of sample material successively through finer sieves and weighing the amount collected on each sieve to determine the percentage weight in each size fraction. It covers the approximate size range 5 μm to 125 mm.

- Microscopy is the most direct method for particle size distribution measurements. It is the only method in which individual particles are observed and measured. Its range of applicability is theoretically unlimited. The optical microscope is applicable to particles in the size range 0.8-150 μm, and down to 0.001 μm using electron microscopy.

- Sedimentation techniques utilize the dependence of the terminal velocities of falling particles suspended in a fluid on their size. Particles in the 1 μm to 40 μm size range can be analysed with these methods.

On-line techniques

- Machine vision techniques measure the projected area of particles at the surface of a particle stream with the use of video cameras. A volume distribution has to be estimated from this using a stereological method. A disadvantage of such methods is

that smaller particles tend to be obscured by larger ones. A wide range of sizes can be covered, typically from about 5mm to 500mm.

- Changes in electrolytic resistivity. Particles suspended in an electrolyte, flow through a small aperture having an immersed electrode on each side. As each particle passes through the aperture, it replaces its own volume of electrolyte within the aperture, thus changing the resistance value. This change in resistance has a magnitude proportional to particle volume. Size range: 2 - 100 μm.

- With permeability methods, the size characteristics are inferred from the resistance offered to the flow of a fluid through a packed bed of powder. The flow rate of the fluid is related with particle surface area.

- Adsorption occurs when a solid is exposed to a gas. The gas molecules impinge upon the solid and reside upon the surface for a finite time. The amount of gas adsorbed depends, among other things, upon the nature of the solid. It can be calculated to determine an average particle surface area.

There are many more other techniques available that measure particle size distributions, either falling in the on-line or off-line categories. Normally these methods are concerned with estimating particle sizes for powders or very fine particles and gasses. Also, some of the methods mentioned above under the off-line category, can be configured to obtain a continuous, on-stream estimate of particle sizes.

1.3 Relevant Concepts to Particle Size Measurements

1.3.1 Particle Size Characteristics

The size of a particle, D, is the representative dimension that best describes the degree of comminution of the particle [7]. A spherical homogeneous particle is uniquely defined by its diameter and thus is its size. For a cube the length along one edge is characteristic. With other regular particles, it may be necessary to specify more than one dimension.

The diameter d_j of a particle deviating from spherical symmetry may be defined as any one dimensional distance between two points on the external surface of the particle that intersects the centre of gravity of the particle. The size of any irregular particle is a statistical average of all N of these nonequivalent diameters [7]. Consequently, the size of a given particle depends on the averaging method. Some averaging methods used to obtain a meaningful statistical representative size include:

- Geometric mean of diameters, $D = \left(\prod_{j=1}^{N} d_j\right)^{1/N}$
- Arithmetic mean of diameters, $D = \frac{1}{N}\sum_{j=1}^{N} d_j$
- Harmonic mean of diameters, $D = \left(\frac{1}{N}\sum_{j=1}^{N} \frac{1}{d_j}\right)^{-1}$

Because of the difficulties of describing the shape of a particle it is more usual to define the size of a particle by a single dimension. This can be done by expressing the size of the particle in terms of the diameter of a sphere that is equivalent to the particle with respect to some stated property. Any of the following equivalent spheres may be used for this purpose:

- has the same projected area as the particle when viewed in a direction perpendicular to the plane of greatest stability,
- has the same volume,
- has the same surface area.

In this work we define the equivalent diameter to be the diameter of a sphere having the same volume as the particle. The acoustic sensor we use measures the mass of the particle. Knowing the density of the particles, there is a linear relationship between the mass and the volume of the sphere with equivalent mass.

1.3.2 Particle Size Distributions

A mono-disperse system of particles is composed of the same-sized particles, whereas different-sized particles are found in a poly-disperse particle system. In size measure-

ments on poly-disperse particle systems, the probability that a given particle picked at random has a specified size is measured. Thus the particle sizes reported for any material are associated with their frequency of occurrence. The frequency of occurrence may be reported as the number of particles or as a weight greater than or smaller than a stated size or range of sizes. When the frequency of occurrence of particle sizes is determined by a number, a number-size distribution is obtained.

In a number-size distribution the total number of particles N are classed into I number of class ranges. The result is given as a frequency f_i where there are n_i particles counted in each of the size ranges D_i,

$$f_i = \frac{n_i}{N}. \tag{1.1}$$

The mode of distribution is the value that occurs most frequently. Size distributions having two or more mean sizes are described as heterogeneous (multimodal) distributions. Such a distribution is usually a mixture of two or more homogeneous (unimodal) distributions [7].

1.3.3 Statistical Concepts

It is commonly found that milled products have particle size distributions that obey the log-normal distribution function [3]. When particle size is plotted as a function of the number of times each size occurs, a skew particle size distribution is obtained as shown in Figure 1.4(a).

Particle size distributions are characterised by the parameters that measure the central tendency μ of the distribution, and the variance σ^2 about this central tendency. For the central tendency there are three measures:

1. the average or arithmetic mean,
2. the median,
3. the mode.

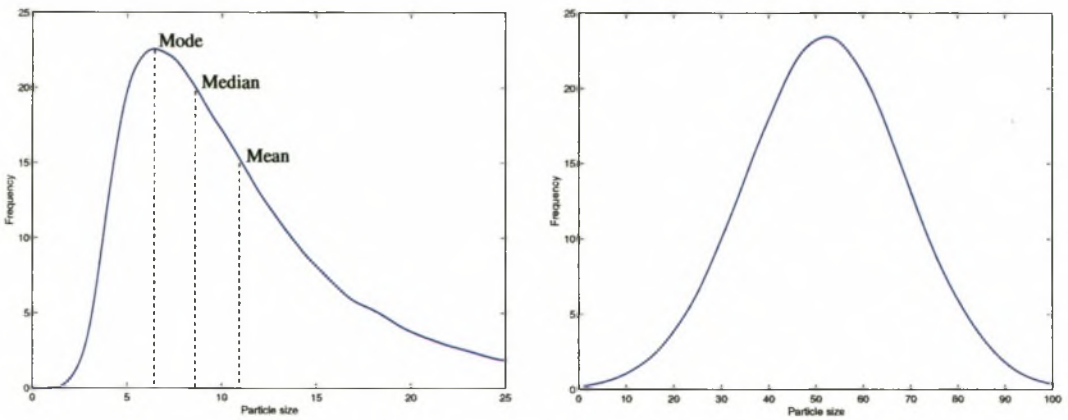

(a) (b)

Figure 1.4: (a) Milled particles typically have a skewed size distribution. (b) A Gaussian like distribution can be obtained be taking the logarithm of the particle size.

The mean is affected by all observed values and thus greatly influenced by extreme values. Therefore the central tendency of a skewed distribution is more adequately represented by the median than the mean.

When a skewed distribution is plotted using the logarithm of the particle size, the asymmetrical curve is transformed into a symmetrical curve. By taking the logarithm of the distribution in Figure 1.4(a) we get the log-normal distribution in Figure 1.4(b). This transformation is important because in this form the distribution is Gaussian like. In the log-normal distribution the mean and median have identical values. Size distributions can then be characterised best by the mean particle size and geometric standard deviation. These two values completely describe the log-normal particle distribution.

In practice few of the distributions found are exactly Gaussian (nor log-normal). Generally the deviations from it are slight and the discrepancies for any distribution with a single hump somewhere near the middle and tailing off to either side are quite negligible [2].

A class of estimators that can be used to obtain a useful estimate of the mean, μ, is known

as L-estimators [8]. They are of the form

$$\hat{\mu} = \sum_{i=1}^{N} a_i x_i, \tag{1.2}$$

where a_i are fixed coefficients and $\mathbf{x} = (x_1, x_2, \ldots, x_N)$ is the random vector of which the "mean" needs to be estimated. Here the random vector is sorted so that $(x_1 \leq x_2 \leq x_3 \leq \ldots \leq x_N)$. By taking $\alpha = j/N$, where $0 \leq j \leq N/2$ is an integer and

$$a_i = \begin{cases} \frac{1}{(1-2\alpha)N}, & \text{if } \alpha N + 1 \leq i \leq N - \alpha N, \\ 0, & \text{otherwise,} \end{cases} \tag{1.3}$$

we get

$$\hat{\mu} = \frac{1}{(1-2\alpha)N} \sum_{i=\alpha N+1}^{N-\alpha N} x_i. \tag{1.4}$$

This is the α-trimmed mean of $\mathbf{x}$ where we simply discard the αN smallest and αN largest observations before estimating the mean in the usual way. Since we ignore the smallest and largest αN observations this method is robust against outliers.

By using $\alpha = 0$, (1.4) gives the sample mean. By taking

$$a_i = \begin{cases} 1, & \text{if } i = k + 1, \\ 0, & \text{otherwise,} \end{cases} \tag{1.5}$$

where $N = 2k + 1$, (1.2) results in the sample median.

The standard deviation is used as the measure of dispersion. It is the root-mean-square deviation about the mean value. As in the α-trimmed mean discussed above, we ignore the αN smallest and αN largest observations to obtain an estimate of the standard deviation that is robust against outliers.

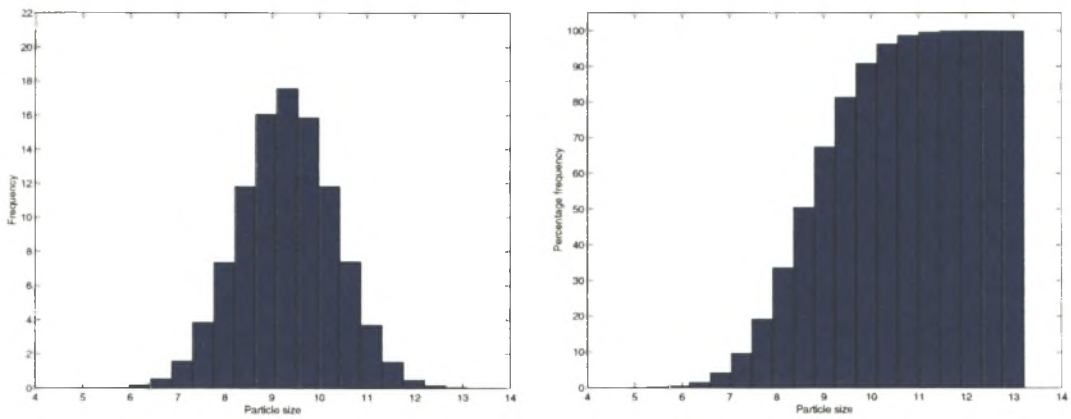

(a) (b)

Figure 1.5: Histogram and cumulative plot.

1.3.4 Methods of Data Presentation

The purpose of a particle size measurement is to discover the true frequency distribution of particle size. Because particle sizes are critical to mining activities, the need for adequate presentation of the data becomes apparent.

Histograms and cumulative plots are the two main forms used for presenting particle size data. Both use one axis to represent particle size and the other axis to represent particle amount. The two differ only in the way the particle "amount" is presented.

The histogram is a bar graph in which the bases of each of the I rectangular bars are the width of the corresponding size classes. An example is shown in Figure 1.5(a). Normally the size classes are of equal width and the area of each bar is proportional to the amount of particles within the size class. More specifically the height of each bar corresponds to the frequency f_i.

The cumulative plot is a continually rising graph which involves plotting the percent of particles less than a given particle size against the particle size (Figure 1.5(b)). The vertical axis in the cumulative plot is usually expressed in terms of percent, with 100% representing the total "amount" of particles in the sample. This method has the advantage that the median size and the percentage between any two sizes may be read off directly.

1.3.5 Instrument Selection

For irregular particles, the assigned size usually depends upon the method of measurement, hence the particle sizing technique should, wherever possible, duplicate the process one wishes to control [4]. The performance of a mill is dependent of the mass of the particles being milled [6]. Thus it would be ideal if the sensor measures the mass of ore particles directly.

There are three basic steps in the selection of an instrument for particle size analysis [3]:

1. Definition of requirements.
2. List the alternative instruments.
3. Select the equipment on the basis of initial cost, time for analysis, degree of automation, and sample size.

The economic evaluation of an instrument must consider the value of the data as well as the cost of obtaining the information.

Other general considerations in the measurement of particles that are not strictly instrument-oriented but are essential to the development of meaningful data, include:

- It is necessary to obtain a representative sample. In general, the instrument will examine only a fraction of the total, thus the sample should be withdrawn to be as representative as possible.
- The manipulations on the sample should be minimised since every operation introduces the opportunity for change in the sample with the attendant bias.

The instrument should have the following properties [9]:

- Must be reliable to reduce plant down-time.
- Production should not be hindered by failure of the instrument.
- Must be sufficiently robust to withstand harsh environmental conditions.

1.4 Research Objectives

The aim of this project is to investigate the feasibility of using acoustic techniques for particle size determination. Specifically, we want to estimate particle sizes by dropping ore particles onto a metal object, in this case a cantilever bar, and use the acoustic signal generated by the vibration of the bar.

A testing system was implemented to empirically determine statistical properties and the bounds of accuracy of the instrument. These characteristics of the instrument are also theoretically determined and validated.

It is attempted to remove as many inherent biases in the instrument. Compensation is performed by scaling size estimates and size estimate distributions to reduce the error in given results.

We indicate application and under which circumstances it will work best. The sensor will only work under specific circumstances of which the size range and the flow rate of particles are the most important.

1.5 Contribution

The feasibility of using an acoustic sensor for determining particle size distributions for use in the mineral industry has been investigated. Research done with this goal in mind has led to the following contributions:

- The design and implementation of a testing system that enables easy generation of accurate experimental data.
- A kernel loadable device driver for the Eagle PC30FS16 analogue to digital sampling card was developed under *Linux* using C++.
- Various software procedures and algorithms were implemented in *Matlab*. These can be used and converted to C++ (even Assembler where necessary) in minimum time to develop an on-line platform.

- Biases introduced by the sensor were pointed out and we showed how to compensate for these.

1.6 Thesis Outline

The next chapter discusses the metal cantilever bar transducer used. Flexural bar vibration is represented using a partial differential equation which resulted from the Bernoulli-Euler beam theory. Hardware used for sampling the analogue signal is also discussed in this chapter.

Chapter 3 is the central part of this work. How the system and various signals are modelled is described. This knowledge is used to perform deconvolution as to obtain an estimate of particle sizes.

Size estimates determined in Chapter 3 are prone to high variances and thus do not provide accurate results. In Chapter 4 we show how these estimates can be improved by determining the position of impact on the bar and then compensating size estimates.

Chapter 5 discusses the experimental configuration and procedures. Experimental results achieved are presented with the effects of various compensation techniques.

Finally, we conclude in Chapter 6 with a summary of work done.

Chapter 2

Transducer Dynamics

The transducer is the (once missing) link between falling particles and a digital acoustic signal. It consists of a metal cantilever bar with attached strain gauges that pick up bar vibration. Bar vibrations due to particle impact contain information regarding the size of the particles. This chapter describes the physical sensor configuration. A theoretical investigation into bar vibration properties is also included. The last part of the chapter discusses simulation results and how these compare to experimental data.

2.1 Transducer Properties

2.1.1 Cantilever Bar Configuration

Figure 2.1 shows the round and square transducers which consist of metal cantilever bars and strain gauges. We investigated the use of cantilever bars with a square cross section and a round cross section. When it comes to angle compensation (Section 4.3) it was found that the round bar results in better size estimates than the square bar.

Figure 2.1(a) shows the square bar with four of the strain gauges shown. These four gauges are used in a full bridge configuration (see Section 2.2.2) to measure vibration in the vertical direction. Not shown here, is another set of four gauges applied to the left and right sides

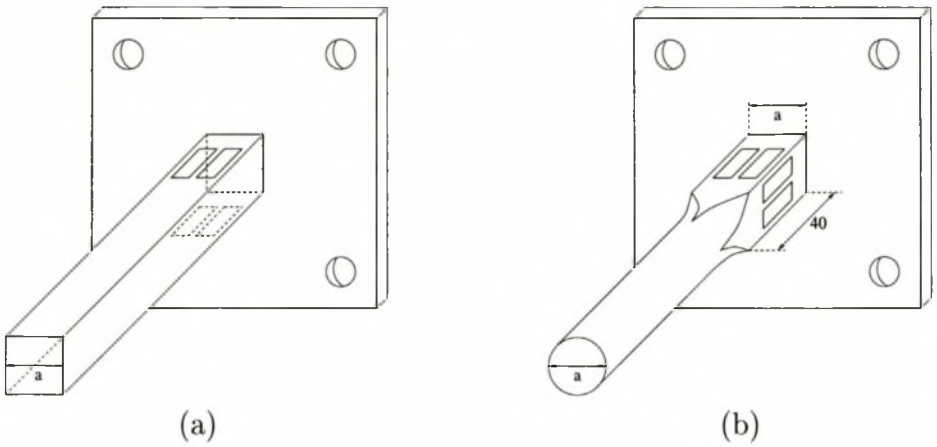

Figure 2.1: (a) Square cantilever bar with strain gauges. Note that for clarity, only the vertical displacement sensing strain gauges are shown. Four gauges are used in a full Wheatstone bridge configuration to measure vibrations in either direction. (b) Round bar showing two of the vertical and two of the horizontal measuring strain gauges.

of the bar in a similar full bridge configuration that measures horizontal vibrations.

The round bar is shown in Figure 2.1(b). The round bar is machined starting off with a square bar with cross sectional side lengths equal to the diameter of the round cross section. As shown, about 40 mm is not machined (i.e. left square) in order to apply the strain gauges in the same way as on the square bar.

2.1.2 Wave Equation

As particles impact on the bar, it bends and starts to vibrate. Figure 2.2 shows the deformation of the bar during bending. We describe the flexural vibrations with the Bernoulli-Euler beam theory [10]. The speed of propagation of the disturbance in the beam is proportional to the frequency so that the higher the frequency the greater the propagation speed [10]. The Bernoulli-Euler model ignores the fact that the propagation speed should obviously have a limit at some frequency. For our purposes this is not a problem though since we are only interested in frequencies under 15kHz which behaviour is similar to the theoretical components described by the model.

The transverse displacement $y(z,t)$ as measured from the horizontal z-axis is a function

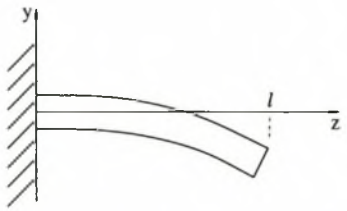

Figure 2.2: Transverse displacement of a vibrating cantilever bar. Note the displacement is not drawn to scale.

of time t and spatial variable z. For a bar of constant cross-section and uniform material properties wave propagation is described by the governing partial differential equation [11],

$$\frac{\partial^4 y}{\partial z^4} = -\frac{\rho}{Q\kappa^2}\frac{\partial^2 y}{\partial t^2}. \tag{2.1}$$

For a bar with a square uniform cross-sectional shape $\kappa = \frac{a}{\sqrt{12}}$ is the radius of gyration with a the width of the cross-section. For a round bar we have $\kappa = \frac{a}{4}$ with a the diameter of the cross-section. Young's modulus Q and the material density ρ are constants determined by the material the bar is made of. For the mild steel bars used, $Q = 20 \times 10^{10}\text{N/m}^2$ and $\rho = 8.15 \times 10^3\text{kg/m}^3$.

Frequencies present in the vibrating bar are determined by the boundary conditions. A cantilever bar of length l is clamped at one end ($z = 0$) and free at the other end ($z = l$). The boundary conditions for this configuration are given by:

$$\begin{aligned} y(0,t) &= 0, \\ \frac{\partial y(0,t)}{\partial z} &= 0, \\ \frac{\partial^2 y(l,t)}{\partial z^2} &= 0, \\ \frac{\partial^3 y(l,t)}{\partial z^3} &= 0. \end{aligned} \tag{2.2}$$

The first two of these equations are straight forward to interpret. For the other two at $z = l$, since there is no bar beyond $z = l$ to cause a moment or a shearing stress there are no bending moment or shearing force.

By assuming a solution for (2.1) of the form $y(z,t) = Y(z)e^{-2j\pi vt}$ and using the boundary conditions (2.2) it is found that the resonant frequencies are given by [11]

$$v_n = \frac{\pi}{2l^2}\sqrt{\frac{Q\kappa^2}{\rho}}\beta_n^2. \tag{2.3}$$

Here $n = 1, 2, 3, \ldots$ are the modes of vibration in the bar. The values of constants β_n are fixed and can be found in [11, p 182]. From (2.3) it is clear that the frequencies present in the bar can be controlled by adjusting the physical dimensions of the bar.

There is an inverse square law relationship between the length of the bar and the frequencies at which the bar resonates. This relation for a square cantilever bar with the width of the cross-section constant at $a = 14$mm, is shown in Figure 2.3. This graph shows the frequency of the fundamental mode vs. bar length. Frequencies of other modes have the same relation at just higher frequencies. The relationship between frequencies present and the cross-sectional width (or diameter for the case of a round bar), is linear. These relationships are taken into account when designing a bar for different particle size ranges. A thicker, longer bar resonates at similar frequencies as a shorter, thinner one.

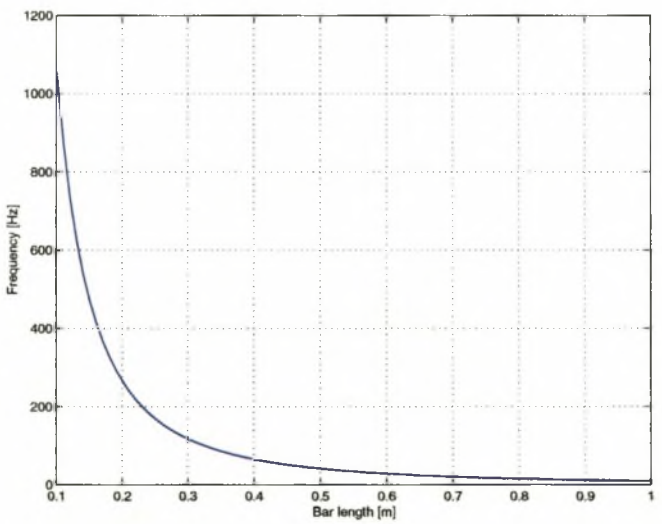

Figure 2.3: Frequency of the fundamental mode vs. bar length for a square bar with cross-sectional width $a = 14$mm.

The characteristic function (mode) corresponding to the allowed frequency v_n is given by the equation

$$\psi_n = a_n \left(\cosh \frac{\pi \beta_n z}{l} - \cos \frac{\pi \beta_n z}{l} \right) + b_n \left(\sinh \frac{\pi \beta_n z}{l} - \sin \frac{\pi \beta_n z}{l} \right), \tag{2.4}$$

where a_n and b_n are constants that can be found in [11, page 183]. The shapes of the first five characteristic functions are shown in Figure 2.4. There is a $1/n^2$ dependence on the amplitudes of the modes and thus the fundamental will dominate with superimposed "ripples" on the fundamental due to higher modes [12]. Although the theoretical solution predicts the presence of these higher frequencies in the motion for all time, observation of the motion would reveal that these components rapidly disappear after two or three oscillations, owing to damping arising from friction [12].

The complete solution for $y(z,t)$ is determined using the initial conditions. Graff [12] says the problem for a falling mass impacting on a beam would represent a complicated interaction problem in which the size of the falling mass in relation to the beam mass, and the degree to which the two bodes would "stick" together due to plastic deformation would all be factors. The approximation of such an impact by an idealised impulse, nevertheless, provides an approximation when the mass of the particle is somewhat less than the beam mass [12]. For the case where a falling particle hits the bar at its free end the impulse force, F, acting on the bar will result in a sudden change in velocity without an appreciable change in its displacement [13]. The initial conditions can be approximated by

$$\begin{aligned} y(z,0) =& y_0(z) = 0, \\ \frac{\partial y(z,0)}{\partial t} =& v_0(z) = \begin{cases} 0 & \text{if } z \neq l, \\ U & \text{if } z = l. \end{cases} \end{aligned} \tag{2.5}$$

Here $U = P/\rho S$ with S the cross-sectional area of the bar and P the total impulse given to the bar [14],

$$P = \Delta p = p_f - p_i = \int_{t_i}^{t_f} F dt. \tag{2.6}$$

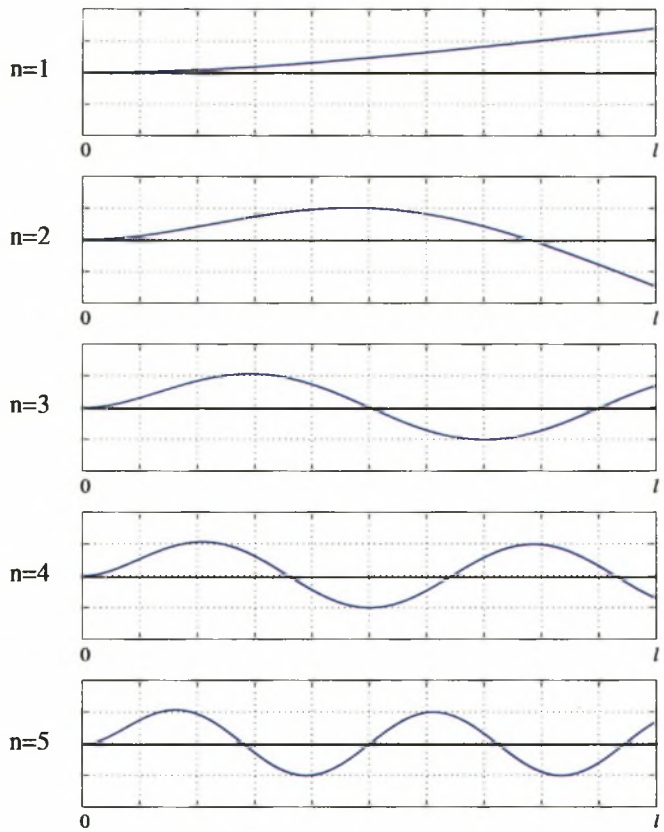

Figure 2.4: Shapes of the first five characteristic functions for a vibrating bar clamped at one end and free at the other

In (2.6) F is the contact force applied to the bar by the falling mass for a small moment of time $\Delta t = t_f - t_i$, and p_f and p_i are the momentum of the particle before and after impact respectively.

2.2 Bar Vibration Measurement Hardware

Strain gauges are used to measure bar vibrations. As mentioned before, vibrations are measured in the vertical and horizontal directions. This two component vibration measurement is depicted in Figure 2.5. Part (a) of the figure shows how vertical bar vibrations are sensed by four strain gauges in a bridge configuration. This signal gets amplified by

an instrumentation amplifier after which it gets filtered before it is sampled and processed. Part (b) shows exactly the same procedure for the horizontal component of vibration. Sections 2.2.1 to 2.2.4 discuss these analogue domain steps in more detail.

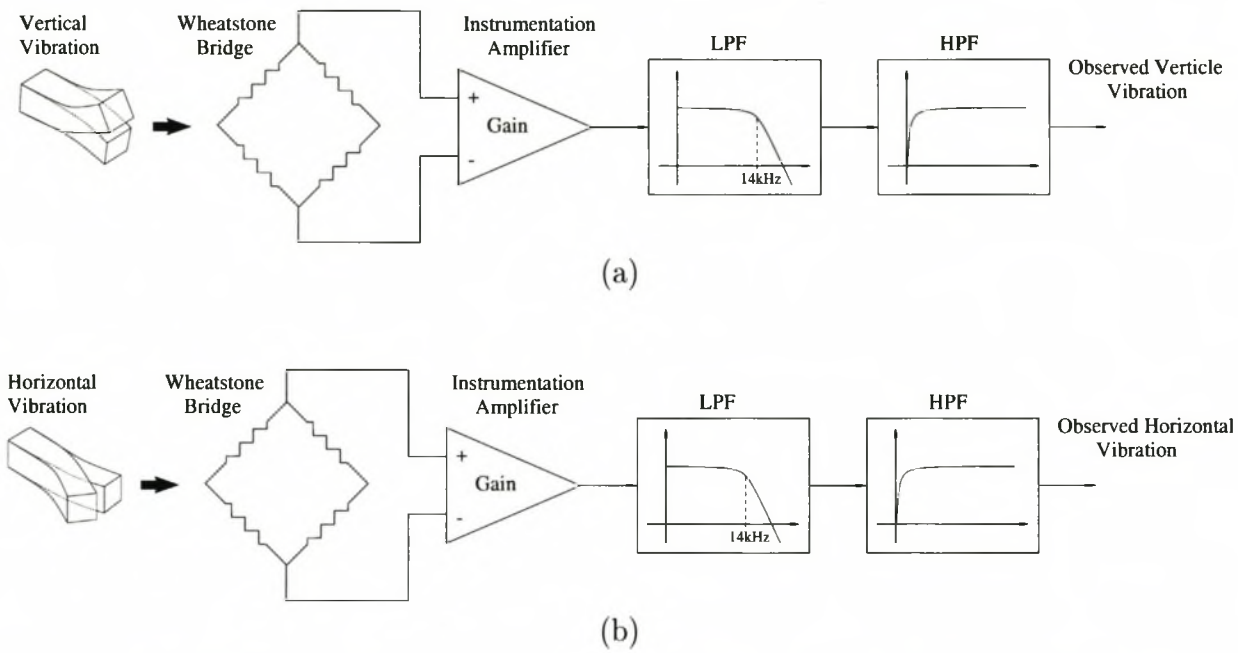

Figure 2.5: Block diagram illustrating steps involved before sampling the acoustic signal for (a) the vertical component of vibration and (b) the horizontal component.

2.2.1 Strain Gauge Application

The deformation caused by a force applied to a body is called strain. Strain is a dimensionless quantity meaning the deformation per unit length $\epsilon = \Delta L/L$. Strain may be either tensile (positive) or compressive (negative). Figure 2.6(a) shows a cantilever bar in bending under applied force F.

The strain gauge is a passive transducer that converts a mechanical displacement into a change of resistance [15]. The gauge is a thin wafer-like device that is attached to measure applied strain. The resistance of the wire in the gauge changes with length as the material to which that gauge is attached undergoes tension or compression. This change in resistance is proportional to the applied strain and is measured with a full Wheatstone bridge (see

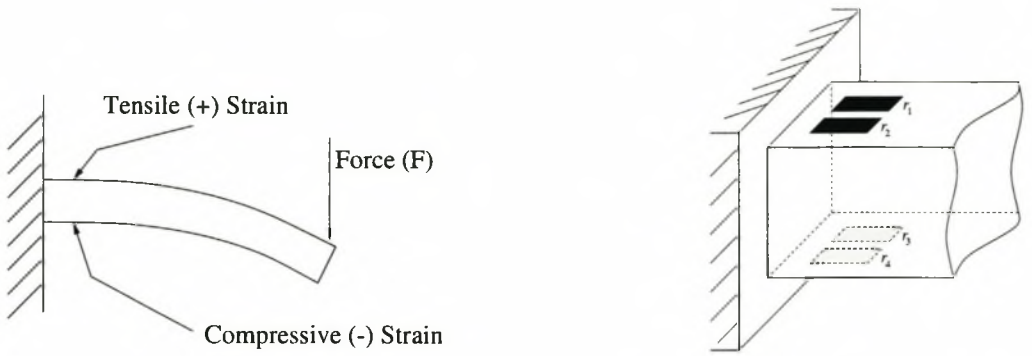

Figure 2.6: (a) Cantilever in bending in response to a force generated by the impact of a particle. (b) Strain gauges r_1, r_2, r_3 and r_4 are used in a set to measure strain in the vertical direction.

Section 2.2.2). The relation between the applied strain ϵ and the relative change of the resistance of a strain gauge is described by [16]

$$\frac{\Delta R}{R_0} = k \times \epsilon. \tag{2.7}$$

The gauge factor k, is a characteristic of the gauge used and is supplied by the manufacturer. It describes the sensitivity of a strain gauge. R_0 is the nominal value of the strain gauge. Strain gauges used were manufactured by *Hottinger Baldwin Messtechnik GMBH*[1], Part No. 1-LY11-6 120A. Nominal resistance $R_0 = 120\Omega \pm 0.35\%$ and gauge factor $k = 2.04 \pm 1\%$ as supplied by HBM.

Strain gauges are applied as close as possible to the end of the bar which is clamped in at $(x = 0)$ as shown in Figure 2.6(b). The reason for this is two fold: strain is a maximum at this point and also the sensors need to be out of the way of falling particles.

[1]Supplied by H. Rohloff (PTY) LTD, P.O. Box 202, Bergvlei 2012, Sandton, South Africa. Tel. (011) 786-3020/5.

2.2.2 The Wheatstone Bridge

The Wheatstone bridge[2] is well suited for the measurement of small changes of a resistance and is therefore suitable to measure the resistance change in a strain gauge [16]. As shown in Figure 2.7 the four arms of the bridge are formed by resistors r_1 to r_4 which correspond to the four strain gauges shown in Figure 2.6(b). Note that the two strain gauges on the upper side of the bar, r_1 and r_2, are electrically connected as opposite arms of the bridge circuit. Similarly the two gauges on the underside of the bar, r_3 and r_4, form the remaining two opposite arms. This is due to the fact that strain values on the upper side and on the underside of the bar are the same but with *opposite sign*, i.e. $\epsilon_1 = \epsilon_2 = -\epsilon_3 = -\epsilon_4 = \epsilon$. Connecting the pairs as opposite arms in the bridge results in the addition of strain values measured by all four strain gauges.

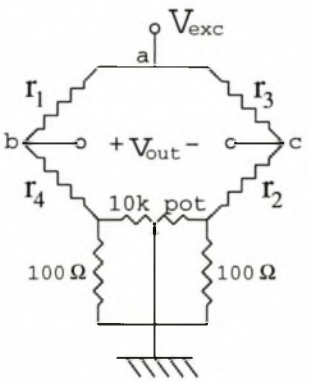

Figure 2.7: Wheatstone Bridge with balancing circuitry.

The bridge is excited by a constant DC voltage V_{exc}. The bridge excitation voltage level affects both the output sensitivity and the gauge self heating [17]. From the measurement standpoint a high excitation level is desirable but a lower level reduces gauge self heating.

We use four strain gauges all with the same nominal value r. This ensures that the relative changes of the individual bridge arms are proportional to the relative variation of the output voltage V_{out}. The ratio between the output voltage and the excitation voltage for

[2]Named after the English physicist Sir Charles Wheatstone (1802-1875).

a cantilever bar as depicted in Figure 2.6(b) can be shown to be [16]

$$\frac{V_{out}}{V_{exc}} = k \times |\epsilon|, \tag{2.8}$$

where ϵ is the strain measured by each strain gauge and k is the gauge factor. Since V_{out} is very small, typically in the μV range, an instrumentation amplifier is used to amplify this differential output voltage to a signal between $\pm$5V. An instrumentation amplifier is a committed gain block that amplifies a differential input voltage by a precisely set gain [18]. Since the bridge output should not be loaded, instrumentation amplifiers are designed to have very high input impedance. Voltages common to both inputs are rejected. The circuit diagram and PC board layout for the instrumentation amplifiers are in Appendix A.

The combination of the potentiometer and the two fixed resistors shown in Figure 2.7 is used to balance the bridge during setup.

A set of four strain gauges as described in this section, is used to measure vibration in the vertical plane. As noted earlier, there is also a set of four gauges on the right and left side of the bar. This allows measurement of bar vibration in both the horizontal and vertical planes. The total signal is thus a vector comprising the horizontal and vertical acoustic components. This will be discussed in detail in Section 4.3.

2.2.3 Anti-aliasing Filter

In order to prevent aliasing, a 14th order Butterworth [19] low pass filter (LPF) is used at the output of the instrumentation amplifier. We used a filter designed by Bellingan [20] with a cut off frequency at 14 kHz. Details of this design can be found in [20].

As mentioned in Section 2.2.2, the Wheatstone bridge is balanced to produce a zero voltage output when the bar is at rest. However, due to temperature and other variations there is always a small drift in the output voltage resulting in a DC offset. To be able to make use of the full dynamic range of the analogue to digital converter, the LPF is followed by a passive high pass filter (HPF). This filter removes the DC offset that may be present in

the signal.

2.2.4 Analogue to Digital Converter

Software development for this project was done using *Matlab* on a personal computer running Linux. The acoustic signal generated by the strain gauges is converted to digital using an analogue to digital converter card, PC30FS16, from *Eagle Technology*[3]. Using this card, up to 16 channels can be sampled simultaneously with 12 bit precision. Since we observe two components of bar vibration, we use 2 channels per sensor. The details of how experiments were performed are discussed in Section 5.1.

Only software for the Windows operating system was provided by the manufacturer of the analogue to digital card. Software in the form of a kernel loadable module device driver for Linux [21] was developed by Carl Bellingan and myself. By using this modular approach it is easy to add support for the new device without patching the kernel source.

2.3 Simulations

Wave equations as described in Section 2.1.2 were implemented to simulate bar behaviour. For validation purposes these bar simulations could then be compared to empirical data.

The bar used in this experiment is a square cantilever bar with dimensions 14mm×14mm×300mm. Young's modulus $Q = 20 \times 10^{10}\text{N/m}^2$ and material density $\rho = 8.15 \times 10^3\text{kg/m}^3$ were used for simulation purposes. Because of the low pass anti-aliasing filter used at the output of the sensors (discussed in Section 2.2.3), only the first seven modes of vibration ($n = 1, 2, 3, \ldots, 7$) are present in the observed signal. For this reason simulation results also only include the first seven modes. AR estimation of order 64 is used resulting in 32 positive frequencies that will be estimated. The reason for using a model order of 64 will become clear in Section 3.3.2.

[3]P.O. Box 4376, Cape Town, 8000, Tel. (021) 234 943.

Mode	1	2	3	4	5	6	7
Theory	117	734	2,055	4,028	6,658	9,946	13,891
AR, simulated	122	723	2,053	4,027	6,674	9,946	13,886
AR, experiment	121	735	2,140	4,276	6,730	9,756	12,889

Table 2.1: Comparison between simulated frequencies and experimental results for the first seven modes of vibration in a steel cantilever bar. Frequencies are given in Hertz.

Table 2.1 shows the comparison between theoretically determined frequencies for each mode, using (2.3), and estimated frequencies using AR estimation for both simulated bar vibrations and experimental data. Only the seven positive frequencies corresponding to poles closest to the unit circle are shown. From this table it is clear that the experimental configuration matches theory very closely. Observed frequency modes are extremely close to the ones predicted by theory.

The good correlation between the theory and practical results is further emphasised in Figures 2.8 and 2.9. Figure 2.8 shows the simulated bar response over a 0.025 second time period after impact with the corresponding magnitude frequency response using the AR spectral estimator of order 64. Figure 2.9 is a similar plot for real data from the experimental bar setup. The peaks in the frequency response correspond to bar resonances shown in Table 2.1. Visual inspection of these two figures reveals the accuracy of the theoretical approximation[4].

2.4 Summary

This chapter described how a two component digital signal is obtained resulting from bar oscillations. Two sets of four strain gauges each are configured in a full Wheatstone bridge. The differential signal is amplified using an instrumentation amplifier. An anti-aliasing LPF in combination with a HPF is used to filter data before it is sampled by

[4]From the time signal in Figure 2.9 it can be seen how quickly high-frequency components of resonance disappear. This is similar to a tuning fork where the high-frequency overtones are damped out rapidly and the harsh initial sound will quickly change to a pure tone due to the fundamental!

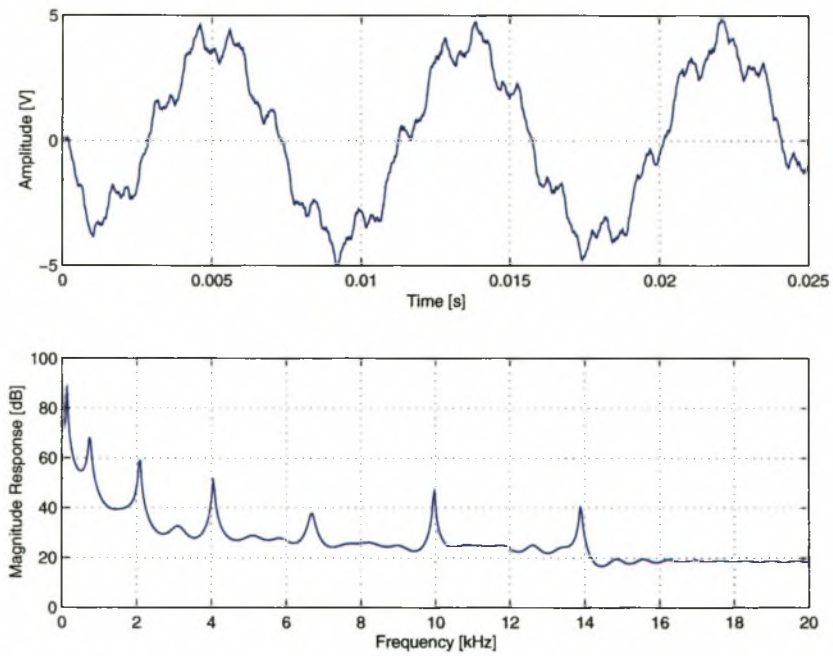

Figure 2.8: Time sequence and magnitude of the frequency response for simulated data.

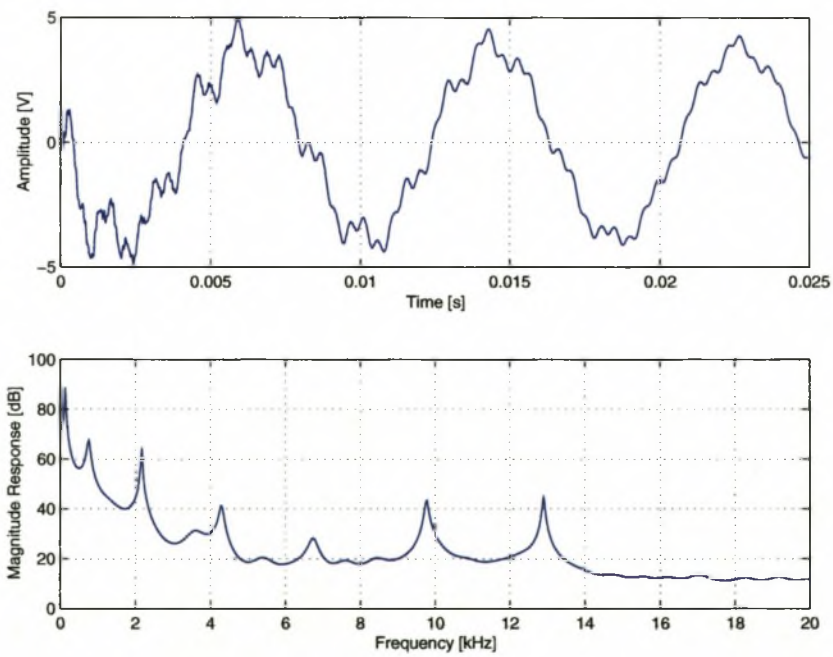

Figure 2.9: Time sequence and magnitude of the frequency response for experimental data. Note from the time signal how the high-frequency components of resonance decay quickly while the fundamental persists for a much longer time.

an analogue to digital converter. Equations describing wave propagation in a cantilever bar were presented. It was shown that experimental data very closely match theoretical results.

Chapter 3

System Modelling

"A model is a more or less idealised representation of an often complex reality" [22]. Modelling the system consists of obtaining a mathematical description of all the internal components in the system and how they interact. The three main components are the input signal $u(n)$, the bar response $h(n)$ and the observed signal $x(n)$. Using $x(n)$ we want to find $u(n)$. Since we do not know $h(n)$, this is not a trivial task. As a matter of fact, it is impossible to determine $u(n)$ exactly. Fortunately, we are able to get an estimate $\hat{h}(n)$ of $h(n)$. Using this and other *a priori* information about the system we can get a good estimate $\hat{u}(n)$ of the input signal $u(n)$.

Mendel [23] suggests that system modelling is decomposed into four subproblems: representation, measurement, estimation and validation. This chapter deals with these four subproblems in detail.

3.1 Representation

Representation deals with how something should be modelled. This is normally in the form of a mathematical description of the system. We need an equation that describes the following sensor: *A metal cantilever bar of dimension (x,y,z) vibrates when hit by an ore particle. From the observed vibration determine ore particle size.*

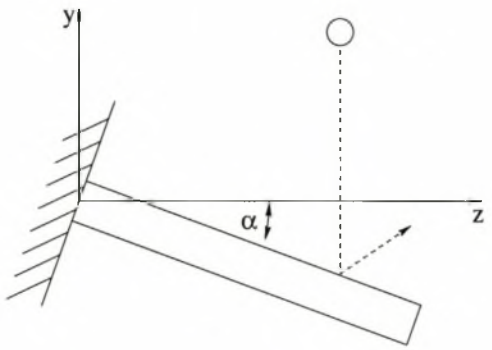

Figure 3.1: The bar can be installed to be at an angle α from the horizontal. This will reduce the occurrences of rebounces.

There are two aspects of the system that are represented independently of each other. The first one being representation of the sensor and the second representation of the input signal. Representation of these two components are discussed in the following two sections.

3.1.1 Sensor Representation

A cantilever bar vibrates according to well known principles. Wave propagation in a bar involves one spatial variable z as can be seen from the governing partial differential wave equation (2.1) which is repeated here for convenience,

$$\frac{\partial^4 y}{\partial z^4} = -\frac{\rho}{Q\kappa^2}\frac{\partial^2 y}{\partial t^2}. \tag{3.1}$$

The wave equation is an *internal* representation describing the physics of the system.

A physical consideration that has to be taken into account is the possibility of a particle bouncing straight up off the bar and then bouncing back onto the bar a second time. This "rebouncing" is clearly undesirable. The second impact will be much smaller than the first with the result that it will not represent the true particle size. This problem can be reduced by mounting the cantilever bar at an angle α as shown in Figure 3.1. The law of reflection states that the angle of reflection equals the angle of incidence as measured from the normal constructed to a reflecting surface [14]. With the bar at an angle, most of

the particles *should* bounce off directly. The author proposes that there is still, albeit very small, a possibility that a rebounce may occur. Unfortunately there is nothing that can be done to compensate once a rebounce has happened. Typically the incorrectly estimated particle size for the rebounce is about three times smaller than that of the first correct impact. Thus, the occurrence of a rebounce does not pose any serious problems since it will result in an outlier that can easily be discarded using nonlinear filtering techniques (L-filtering).

If the system can adequately be represented by a lossless wave equation with impulses as inputs, the observed output will be time-delayed scaled replicas of the system impulse response [24]. This leads to the one-dimensional convolutional model

$$x(t) = u(t) * h(t), \tag{3.2}$$

where $h(t)$ is the impulse response of the system, $u(t)$ is the system input and $x(t)$ the observed output. Here $*$ is used to denote the operation of convolution. This time-series model is an *external* representation. It does not retain any of the physics associated with the internal wave motion that produces $x(t)$.

Equation (3.2) can be discretized and additive noise included to obtain an approximated discrete-time convolutional model

$$x(n) = u(n) * h(n) + e(n). \tag{3.3}$$

A graphical representation of (3.3) is depicted in Figure 3.2.

3.1.2 Input Signal Representation

We model the impact of a particle at some point on the bar as an impulse-like function with an amplitude proportional to the energy of the collision. It will be shown in Section 3.3.3.1

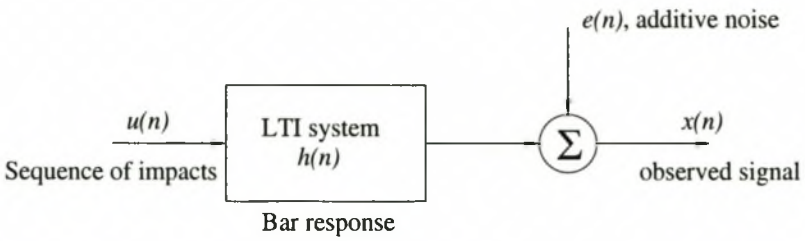

Figure 3.2: Discrete-time convolutional model.

that simple deconvolution[1] provides poor amplitude estimates. This is due to noise present in the observed signal. Fortunately we can improve amplitude estimates by making use of some *a priori* information regarding $u(n)$.

Consider particles falling down a conveyer onto the bar. Because of the narrow width of the bar, the particles can be seen as being in single file. This leads to the natural choice for $u(n)$ to be represented by an impulse train where the temporal locations and amplitudes of impacts are random. An impulse train is a sequence consisting of impulses with random amplitudes at random instances of time while the rest of the time series equals zero and is given by

$$u(n) = \sum_{i=0}^{\infty} a_i \delta(n - t_i). \tag{3.4}$$

Here a_i are the random amplitudes and t_i the random positions in time when the impulses occur.

When only a small part of the components of $u(n)$ are non-zero, the sequence is referred to as a *sparse* impulse train. A non-zero component corresponds to the event where a particle impacts on the bar where the amplitude of the impulse is related to the particle size.

A Gaussian process has non-zero values at all samples and is not a realistic model for our situation. Under a certain distributional assumption the process $u(n)$ can be described by the Bernoulli-Gaussian (BG) distribution [25]. By definition, the BG distribution has

[1]Simple deconvolution is the process where we compute an inverse filter and convolve this with the input signal. The alternative that we use is MAP deconvolution.

independent components. Each component is zero with probability $(1 - \lambda)$ and non-zero with probability λ. Given that the component is non-zero it is sampled from a Gaussian distribution. For small λ the BG distribution will clearly produce sparse realizations, whereas it approaches the Gaussian for λ close to 1 [26].

The BG process can be represented as the product of two statistically independent random sequences [26]:

$$u(n) = q(n)r(n), \tag{3.5}$$

a Bernoulli[2] event sequence, $q(n)$, and a white Gaussian amplitude sequence, $r(n)$. The Bernoulli sequence, which is a random sequence of zeros and ones, locates the time events when particles impact. A value of unity indicates an impact occurred while at all other time points it equals zero. The sparsity of $q(n)$ is determined by the density parameter λ so that

$$\begin{aligned} Pr[q(k) = 1] &= \lambda, \\ Pr[q(k) = 0] &= 1 - \lambda. \end{aligned} \tag{3.6}$$

The Gaussian sequence $r(n)$ represents the amplitudes of the impacts at the time events occur.

With this model it is possible to separate the problems of determining when an impact event occurs from what the amplitude of that event is.

The problem of a rebounce was explained in Section 3.1. This can be accounted for by modelling the input as

$$\begin{aligned} u_{true}(n) &= u(n) + u_{rb}(n), \\ &= q(n)r(n) + u_{rb}(n). \end{aligned} \tag{3.7}$$

Here the sequence $u_{rb}(n)$ accounts for the smaller event that occurs when a particle re-

[2]After the Swiss mathematician Jacob Bernoulli (1654–1705).

bounces. It is "convolutional noise" since, because of the distributive property of convolution, the observed signal now not only contains $u(n) * h(n)$, but also $u_{rb}(n) * h(n)$. The inclusion of $u_{rb}(n)$ in effect raises the threshold level of the detector algorithm discussed in Section 3.3.3.5 so that only significant amplitudes are detected.

3.2 Measurement

The only physical signal that can be observed is $x(n)$, the acoustic signal at the output of the strain gauges. This signal is used to firstly estimate the parameters of the system function $H(z)$ and secondly to estimate the input signal $u(n)$.

Because of the on-line requirement of particle size data, the estimation of $u(n)$ has to be done in real time. Estimation of the system parameters is done off-line during initial setup.

3.3 Estimation

The estimation subproblem is the important one which deals with the determination of those quantities that cannot be measured directly from the observed signal. The internal system parameters have to be estimated and used in the deconvolution process of estimating the external system input. This is the heart of the entire system as can be seen from (3.3). Only a good estimate of $h(n)$ can result in an approximation of $u(n)$ which is accurate enough to be able to supply particle size data within given tolerance.

Estimation is closely related to inverse modelling in which a model is determined which could have given rise to observed effects. Similar to the system representation in Section 3.1, there are also two components to the estimation problem. These are the estimation of $h(n)$ and the deconvolution of $x(n)$ to obtain an estimate of $u(n)$.

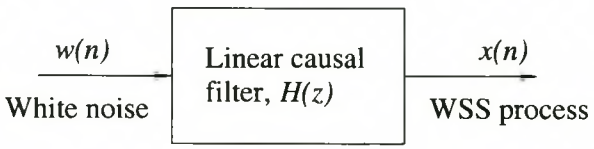

Figure 3.3: Filter for generating the random process $x(n)$ from white noise $w(n)$.

3.3.1 Sensor Response Estimation: Autoregressive

As noted in Section 2.1.2, the bar exhibits several modes at which it resonates. Such resonant behaviour is accurately modelled as a process with poles located at the resonant frequencies of the sensor. Numerous techniques for estimating theses poles exist [27–29]. This prior knowledge of the sensor's dynamics allows for more accurate estimates of the characteristics of the sensor.

A wide-sense stationary random process can be represented as the output of a causal and causally invertible linear system excited by a white noise process [27]. This representation of the process $x(n)$ as the output of a filter with system function $H(z)$ is known as the Wold representation. Figure 3.3 shows the filter for generating $x(n)$ from white noise $w(n)$.

The linear filter $H(z)$ for generating the random process $x(n)$ from the white noise process $w(n)$ is a rational function which can be expressed as

$$H(z) = \frac{B(z)}{A(z)} = \frac{\sum_{k=0}^{q} b_k z^{-k}}{1 + \sum_{k=1}^{p} a_k z^{-k}}, \tag{3.8}$$

where b_k and a_k are the filter coefficients that determine the location of the zeros and poles of $H(z)$, respectively. This general model is termed an autoregressive-moving average (ARMA) model.

By setting all the b_k coefficients, except $b_0 = 1$, equal to zero, we effectively model a process containing poles only. In this case the measured data sequence $x(n)$ is modelled as the output of a linear time-invariant recursive system described by a difference equation with

an input driving sequence $u(n)$,

$$x(n) = -\sum_{k=1}^{p} a_k x(n-k) + u(n). \tag{3.9}$$

This is a purely recursive system where the output is a weighted linear combination of p past outputs and the present input. Such a model is termed an autoregressive model of order p, AR(p), and can be represented as

$$H(z) = \frac{\sigma_u}{A(z)} = \frac{\sigma_u}{1 + \sum_{k=1}^{p} a_k z^{-k}}, \tag{3.10}$$

where $a_1, a_2, \ldots a_p$ are the AR parameters for the process and σ_u^2 is the energy in the system input signal, $u(n)$. The power spectral density (PSD) of the output AR process is

$$P_{AR}(f) = \sigma_u^2 \left| \frac{1}{A(f)} \right|^2, \tag{3.11}$$

where $A(f)$ is $A(z)$ evaluated along the unit circle $z = \exp(j2\pi f)$ for $-\frac{1}{2} \leq f \leq \frac{1}{2}$ [27].

The AR model is suitable for modelling the bar because of the following reasons:

1. A theorem due to Kolmogorov (1941) asserts that any ARMA or moving average (MA) process can be represented by an AR model of possibly infinite order [28].

2. An AR process is suitable for representing spectra with narrow peaks. It is known that the vibrating bar generates poles at certain positions in the z-plane corresponding to the characteristic frequencies (2.3).

3. The AR model results in a simple representation of the dynamics of the bar.

The AR parameters of the process can be estimated from $x(n)$ by a number of methods [27–29]. For this work, the autocorrelation method in conjunction with the Yule-Walker equations were used. Given the auto-correlation function (ACF), the Yule-Walker

equations define a linear relationship between the ACF and the AR model parameters [28]

$$r_{xx}(k) = \begin{cases} -\sum_{l=1}^{p} a(l) r_{xx}(k-l), & \text{for } k \geq 1\ , \\ -\sum_{l=1}^{p} a(l) r_{xx}(-l) + \sigma_u^2, & \text{for } k = 0, \\ r_{xx}^*(-k), & \text{for } k < 0. \end{cases} \tag{3.12}$$

We use a biased estimate of the ACF

$$r_{xx}(m) = \frac{1}{N} \sum_{n=0}^{N-m-1} x^*(n) x(n+m), \qquad m \geq 0, \tag{3.13}$$

in (3.12) to estimate the AR coefficients. This ensures a stable AR model which implies that the inverse filter $H^{-1}(z)$ will be minimum-phase [27]. The Levinson-Durbin algorithm is a computationally efficient recursive algorithm which is used to solve the Yule-Walker equations (3.12) for $a_1, a_2, \ldots a_p$ and σ_u^2.

The AR parameters need only be calculated each time the bar is calibrated and can thus be done off-line.

3.3.2 Model Order Selection

Ideally the output $x(n)$ can be measured using a linear measuring device and system function $H(z)$ is purely determined by the response of the bar. In practice however the measuring device has a system response $H_m(z)$ and thus the total system function $H(z)$ is the product of $H_b(z)$ and $H_m(z)$, the response of the bar and measuring device respectively,

$$H(z) = H_b(z) H_m(z). \tag{3.14}$$

As discussed in Section 2.2.3 a low-pass Butterworth filter was used to prevent aliasing. This filter has a cutoff frequency of 14kHz and only the first seven modes of vibration as given by (2.3), $n = 1, 2, \ldots, 7$, are present in the observed signal $x(n)$. Thus, there will be 14 complex conjugate poles due to the bar response $H_b(z)$.

The combination of the instrumentation amplifier, Wheatstone bridge, anti-aliasing filter and analogue to digital converter determines the number of poles that will be present in $H_m(z)$. Thus we do not know directly the model order of $H_m(z)$. However, the measuring devices and anti-aliasing filter contribute at least 50 poles. Because of the unknown number of poles, an estimation of this must be made.

Much work have been done on the criteria for model order selection [28, 30, 31]. Four of the more common criteria are discussed below.

Prediction Error Power - PEP

The Levinson-Durbin algorithm recursively calculates the AR parameters and prediction error power ρ, which is identical to the excitation noise variance σ_u^2 [28]. If the system is an AR(p) process and we guess it is of order k, with $k = p + 1$, then $a_p(j) = a_k(j)$ for $j = 1, 2, \ldots, p$ and $a_k(k) = 0$ [28]. Here $a_p(j)$ is the j'th AR parameter for a model estimate of order p. This means that the first p AR parameters of an estimate of order greater than p will be equal to the AR estimate of order p and the rest will be zero.

The recursion formula for the prediction error power is derived in [28, p 170] and is given by

$$\rho_k = (1 - |a_k(k)|^2)\rho_{k-1}. \tag{3.15}$$

Hence, with $a_k(k) = 0$ for $k > p$, the prediction error power is a constant for a model order equal to or greater than the true model order. It would therefore be a good assumption to choose the model order to be the one at which ρ does not change.

Final Prediction Error - FPE

Akaike [30] proposed a criteria called the Final Prediction Error (FPE) criterion where the order p is selected to minimise the performance index

$$FPE(p) = \rho\left(\frac{N+p+1}{N-p-1}\right). \tag{3.16}$$

Akaike Information Criterion - AIC

A second criterion proposed by Akaike [30] is called the Akaike Information Criterion (AIC). It is based on selecting the order p that minimises

$$AIC(p) = \ln(\rho) + 2p/N. \tag{3.17}$$

Minimises the Description Length - MDL

Rissanen [31] based a criterion on selecting the order p that minimises the description length (MDL) where MDL is defined as

$$MDL(p) = N\ln(\rho) + p(\ln N). \tag{3.18}$$

Above mentioned criteria were implemented and applied to empirical data. The results are shown in Figure 3.4. It is a plot showing the four normalised error criteria that need to be minimised to determine the model order. Different symbols are used to distinguish between the four lines as indicated by the legend. From this figure it is clear that all four criteria suggest a model order between 60 and 70. It was decided to model the system as AR(64), i.e. using a model order $p = 64$.

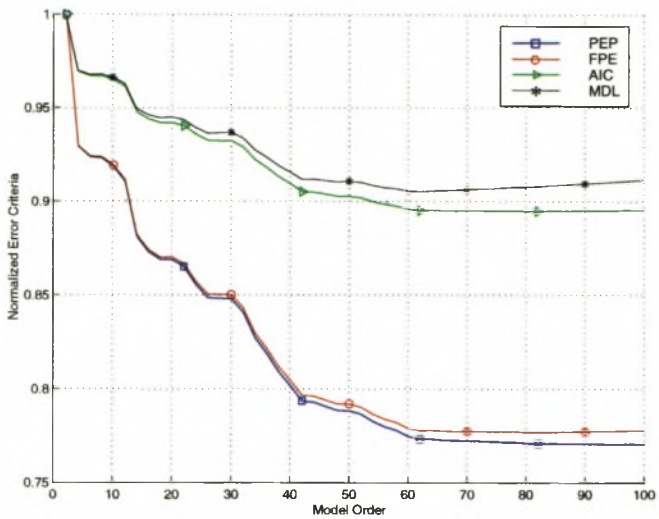

Figure 3.4: Normalised error criteria used to determine model order.

3.3.3 Estimating Input Impulse Sequence

Whereas convolution allows us to determine the output of LTI systems to any given arbitrary input signal, deconvolution is the inverse process. The term "deconvolution" is used to describe the operation of separating the input signal from the characteristics of the system. It is the process of separating two convolved signals and is used to estimate a desired signal $u(n)$ which is observed through a linearly degraded and noisy version $x(n)$. Deconvolution attempts to remove various undesired aspects of the raw data. One such undesired aspect is the duration of the system impulse response, resulting in overlapping and interference between the signals caused by two separate events or impacts. Another undesirability is the ever present noise in the observed signal.

The linear time-invariant system takes as input the signal $u(n)$ and produces an output signal $x(n)$, which is the convolution of $u(n)$ with the unit sample response $h(n)$ of the

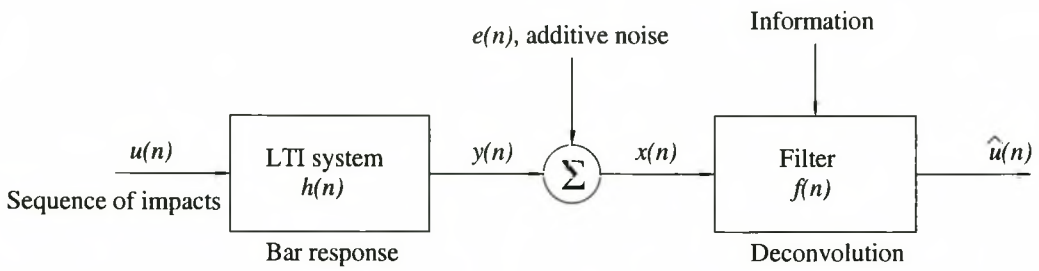

Figure 3.5: Observed signal $x(n)$ is "filtered" to obtain an estimate $\hat{u}(n)$ of $u(n)$. *A priori* information about the system is used to improve estimation results.

system,

$$\begin{aligned} x(n) &= u(n) * h(n) + e(n), \\ &= \sum_{k=0}^{n} h(n-k)u(k) + e(n). \end{aligned} \tag{3.19}$$

This situation is again depicted in Figure 3.5 but here the deconvolution filter $f(n)$ is shown. We "filter" $x(n)$ to obtain the best possible estimate $\hat{u}(n)$ of $u(n)$,

$$\begin{aligned} \hat{u}(n) &= f(n) * x(n), \\ &= \sum_{i=0}^{N-1} f(i)x(n-i), \end{aligned} \tag{3.20}$$

where $f(i)$ denotes the N filter coefficients of the inverse filter. The optimum, in the least-squares sense, FIR filter that satisfies (3.20) is called a Wiener[3] filter. *A priori* information regarding system parameters is used to improve estimation. This information can be knowledge about statistical properties of the input or noise variances.

[3]Named after the famous mathematician Norbert Wiener who introduced optimum least-squares filtering methods in engineering.

3.3.3.1 Simple Deconvolution

By determining the inverse system response and convolving this with $x(n)$ the input signal can be found. In the z-domain, (3.19) translates to

$$X(z) = U(z)H(z), \tag{3.21}$$

where $X(z)$, $H(z)$ and $U(z)$ are the z-transforms of $x(n)$, $h(n)$ and $u(n)$ respectively. In (3.21) the additive noise is ignored. In Section 3.3.1 the system function between the input and the output of the process was shown to be the rational function

$$H(z) = \frac{\sigma_u}{A(z)}. \tag{3.22}$$

The inverse system function is given by

$$F(z) = H^{-1}(z) = \frac{A(z)}{\sigma_u}, \tag{3.23}$$

where $F(z)$ is the z-transform of the inverse filter $f(n)$. The zeros of $H(z)$ become the poles of the inverse system, and vice versa. If $H(z)$ is an all-pole system, then $F(z)$ is an all-zero and thus a finite-duration impulse response (FIR) system.

Substituting (3.19) for $x(n)$ into (3.20) and taking the z-transform result in

$$\begin{aligned} \hat{U}(z) &= F(z)X(z), \\ &= F(z)\left(U(z)H(z) + E(z)\right). \end{aligned} \tag{3.24}$$

In the ideal situation when $F(z)H(z) = 1$, (3.24) simplifies to

$$\begin{aligned} \hat{U}(z) &= U(z) + F(z)E(z), \\ &= U(z) + E(z)/H(z). \end{aligned} \tag{3.25}$$

Transforming $\hat{U}(z)$ back into the time domain gives an estimate $u_{sd}(n)$ for $u(n)$.

In practice this method of inverse filtering gives large variations in the solution even with very small variations in the input. The reason is that the system has a narrow-band structure with H(z) close to zero at some frequencies. Any noise at these frequencies will be blown up by the division in (3.25). This makes the deconvolution problem ill-posed.

Statistical methods have proven efficient in removing the ill-posedness by introducing additional information in the form of a stochastic model. A method which works effectively for sparse impulse trains is discussed in the following section.

3.3.3.2 Maximum A Posteriori (MAP) Deconvolution

It is known *a priori* that the impulse train to be estimated is sparse. By sparse we mean only a limited number of randomly located samples are non-zero. This information can be used to improve estimation. A common solution is to quantify *a priori* knowledge about sparsity by a statistical model and use a maximum *a posteriori* (MAP) estimator for reconstruction.

It was shown in Section 3.1.2 how $u(n)$ can be represented as a BG process. It is convenient to represent the BG process by two $(M \times 1)$ vectors; $\mathbf{t}$ giving the positions of the non-zero components and $\mathbf{a}$ giving their amplitudes. The relationship between $u(n)$, $\mathbf{a}$ and $\mathbf{t}$ is given in (3.4). If we know the number of impulses present in the signal, (3.4) becomes

$$u(n) = \sum_{i=1}^{M} a_i \delta(n - t_i), \tag{3.26}$$

with M the number of impulses and

$$\mathbf{a} = [a_1, a_2, a_3, \ldots, a_M]',$$
$$\mathbf{t} = [t_1, t_2, t_3, \ldots, t_M]'.$$

By inserting (3.26) in (3.19) the convolutional model can be written as

$$x(n) = \sum_{i=1}^{M} a_i h(n - t_i) + e(n), \qquad n = 1, 2, 3, \ldots, N \tag{3.27}$$

with N the length of the observed signal. In matrix form (3.27) becomes

$$\mathbf{x} = \mathbf{Ha} + \mathbf{e}, \tag{3.28}$$

where

$$\mathbf{x} = [x_1, x_2, x_3, \ldots, x_N]',$$
$$\mathbf{e} = [e_1, e_2, e_3, \ldots, e_N]'.$$

$\mathbf{H}$ is of size $(N \times M)$ and depends on $\mathbf{t}$. Its elements are given by $H_{ni} = h(n - t_i)$ for $n = 1, 2, \ldots, N$ and $i = 1, 2, \ldots, M$. Thus, each column of $\mathbf{H}$ contains a copy of the system impulse response, $h(n)$, that is shifted to the corresponding impulse position.

In the following two sections, we explain MAP deconvolution and how the system representation in (3.28) is used to achieve this.

3.3.3.3 Principles of Maximum A Posteriori (MAP) Estimation

Consider a vector of unknown parameters Φ that describe a collection of N independent identically distributed observations $x(n)$ collected in an $(N \times 1)$ vector $\mathbf{x}$. The *a posterior* conditional joint probability density function $p(\Phi|\mathbf{x})$ is given by Bayes' Theorem[4] [32] as

$$p(\Phi|\mathbf{x}) = \frac{p(\mathbf{x}|\Phi)p(\Phi)}{p(\mathbf{x})}, \tag{3.29}$$

in which $p(\Phi)$ is the *a priori* probability density function for Φ and $p(\mathbf{x}|\Phi)$ is the probability density function of the observations $\mathbf{x}$ given the parameters Φ. Since $p(\mathbf{x})$ does not depend

[4]The theorem is named for Thomas Bayes (1702–1761), an English theologian and mathematician.

on Φ,

$$p(\Phi|\mathbf{x}) \propto p(\mathbf{x}|\Phi)p(\Phi). \tag{3.30}$$

The MAP estimate $\hat{\Phi}$ is the value of Φ that maximises (3.30) for a particular set of measurements $\mathbf{x}$[5]. Because the random nature of Φ are accounted for by means of $p(\Phi)$, MAP estimation is also known as *unconditional* maximum-likelihood (ML) estimation [26].

3.3.3.4 MAP Deconvolution – Application To Particle Size Estimation

As mentioned before, the purpose of deconvolution is to estimate a desired signal $u(n)$ which is observed through a linearly degraded and noisy version $x(n)$. From (3.26) and (3.28) it can be seen that this is identical to estimating $\mathbf{a}$ and $\mathbf{t}$. Our parameter vector Φ is therefore of the form

$$\begin{aligned} \Phi &= [\mathbf{a}, \mathbf{t}]', \\ &= [a_1, a_2, \ldots, a_M, t_1, t_2, \ldots, t_M]'. \end{aligned} \tag{3.31}$$

Substituting (3.31) into (3.30) gives [25],

$$p(\mathbf{a}, \mathbf{t}|\mathbf{x}) \propto p(\mathbf{x}|\mathbf{a}, \mathbf{t})p(\mathbf{a}|\mathbf{t})p(\mathbf{t}). \tag{3.32}$$

The MAP estimate is the values of $\mathbf{a}$ and $\mathbf{t}$ that maximises the *a posteriori* probability density $p(\mathbf{a}, \mathbf{t}|\mathbf{x})$. This is obtained by specifying $p(\mathbf{x}|\mathbf{a}, \mathbf{t}), p(\mathbf{a}|\mathbf{t})$ and $p(\mathbf{t})$ and maximising (3.32). To do this we state the following distributional assumptions:

- The noise $\mathbf{e}$ is zero mean Gaussian and white, independent of $\mathbf{a}$ and $\mathbf{t}$, and has variance σ_e^2.
- Amplitude vector $\mathbf{a}$ is sampled from a white Gaussian process with variance σ_a^2.

[5]MAP estimation is similar to maximum-likelihood (ML) estimation where values of Φ are found that maximise the likelihood $l(\Phi|\mathbf{x}) \propto p(\mathbf{x}|\Phi)$ [26]. The only difference between MAP and ML methods is $p(\Phi)$ in (3.30). If the random nature of Φ is known *a priori* it makes sense to rather use a MAP estimator.

- Vectors $\mathbf{a}$ and $\mathbf{t}$ are statistically independent.

Maximisation with respect to $\mathbf{a}$ for fixed $\mathbf{t}$ only requires a linear least squares fit, while maximisation with respect to $\mathbf{t}$ is a difficult combinatorial search problem. For this reason we maximise (3.32) for $\mathbf{a}$ assuming $\mathbf{t}$ is known. Estimation of $\mathbf{t}$ (i.e. the impulse positions), which is a detection problem, is discussed in Section 3.3.3.5.

Vectors $\mathbf{a}$ and $\mathbf{e}$ are jointly Gaussian and a linear transformation of Gaussian random variables (3.28) produces other Gaussian random variables [32, p 149]. This implies that $\mathbf{x}$ is Gaussian, which except for constant factors, can be written as [25]

$$p(\mathbf{x}|\mathbf{a},\mathbf{t}) \propto \exp\left\{\frac{\mathbf{a}'\mathbf{H}'\mathbf{H}\mathbf{a} - 2\mathbf{x}'\mathbf{H}\mathbf{a}}{-2\sigma_e^2}\right\}. \tag{3.33}$$

Assuming $\mathbf{a}$ to be zero-mean the prior distribution of $\mathbf{a}$ given $\mathbf{t}$ is [25]

$$p(\mathbf{a}|\mathbf{t}) = (2\pi\sigma_a^2)^{-M/2} \exp\left\{\frac{\mathbf{a}'\mathbf{a}}{-2\sigma_a^2}\right\}. \tag{3.34}$$

Because we are working with exponential densities, it is convenient to take the logarithm of (3.32) to obtain the log-posterior density $P(\mathbf{a},\mathbf{t}|\mathbf{x})$ given by

$$P(\mathbf{a},\mathbf{t}|\mathbf{x}) = \ln p(\mathbf{a},\mathbf{t}|\mathbf{x}) = \ln p(\mathbf{x}|\mathbf{a},\mathbf{t}) + \ln p(\mathbf{a}|\mathbf{t}) + \ln p(\mathbf{t}) + c, \tag{3.35}$$

where $\ln(\cdot)$ denotes the natural logarithm and c is a constant. Since the logarithm is a monotonically increasing transformation, maximising (3.35) is equivalent to maximising (3.32).

Define

$$\begin{aligned} \mathbf{S} &= \mathbf{H}'\mathbf{H} + \gamma\mathbf{I}, \\ \mathbf{v} &= \mathbf{H}'\mathbf{x}, \\ \gamma &= \sigma_e^2/\sigma_a^2, \end{aligned} \tag{3.36}$$

and substitute (3.33), (3.34) and (3.36) into (3.35) to get after reorganising [25]:

$$\begin{aligned} \ln p(\mathbf{a}, \mathbf{t}|\mathbf{x}) &= \frac{(\mathbf{a} - \mathbf{S}^{-1}\mathbf{v})'\mathbf{S}(\mathbf{a} - \mathbf{S}^{-1}\mathbf{v})}{-2\sigma_e^2} + \frac{\mathbf{v}'\mathbf{S}^{-1}\mathbf{v}}{2\sigma_e^2} \\ &\quad - M/2 \ln(2\pi\sigma_a^2) + \ln p(\mathbf{t}) + c. \end{aligned} \tag{3.37}$$

Only the first term on the right side of (3.37) is dependent on $\mathbf{a}$. Thus, by maximising it we can reach our goal of obtaining the MAP estimate. Because the denominator is negative, this is achieved by minimising $(\mathbf{a} - \mathbf{S}^{-1}\mathbf{v})'\mathbf{S}(\mathbf{a} - \mathbf{S}^{-1}\mathbf{v})$. Since $\mathbf{S}$ is positive definite symmetric [25], it can be seen that the maximising value of $\mathbf{a}$ is

$$\hat{\mathbf{a}} = \mathbf{S}^{-1}\mathbf{v}. \tag{3.38}$$

$\mathbf{S}$ is full rank (it is positive definite), so that (3.38) has a unique solution [28]. A computationally efficient method known as the *Cholesky decomposition* may be used to solve (3.38) [28, p 29]. This method involves the decomposition of $\mathbf{S}$ into the product of a lower triangular matrix $\mathbf{L}$ and a diagonal matrix $\mathbf{D}$. A two stage back-substitution recursion is then employed to yield $\hat{\mathbf{a}}$ in an efficient manner.

3.3.3.5 Impact Event Detection

We need to estimate when in time did the impact events occur, i.e. we have to determine the elements of vector $\mathbf{t}$ or equivalently $q(n)$ which was defined in (3.5). There is no simple solution to obtain $q(n)$ [26]. In principle, the MAP estimate $\hat{q}(n)$ could be determined by trying all the finite number of possible combinations for $q(n)$. Since $q(n)$ is a binary sequence, there is 2^N possible combinations. Clearly this would be computationally prohibitive for realistic signal sizes.

Several techniques to obtain a suboptimal $\hat{q}(n)$ for a Bernoulli-Gaussian process have been proposed in the literature. Some of them include: Viterbi algorithm [33], Single-Most-Likely-Replacement (SMLR) algorithm [26] and Iterated Window Maximisation (IWM) [25]. These methods involve iterative or recursive deterministic searches where

only changes that increase the posterior are accepted. For each new $\hat{q}(n)$ value the amplitudes must be refitted which is computationally expensive and thus not suitable for on-line measurement systems.

It was mentioned in Section 3.3.3.1 that simple deconvolution does not provide good impulse amplitude estimates in the presence of noise, however, it was found that by using simple deconvolution the positions in time when the impulses occur, are clearly resolved. This led to the natural choice of using a threshold detector on $u_{sd}(n)$, the output after performing simple deconvolution. If $u_{sd}(n)$ is above a certain threshold, γ, we assign a value of 1 to $q(n)$. Elements of $q(n)$ corresponding to values of $u_{sd}(n)$ below γ are set equal to zero. Detection results in a very good estimate of vector $\mathbf{T}$. This is due to the fact that particle sizes have a non-zero mean and thus with reasonable signal-to-noise ratios, impulses caused by impact events are well above the noise floor.

In choosing a value for the threshold, γ, we make use of *a priori* information regarding what we are estimating; particle sizes. One thing that is very definite about particle sizes is that they just can *not* be negative[6]. An assumption we make is that particle sizes has a Gaussian distribution, centered around the mean a_{size} with variance σ^2_{size}. Although this is not entirely true, the Gaussian assumption is accurate enough in the region we are interested in (around the mean).

Figure 3.6 shows the Gaussian density that we assume typical particle size distributions have. With given mean and variance (a_{size} and σ^2_{size}) we decide on a threshold γ that will enable us to locate say 95% of all impulses that impact on the bar. We use a square-law detector where u^2_{sd} is compared to γ^2. This thresholding step is followed by an intelligent algorithm that resolves separate events. In essence this is achieved by estimating the envelope u_{env} of u^2_{sd}. Distinct "hills" are formed that are mapped onto u^2_{sd} to find the maximum value $u_{sd,max}$ under each hill. These maximum values correspond to events in time that were resolved by the detector.

[6]We can gladly accept this as fact, since all particles with negative mass flew off the planet soon after its formation.

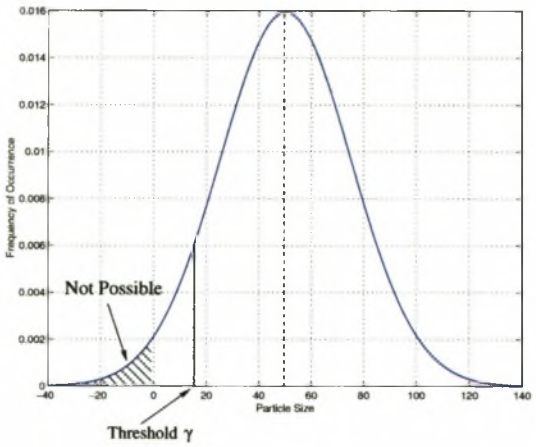

Figure 3.6: Gaussian density for a typical particle size distribution.

3.4 Validation

Once $\hat{u}_k$ is obtained, how do we know it is correct? This is a question we need to answer to ensure that the proposed model is indeed an accurate one.

One way of doing this is to compare particle size distribution estimates to known particle sizes that were used to generate the data. In Chapter 5 we show experimental results and that we are able to estimate particle size distributions with high accuracy. By dropping a single particle many times from a fixed height onto the bar we should ideally get a distribution that consists of a single delta function. Because of estimation errors the measured distribution will be Gaussian, again with a certain mean and variance. The narrower we can get this variance, the more accurate are our estimates.

In this section we validate our assumptions using synthetic data according to the block diagram shown in Figure 3.5. A Bernoulli-Gaussian input signal $u(n)$ is generated and then convolved with the wavelet $h(n)$ shown in Figure 3.7(a) to obtain $y(n)$. Noise $e(n)$ with variance σ_e^2 is added to obtain a simulated observed signal $x(n)$ with signal-to-noise ratio (SNR)[7] fixed at 40, 35 and 32.5 dB. The input sequence $u(n)$ (Figure 3.7(b)) is a BG sequence with $\lambda = 0.01$ and the amplitudes are Gaussian distributed with mean 50

[7]The SNR is defined as the ratio of mean power of noise free signal $y(n)$ to noise variance σ_e^2.

and variance 20. With a sampling rate of $f_s = 40kHz$, this corresponds to 400 impact events per second. An observed signal $x(n)$ corresponding to a SNR of 40 dB is shown in Figure 3.7(c).

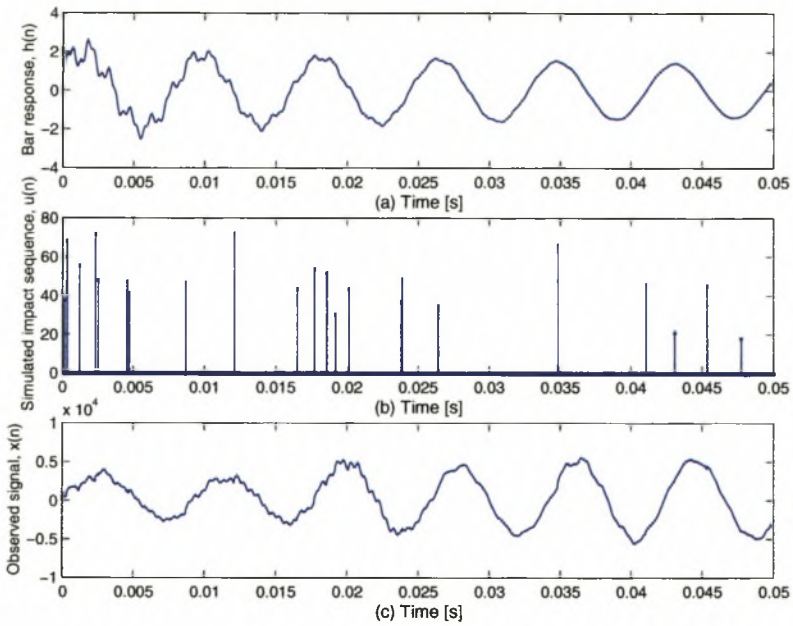

Figure 3.7: (a) Bar response wavelet $h(n)$ used for simulations. (b) Input BG sequence $u(n)$ with amplitude mean 50 and variance 20. (c) Observed signal $x(n)$ for SNR of 40 dB.

Figures 3.8 to 3.10 show the deconvolved results corresponding to SNR of 40, 35, and 32.5 dB respectively. In order to get a better perception of achieved results, these plots are zoomed in and only show deconvolved outputs for the duration $\Delta t = 15$ to 27.5 milliseconds. There are eight impact events that need to be resolved in this time frame. Top plots are simple deconvolution outputs that are used by the detector algorithm discussed in Section 3.3.3.5. The detector used a threshold of $\gamma = 20$. The crosses indicate impulses that were detected. Bottom plots show MAP amplitude estimates as well as the true values. Bars depict estimates and circles depict true values.

Results depicted in Figures 3.8 to 3.10 are discussed in the following three paragraphs:

- Figure 3.8 (SNR = 40 dB): A comparison between the top and bottom plot reveals that all eight impulses are well above the noise-floor and are correctly located by

the detector. MAP estimated amplitudes depicted by bars in the bottom plot correspond well to true values indicated by circles. The RMS error between true impulse amplitudes and estimated amplitudes is 1.765. The only obvious estimation errors correspond to the sixth and seventh impulses. Seeing that these two events are not well separated in time (only 75 μs between them[8]) the estimated amplitude values for them are acceptable.

- Figure 3.9 (SNR = 35 dB): All eight impulses are again above the noise-floor but an additional 8 "impulses" are detected as indicated by the crosses in the top plot. It is clear from the bottom plot that these 8 false-alarms are suppressed to small values well under the threshold and can easily be discarded. The amplitude estimates of the correctly detected impulses are again very satisfactory. The RMS error after thresholding the false-alarms is 2.693. The only estimates that differ substantially from true values are again those of impulse numbers six and seven.

- Figure 3.10 (SNR = 32.5 dB): This scenario is very similar to the one in Figure 3.9. Once again all eighth true impulses are correctly detected, and estimated amplitudes for these are still satisfactory (RMS error is 5.727). The crosses in the top plot indicate that the detector found about 50 impulses, of which only 8 are correct. Fortunately the MAP amplitude estimator suppresses these false-alarms to small positive and negative values. The main problem with so many false-alarms is that vectors $\mathbf{a}$ and $\mathbf{t}$ and matrix $\mathbf{H}$ as defined in (3.26), (3.27) and (3.28) become much larger than necessary. Processing time required for MAP estimation increases exponentially with an increase in the number of impulses found (Section 5.8). Thus, the presence of too many false-alarms slows down MAP estimation considerably. For this reason we need to make sure that signal-to-noise ratios are as high as possible and that the threshold γ used by the detector algorithm is optimal.

The RMS errors between estimated impulse amplitudes and true amplitudes for different SNR's are given in Table 3.4. A higher SNR result in a smaller error and thus better

[8]This corresponds to more that 13,000 particles per second.

SNR	40dB	35dB	32.5dB
RMS error	1.765	2.693	5.727

Table 3.1: RMS errors between estimated impulse amplitudes and true amplitudes for different SNR's.

estimates. This further underlines the need for as high as possible SNR.

3.5 MAP Amplitude Estimation vs Simple Deconvolution

It will be shown in Section 5.8 that MAP estimation requires substantial processing time. The number of floating-point operations needed to perform MAP estimation increases exponentially with an increase in the number of impulses. A question that springs to mind is: "Does MAP estimation improve impulse amplitude estimates and therefore justify the extra processing power?" We answer this question by doing an experiment similar to those described in the previous section.

The top graph in Figure 3.11 shows the simulated BG input signal $u(n)$ over a time period $\Delta t = 0.25$s. Impulse density is such that there are 50 impulses in this time window. The input $u(n)$ was then convolved with the wavelet $h(n)$ in Figure 3.7(a) and noise added with SNR = 35 dB. Using this synthetic observed signal the amplitudes were estimated using both MAP estimation and simple deconvolution.

The bottom graph in Figure 3.11 is an error plot showing the absolute errors for MAP estimation and simple deconvolution for all 50 impulses. It is clear that errors due to MAP estimation are much smaller that those from simple deconvolution. The RMS error for simple deconvolution is 16.785 while the RMS error for MAP deconvolution is a much lower 2.856.

It can be mentioned that in the absence of any noise simple deconvolution outperforms MAP estimation when estimating amplitudes. This can be seen from the equation depicting

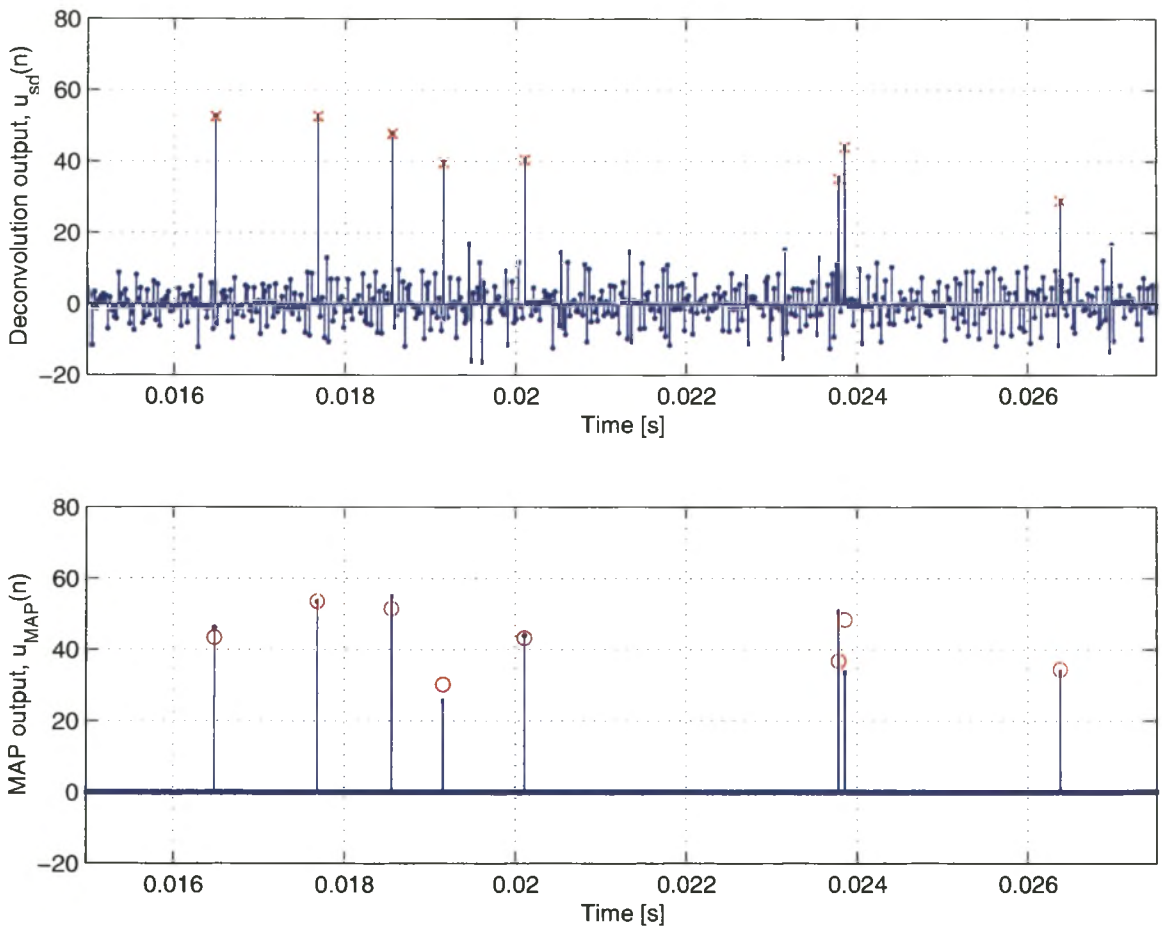

Figure 3.8: Deconvolution results for SNR of 40 dB. (top) Simple deconvolution output $u_{sd}(n)$ is used to detect when impulse events occur. Detected events are depicted by crosses. (bottom) MAP estimates of impact amplitudes. Bars depict estimates and circles depict true values.

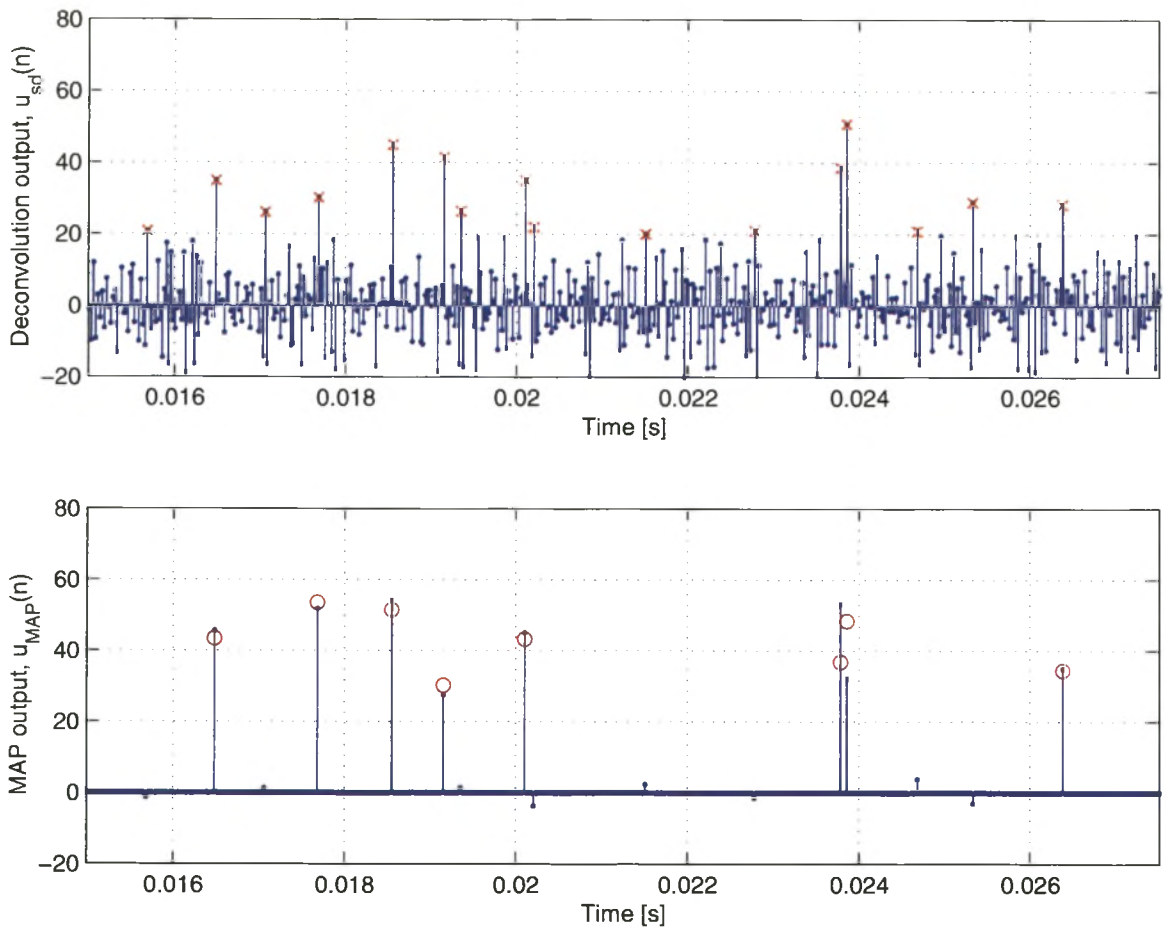

Figure 3.9: Deconvolution results for SNR of 35 dB. (top) Simple deconvolution output $u_{sd}(n)$ is used to detect when impulse events occur. Detected events are depicted by crosses. (bottom) MAP estimates of impact amplitudes. Bars depict estimates and circles depict true values.

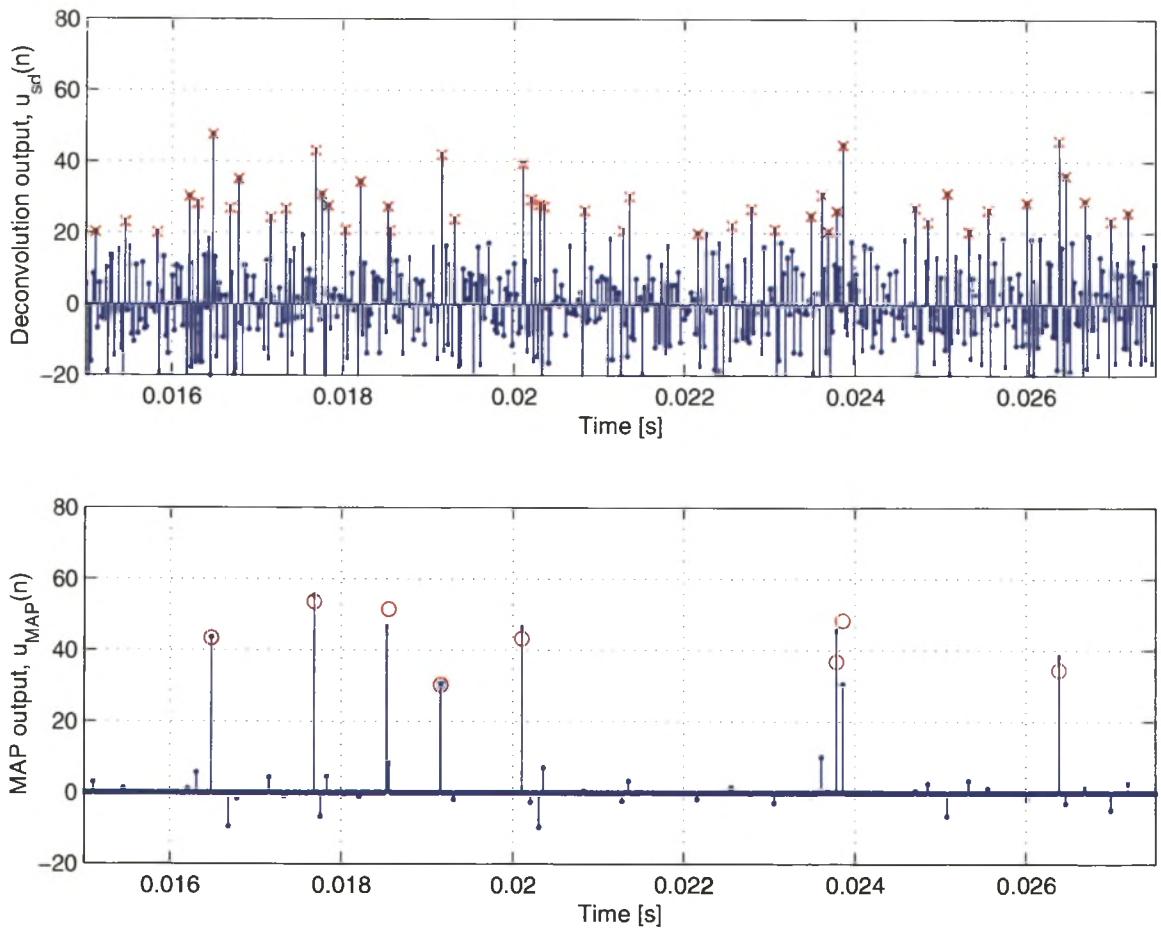

Figure 3.10: Deconvolution results for SNR of 32.5 dB. (top) Simple deconvolution output $u_{sd}(n)$ is used to detect when impulse events occur. Detected events are depicted by crosses. (bottom) MAP estimates of impact amplitudes. Bars depict estimates and circles depict true values.

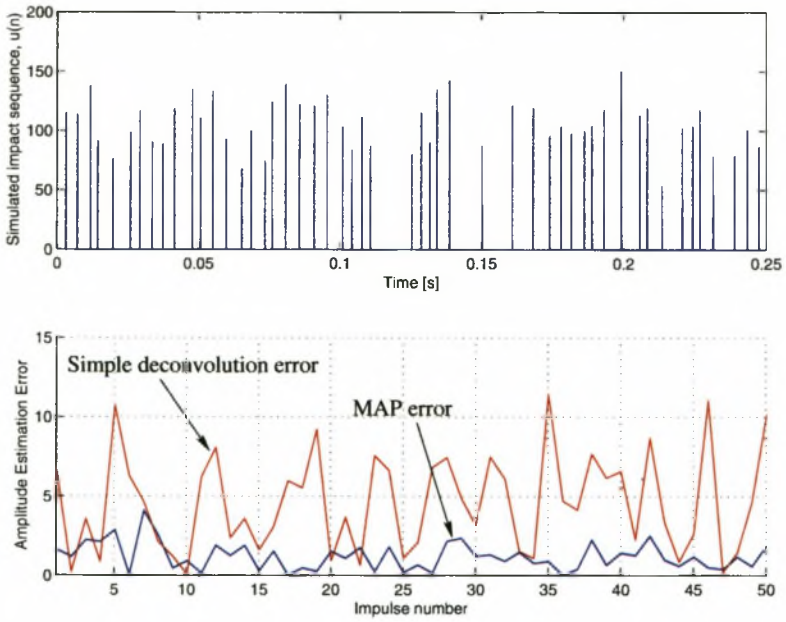

Figure 3.11: (top) Simulated BG input signal $u(n)$. (bottom) Absolute errors for MAP estimation and simple deconvolution. The RMS error for simple deconvolution is 16.785 and the RMS error for MAP deconvolution is 2.856.

simple deconvolution (3.25) which is repeated here for convenience

$$\begin{aligned} \hat{U}(z) &= U(z) + F(z)E(z), \\ &= U(z) + E(z)/H(z). \end{aligned} \tag{3.39}$$

This is for the ideal situation where we know the exact inverse filter such that $\hat{H}^{-1}(z)H(z) = 1$. If there is no noise in the observed signal, $E(z) = 0$ and $\hat{U}(z) = U(z)$, i.e. there is no error in the amplitude estimate using simple deconvolution. With MAP deconvolution we still assume an underlying distribution that will introduce errors since this assumption is not 100% correct.

Unfortunately this noise-free scenario is not a realistic one. With decreasing SNR's, MAP estimation dominates in the battle for smaller estimation errors.

3.6 Summary

In this chapter it was described in detail how the system and all relevant signals can be modelled. The observed signal $x(n)$ is merely the convolution of some input $u(n)$ with the wavelet $h(n)$. In an attempt to determine particle size distributions, we need to deconvolve the effect of $h(n)$ and additive noise out of $x(n)$. It was found that it is beneficial to represent the input as a Bernoulli-Gaussian process. A statistical deconvolution process (MAP) can then be used to obtain a good estimate of impulse amplitudes, even in the presence of substantial noise. We finished the chapter with simulated data and results. It was shown how an efficient algorithm can be used to firstly *detect* temporal impulse positions and then to *estimate* their amplitudes. It is a non-recursive algorithm that can be done on-line.

Chapter 4

Impact Energy Compensation

Although particles falling off the conveyor will be guided to fall on approximately the same location on the bar, there will always be a variance present in the exact position of impact. Particle size estimates are influenced by the position of impact on the bar.

Figure 4.1 is a diagram of the bar indicating the position of impact x_{impact}. The bar and

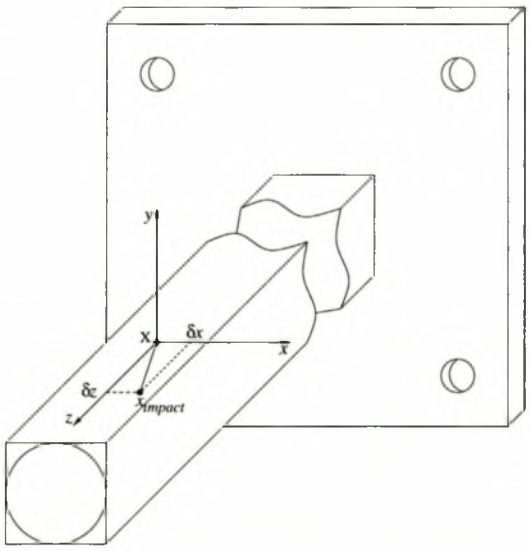

Figure 4.1: Diagram of bar showing possible variance in position of impact in x and z dimension.

conveyor are installed in such a way as to make position X the most likely position of

impact. X will therefore be the mean impact position with a distribution of positions around this point. The variance of the distribution is two dimensional and can occur in both the x and z dimensions of the bar.

The distance between impact position x_{impact} and X is given by δx in the x direction and δz in the z direction. Particle size estimates are effected by both deviations δx and δz. These effects are compensated for by determining the position of impact for every particle and then scaling the particle size estimate according to a function $f(x, z)$. The compensation is done independently for x and z respectively as explained in the rest of the chapter.

The location where the particle strikes the bar along its length, or the z coordinate of impact, is referred to as the "impact position". "Impact angle" is used to refer to the position of impact in the x direction which will cause a glancing blow to either the left or right.

In order to do angle compensation, we measure both the vertical and horizontal components of vibration of the bar. Impulse detection (Section 3.3.3.5) and the initial particle size estimate are performed using only the vertical component. Horizontal impulse amplitudes are solely used to determine the angle of impact.

4.1 Impact Position Compensation (IPC)

As falling particles impact on the bar, energy transferred is a function of the position of impact along the length of the bar (in the z-direction). This relation is shown in Figure 4.2 which is a graph of normalised particle size estimates versus impact position. The amplitudes of the stems are particle size estimate means of data sampled by recording multiple observations of particle impact along the length of the bar at 10 mm intervals. In other words, a single particle was dropped from a fixed height onto different locations along the length of the bar. More specifically, the particle was dropped at l, $l - 10$mm, $l - 20$mm, $\ldots$, $l - 100$mm, thus giving us multiple observations at 11 different impact positions along the length of the bar. Here l is the length of the bar. The complete experimental procedure is described in Section 5.1.

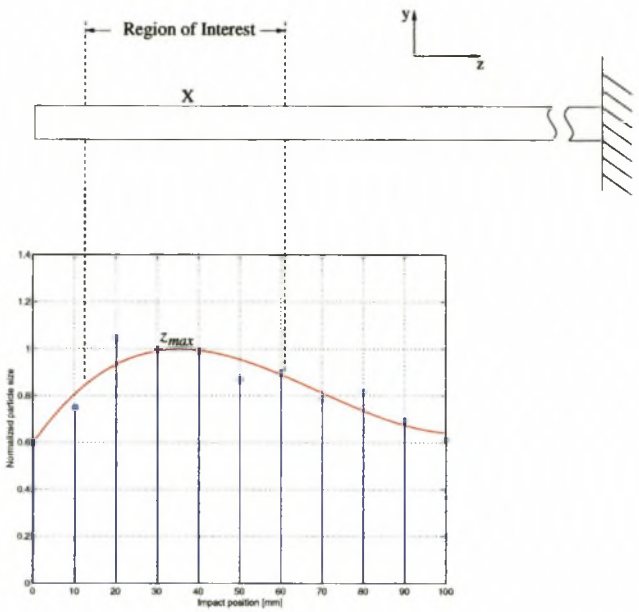

Figure 4.2: Normalised particle size estimate vs. impact position along the length of the bar.

Maximum energy is transferred at impact location z_{max}. This is the "sweet spot" of our bar. It can be seen that there is as much as a 40% fluctuation in size estimates between the minimum and maximum size estimate values for a uniform particle size.

A polynomial $P(z)$ of degree 3 is fitted to the data in a least-squares sense and is also shown in Figure 4.2. This polynomial is used to compensate for size estimates once the impact position has been determined. Compensation is achieved by scaling the size estimate of a particle with the polynomial value corresponding to the estimated position of impact.

4.1.1 Determination of Impact Position

The frequency characteristics of the bar were discussed in Section 2.1 with the frequencies present in the bar given in (2.3). These frequencies are determined and fixed by the physical properties of the bar like the metal properties and boundary conditions (cantilever bar). The pole positions of the system are positioned according to the characteristic frequencies. In Figure 4.3 the frequency of the $i'th$ characteristic, w_i, is predetermined by (2.3).

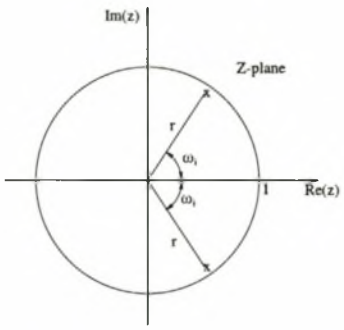

Figure 4.3: Z-plane pole position due to characteristic frequency, w_i.

It was found though, that the system produces different AR coefficients depending on the position of impact along the length of the bar. The distance r of the poles from the origin changes as the impact position changes. The shapes of the first five characteristic functions for a cantilever bar is shown in Figure 2.4. If the bar is struck on a node (a zero) of a mode, that mode is not exited and thus will not be present in the bar vibration. The further a particle strikes the bar from a node, the greater the amplitude for that corresponding mode. This is shown in Figure 4.4 which is the frequency amplitude response of bar vibration resulting from impacts at two different impact positions. Figure 4.4(a) is the response of a bar struck at its free end. None of the modes for a cantilever bar has a node at the free end, thus all seven modes can clearly be seen. Figure 4.4(b) is the frequency response where the bar was struck at $z = 0.77 \times l$ where l is the length of the bar. Figure 4.5 shows the second and sixth characteristic functions on one graph. It can be seen that the second mode has a node at position $z = 0.77 \times l$. Therefore the second resonance in Figure 4.4(b) (at about 700 Hz) is not present. The sixth mode of vibration also has a node at $z = 0.77 \times l$ (as shown in Figure 4.5). This explains the absence of the resonance at about 9,500 Hz in Figure 4.4(b).

From this it is clear that different impact positions will result in different AR parameters. With the reflection coefficients being an equivalent representation of an AR(p) process [28], they can be calculated efficiently with the use of the Levinson algorithm. The reflection coefficients can then be used to construct a p-dimensional feature space and using pattern

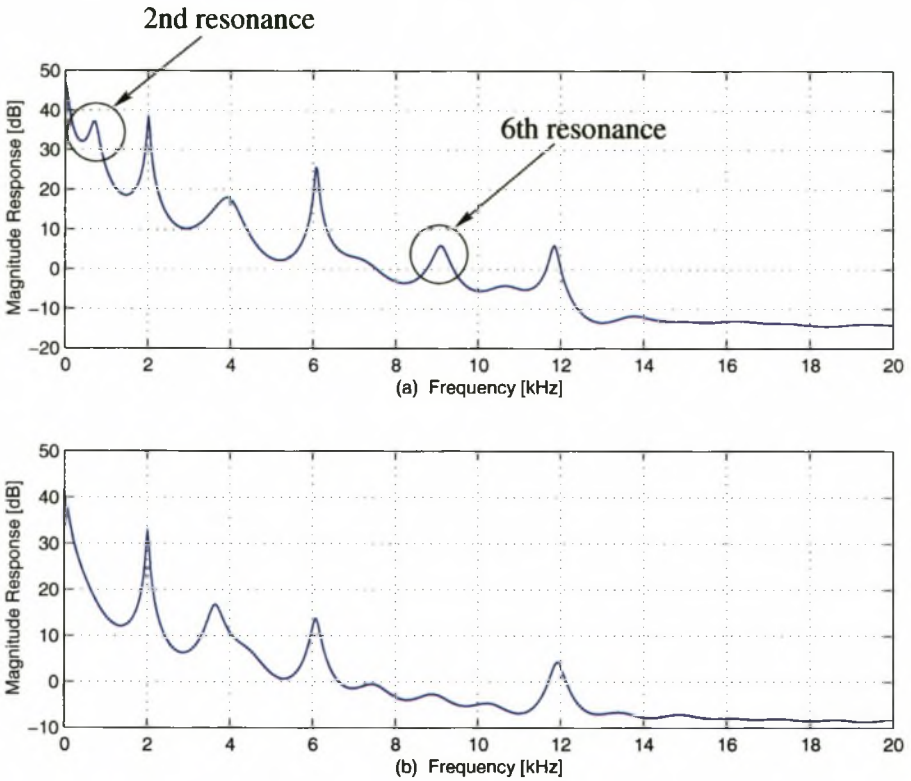

Figure 4.4: Amplitude frequency response of cantilever bar vibrations. (a) Bar struck at its free end and thus all modes are present. (b) Bar struck at the node of mode 2 and 6 resulting in the absence of those two resonances.

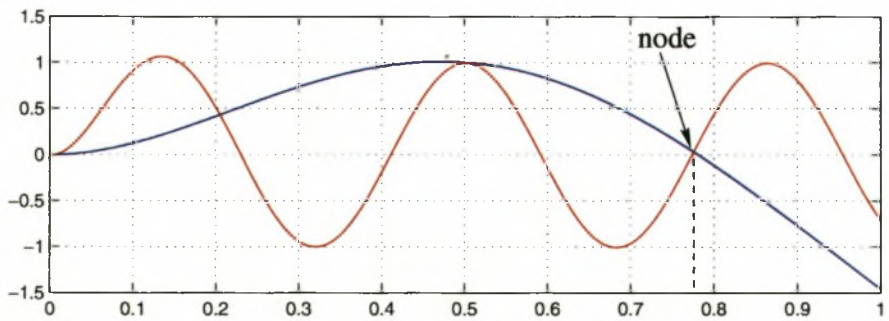

Figure 4.5: The second and sixth characteristic functions of a cantilever bar both have a node at $0.77 \times l$ where l is the length of the bar.

recognition techniques one can classify an observed vector to determine the exact position of impact as discussed in the following two sections.

4.1.2 Karhunen-Loève Transformation

Measured p-dimensional features consisting of reflection coefficients as estimated by the Levinson recursion have substantial redundancy. The biggest problem with this redundancy is the so called "curse of dimensionality" [34]. Processing time increases exponentially as the number of dimensions in the feature vectors increases. It is important to present the measured features compact and efficiently.

The Karhunen-Loève Transformation (KLT) is a popular method of reducing redundancy in the original sample space by projection the features into a new space of lower dimensionality.

The KLT is derived by determining an estimate $\hat{\mathbf{y}}$ of the set of p-dimensional feature vectors $\mathbf{y}$ by only using d dimensions, where $d < p$. This will reduce the dimensions of the original feature space to a d-dimensional set. By minimising the square error between $\mathbf{y}$ and $\hat{\mathbf{y}}$ it can be shown that the optimal basis $\mathbf{U} = \{\mathbf{u}_1, \mathbf{u}_2, \mathbf{u}_3, \dots\}$ onto which $\mathbf{y}$ must be projected are given by the eigenvectors of the matrix $\Phi = E\{\mathbf{y}\mathbf{y}^T\}$. The complete derivation can be found in [34].

An important property of the KLT is that the variance of the data in the direction of the basis vector $\mathbf{u}_j$, is given by the corresponding eigenvalue of Φ [34]. This implies that the approximation of $\mathbf{y}$ should be constructed from the eigenvectors associated with the d largest eigenvalues. Also the features in the transformed space are uncorrelated.

4.1.3 Feature Space Trajectory

For the purpose of impact position determination, we make use of a training approach whereby multiple impact observations at various positions along the length of the bar are sampled. Data are grouped into 11 classes with each class consisting of feature vectors

calculated from impacts spread over the free end of the bar at intervals of 10 mm, thus giving us data at impact positions 0, 10, 20, 30, ... , 100mm from the free end of the bar.

With data grouped into separate classes another form of the KLT can be used, namely the class-based KLT. By making use of the information contained in the class means, vector components are first decorrelated by a KL transform and subsequently the variances are normalised to unity. To obtain optimal compression, the axes are rotated by an additional transformation as to connect the centre of gravities with the most important axis. See [34] for more details.

It was empirically determined that using an order $p = 32$ provide features that enable us to accurately classify impact position. The marginal improvement achieved by using an order greater than 32 does not justify the additional processing power needed.

Figure 4.6 shows reflection coefficients vectors after being reduced from 32 dimensions to 3 dimensions with the use of the class-based Karhunen-Loève Transformation. The data used to produce these results were generated by dropping one marble from a fixed height onto specific positions along the length of the bar. The impact positions were at 0, 10, 20, ... , 100mm from the open end of the bar and make up the different position classes. It is explained in Section 5.1.2 how we use a Particle Holding Device (PHD) to accurately generate experimental data by dropping test particles onto exact positions on the bar. Using the PHD, there can be a deviation of up to 3mm in the impact position in any direction. Feature vectors will thus form clouds in the feature vector space rather than points.

Figure 4.6(a) is a 2-dimensional representation of the 3-dimensionally reduced feature vectors displaying dimension 1 vs. 2 whereas Figure 4.6(b) shows dimension 2 vs. 3. Different colours indicate the different impact position classes which are numbered from class 0 to 10. The position classes are clearly separated. Figure 4.7 is a 3-D plot combining Figures 4.6(a) and (b). Clouds are formed that are separated in 3-D space along a definite feature space trajectory [35]. This can be extrapolated and then used to estimate impact position by means of a classification algorithm like K-Nearest Neighbour (KNN). Impulse amplitude variation can then be compensated for quite easily.

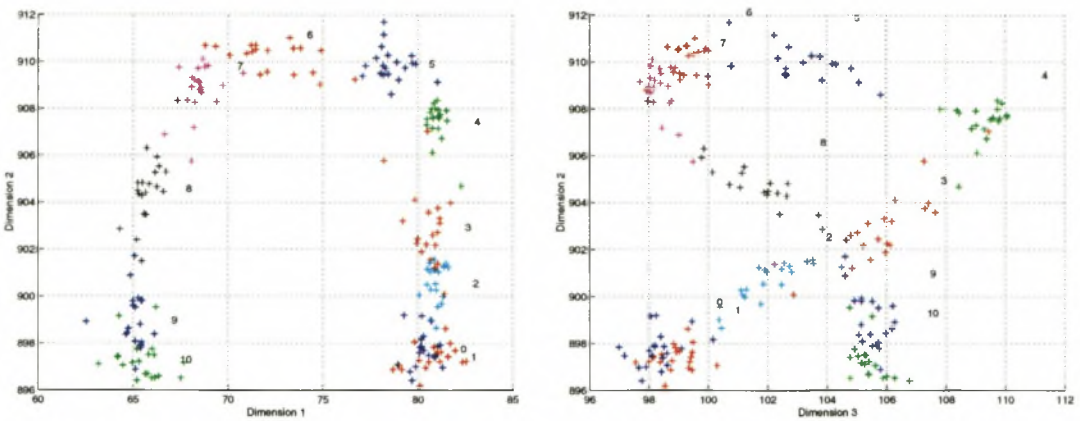

Figure 4.6: 2-D representation of reflection coefficients after dimension reduction using KLT. Different colours show different impact positions along the length of the bar. Class positions for dimension 1 vs. 2 are depicted in (a) and (b) shows the positions for dimension 2 vs. 3

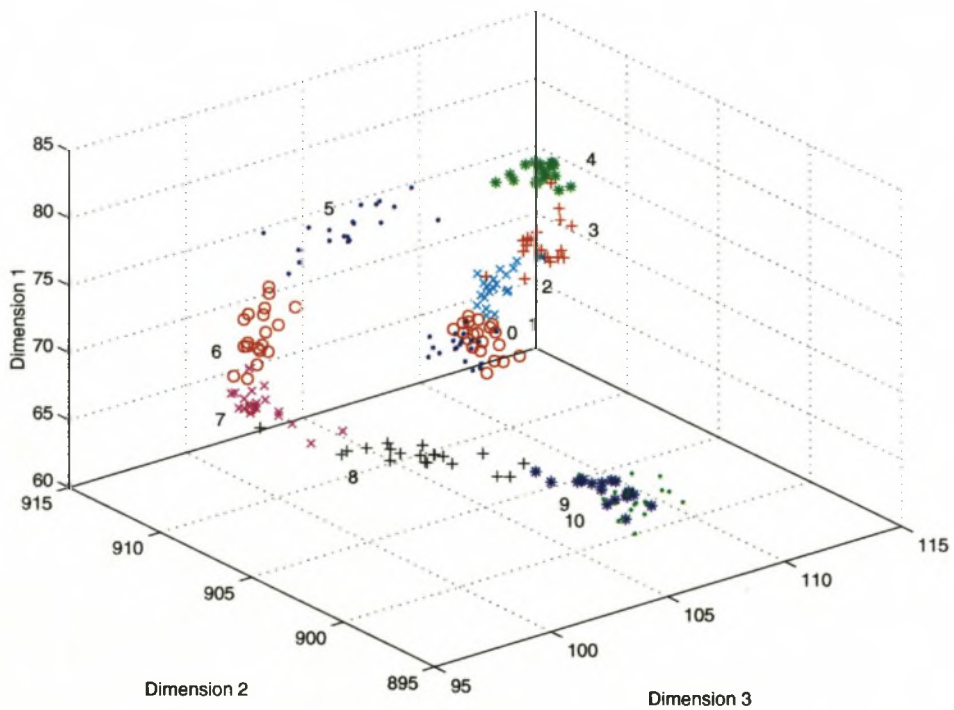

Figure 4.7: 3-D feature space trajectory for 11 impact position classes.

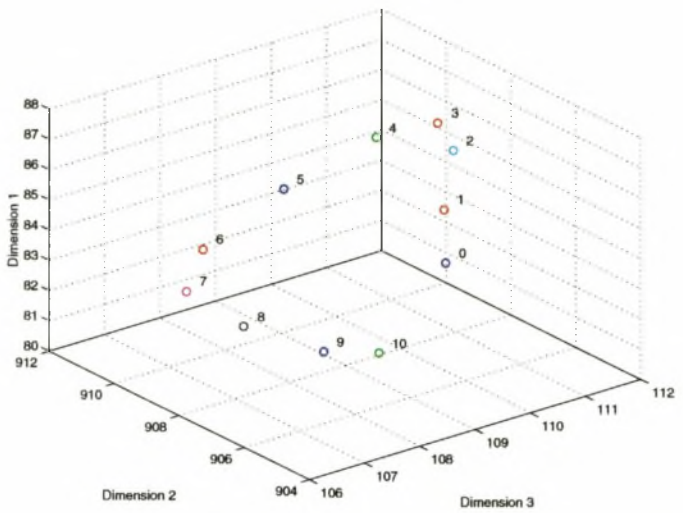

Figure 4.8: 3-D feature space trajectory for 11 impact position classes using simulated data.

4.1.4 Theoretical Validation

As validation for results achieved in the previous section, bar vibration wave theory discussed in Section 2.1.2, was implemented to generate simulation data according to different impact positions along the length of the bar. Reflection coefficients calculated from this synthetic data were transformed using the KLT transformation matrix determined for real training data from the previous section. The 3-dimensional feature space trajectory for the simulations is shown in Figure 4.8. A comparison between Figures 4.8 and 4.7 reveals that theoretical predictions are indeed very similar to results achieved using real data.

4.2 Height Compensation

In Section 3.1.1 we mentioned how the bar could be installed at a slight angle α from the horizontal to reduce the problem of a rebounce. See Figure 3.1.

If the bar is installed horizontally or even at a small angle, the height particles fall from can be assumed to be constant. However, with knowledge of impact position z discussed in the previous section, it is trivial to compensate for a difference in height caused by the

angle the bar is installed at. The simple trigonometric relation

$$\delta y = \delta z \sin(\alpha) \tag{4.1}$$

relates the change in height δy to the change in impact position δz.

4.3 Angle Compensation

Angle compensation scales estimated particle sizes that are inaccurate because of glancing blows. Glancing blows occur when falling particles strike the bar obliquely so as to bounce off at an angle. The free end of the bar is shown in Figure 4.9. Here the square and round bars are overlaid on the same diagram with the different angles shown resulting from an impact to the right of the centre of the bar. The impact angle is defined as the positive angle between the vertical y-axis and a line drawn from the point of impact through the centre of the cross section. The sign of the angle does not matter due to symmetry of the bar as glancing blows to the left and right have the same effect.

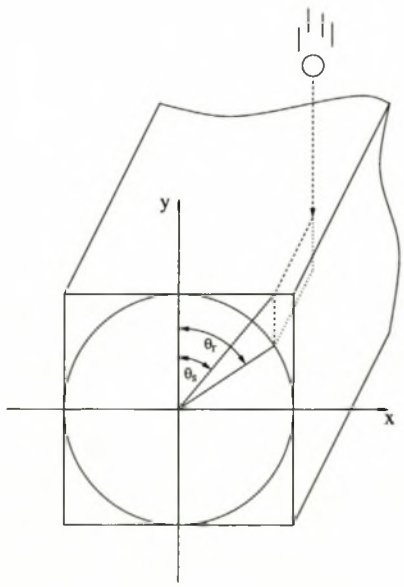

Figure 4.9: Impact angles are defined as the positive angle between the vertical y-axis and a line drawn from the point of impact through the centre of the cross section.

Vibration measurements are made in both the vertical y-direction and also the horizontal x-direction. We model the energy at a given instant as the vector sum of the energies in the vertical and horizontal directions. See Figure 4.10.

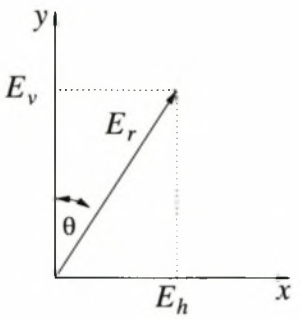

Figure 4.10: Vector representation of vertical & horizontal energies. Total impact energy E_r is the vector sum of the vertical and horizontal components.

This vector notation enables one to compensate for glancing blows where a fraction of the energy in the falling particle is transferred to the bar. Having an estimate of E_v and E_h it is easy to determine the angle θ. Deconvolution techniques described in Chapter 3 are used to determine impulse amplitudes as measured in the vertical and horizontal directions, a_v and a_h. From Figure 4.10 it is clear that there is a simple trigonometric relation between a_v, a_h and θ given by

$$\theta = \tan^{-1}\left(\frac{a_h}{a_v}\right). \tag{4.2}$$

A function $f_{ang}(\theta)$ scales the estimated impulse amplitude to the maximum.

Note that impulse detection (Section 3.3.3.5) and the initial particle size estimate are performed using only the vertical component of vibration. Horizontal impulse amplitudes are solely used to determine the angle of impact.

The effect glancing blows have on a square bar is different to that on a round bar. This is illustrated in Figure 4.11 which shows normalised particle size estimates vs. angle of impact for the round bar, Figure 4.11(a), and the square bar, Figure 4.11(b). Size estimates for glancing blows of more than 60° are erratic for the round bar. These are simply discarded.

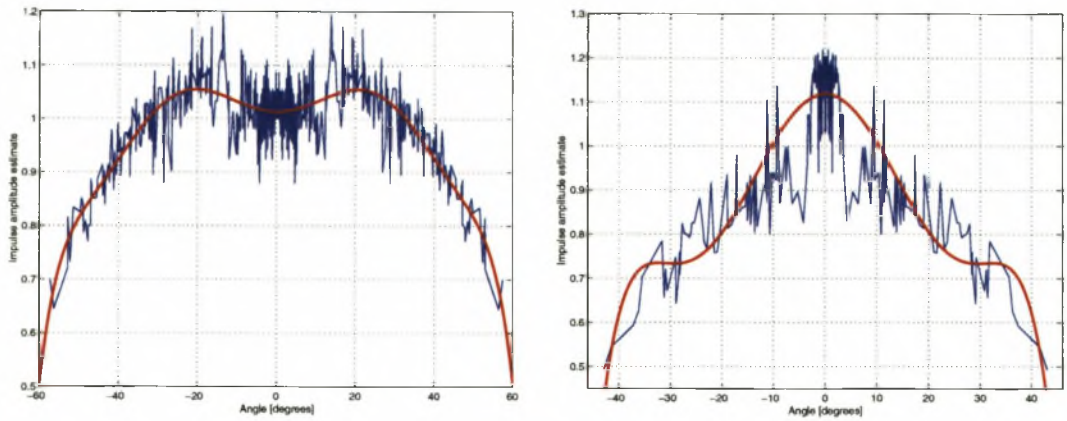

(a) (b)

Figure 4.11: Normalised particle size estimates for the (a) round bar and (b) square bar. A polynomial that is fitted to the data in a least-squares sense is used to scale size estimates.

From Figure 4.9 it can be seen that for the square bar, angles above 45° are not defined and thus not used.

Similar to impact position compensation Section 4.1, a polynomial that fits the data in Figure 4.11 in a least-squares sense, is used to scale size estimates.

4.4 Summary

Particle size estimates are a function of position of impact on the bar. This results in a wide size distribution for a uniform particle size and is clearly undesirable. Fortunately, we are able to determine where the particle strikes the bar.

Size estimates are influenced mainly by two components of positional variance; (i) impact position along the length of the bar and (ii) the angle of impact due to glancing blows. If the bar is installed at an angle from the horizontal, there is also a third component since a variance in impact position along the length of the bar will result in height differences as well. Having determined the exact position of impact on the bar, size estimates are scaled as to compensate for erroneous size estimates due to variance in impact position.

Chapter 5

Experiments and Results

The results presented here are aimed at showing that our instrument is able to estimate particle size distributions within acceptable tolerance. We also show under which operating conditions the sensor operates optimally.

The first section in this chapter describes the experimental configuration and the experimental procedure that were performed to generate experimental data. The rest of the chapter presents results achieved using this data.

5.1 Experimental Setup

5.1.1 Experimental Hardware

A photograph of the experimental setup is shown in Figure 5.1. A metal cantilever bar of length 0.3m is firmly bolted to a wall. Eight strain gauges in two pairs of four each sensing vertical and horizontal vibrations, are applied to the bar as shown in Figure 2.6(b)[1]. A DC excitation voltage, $V_{exc} = 8$V is applied over the bridge. This voltage level ensures that V_{exc} is below the maximum permitted bridge energizing voltage which is supplied by the strain gauge manufacturer as $V_{max} = 9$V for strain gauges used.

[1]Refer to Section 2.2 for details about hardware configuration.

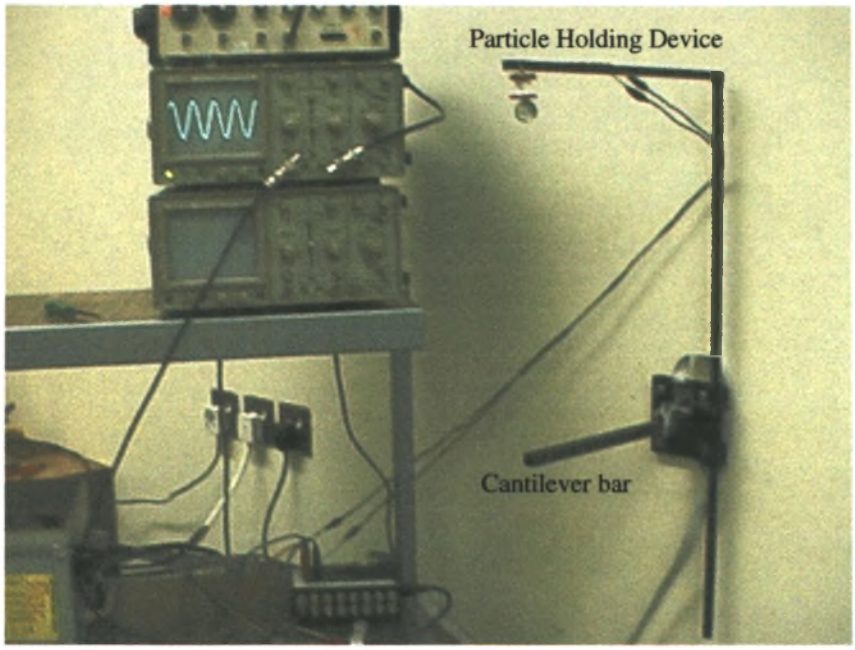

Figure 5.1: A photograph of the experimental setup showing a cantilever bar bolted to a wall, the particle holding device and the data acquisition hardware.

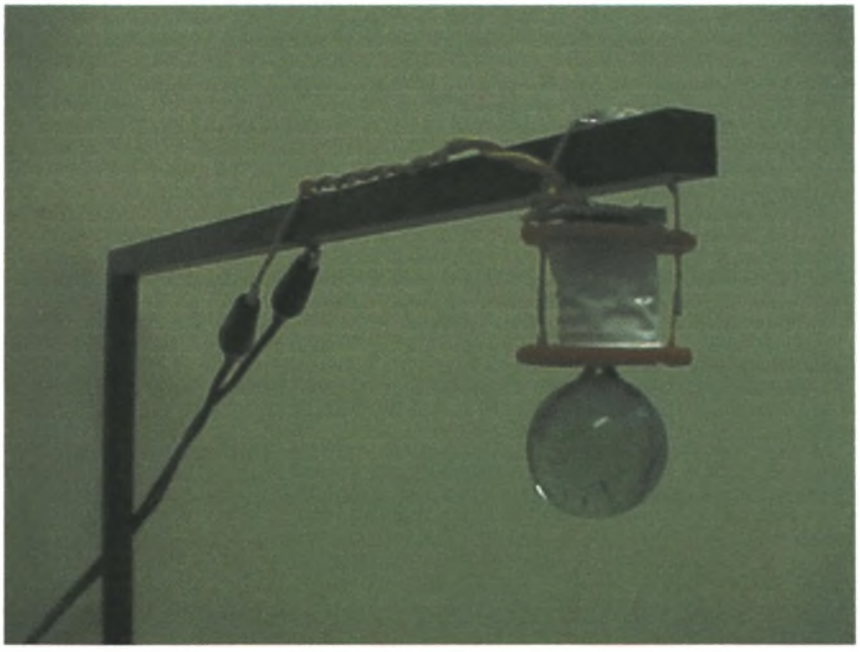

Figure 5.2: The particle holding device consists of an arm with an electromagnet. It enables us to generate accurate experimental results by dropping test particles onto precise locations on the bar.

Instrumentation amplifiers with gains of $G_{vert} = 2250$ and $G_{horiz} = 4155$ are used to measure and amplify $V_{out\ vert}$ and $V_{out\ horiz}$, the outputs of the Wheatstone bridges for the vertical and horizontal vibrations respectively.

5.1.2 Particle Holding Device

The particle holding device (PHD) can be seen in Figure 5.1. A close-up is shown in Figure 5.2. It consists of an arm and an electromagnet. A small piece of ferrous metal is glued onto the test particle which is then magnetically held up by the electromagnet. This enables us to get accurate experimental results by dropping all particles from a fixed height onto the same location on the bar. The surface of the electromagnet that is in contact with the test particle (or rather the metal object that is glued to it) is round with diameter $d = 6$mm. The PHD is accurately positioned with the use of a plumb-line. Because of the finite surface area of the magnet, impact positions for experimental data can deviate up to 3mm from the supposed impact position in any direction.

5.1.3 Test Particles and Test Procedures

Test particles used to generate experimental results, consist of four glass marbles of different sizes. Table 5.1 specifies the marble mass in gram [g].

Particle #	1	2	3	4
Mass [g]	19.1	8.75	4.7	3.2

Table 5.1: Test particle sizes in gram.

Using the PHD, these particles were dropped at various impact positions on the bar. More specifically, bar vibrations were recorded for particle impact at intervals of 10mm across the free end of the bar, thus giving us a number of observations in 11 different impact positions classes at impact positions 0, 10, 20,30, ... , 100 mm from the free end of the

bar. Observations for particle impact in the middle of the bar in the x-direction as well as glancing blows to the left and right were recorded.

In Section 4.3 we saw that the behaviour of a round cantilever bar to particle impact is different to that of a square bar. Uncompensated size estimates due to glancing blows on a square bar are far more erratic than those for the round bar. In order to determine which of these bar configurations results in better size estimates after compensation, experiments were performed using both the round and square bars.

5.1.4 Data Acquisition

Bar vibrations were sampled simultaneously for both the vertical and horizontal components at a sampling rate of 40kHz each using a PC30FS16 sampling card from *Eagle Technology*. This analogue to digital converter allows for 12 bit precision in the dynamic range of $\pm$5V.

5.2 Relationship Between Particle Size and Impulse Amplitude

Figure 5.3 depicts the linear relationship between particle mass and the estimated impulse amplitudes using MAP estimation. The stars are the means of estimated impulse amplitudes for the four test particles plotted against their mass. The means were taken for 20 observations per particle size. The straight line fitted to the four points in a least-squares sense shown in Figure 5.3, indicates that the relation between amplitude estimates and true particle mass is linear. The straight line describes the conversion equation

$$m = ax + b, \tag{5.1}$$

for m the particle mass (in gram) given the estimated impulse amplitude x.

This result verifies our assumption that impulse amplitudes reflect the energy in the impact

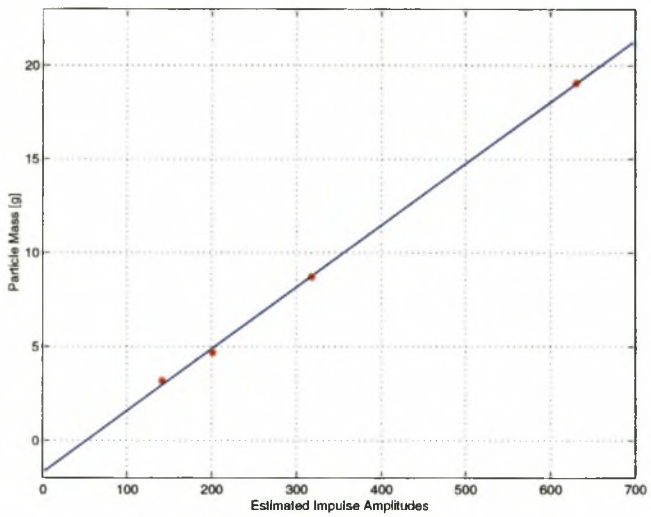

Figure 5.3: Particle mass vs. estimated impulse amplitudes.

given by [14]

$$U = mgh, \tag{5.2}$$

where U is the gravitational potential energy for a falling particle of mass m falling from a height h and g is the acceleration due to gravity. If the particle fall from rest, its kinetic energy K will initially be zero and its potential energy U as given in (5.2). At the end of the fall, at the moment of impact, the law of the conservation of mechanical energy [14] states that all the potential energy U at time $t = 0$ is transferred to kinetic energy K. It is this kinetic energy that is dissipated in the impact between the particle and the bar.

The system calibration factor, a, or the gradient of the line in Figure 5.3 is determined by the sensitivity of the measuring hardware. This in turn is determined by the bridge excitation voltage V_{exc}, the strain gauge factor k, the gain of the instrumentation amplifier and the bar material properties and dimensions. Values for our experimental setup for a

and b are:

$$\begin{aligned} a &= 0.0328, \\ b &= -1.665. \end{aligned} \tag{5.3}$$

5.3 Height Compensation

Equation (5.2) suggests there is a linear relationship between the height h particles fall from and the energy in the impact or the impulse amplitude estimate. This is shown in Figure 5.4. The horizontal axis is the height h and the vertical axis impulse amplitude estimates. The stars are the means of 20 impulse amplitude estimates for multiple observations dropped from heights $h = 200$, 250, 300 and 350mm and the solid line is a least-squares fit on the data points.

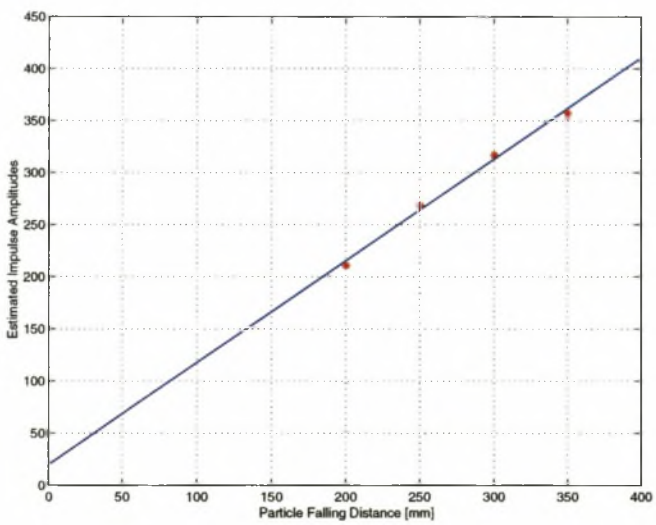

Figure 5.4: Estimated impulse amplitudes vs. particle falling height.

The equation for this line is given by

$$x = ch + d, \tag{5.4}$$

with

$$\begin{aligned} c &= 0.976, \\ d &= 20.560, \end{aligned} \tag{5.5}$$

for our configuration. Again the gradient c of the line is determined by the sensitivity of the measuring hardware. Height compensation discussed in Section 4.2, uses this scaling factor to compensate for any differences in height that may arise.

5.4 Empirical Results - Round Bar

Experiments were carried out as described in Section 5.1.3. Results for these experiments are presented in this section as well as Section 5.5 (for the square bar) using graphs similar to the ones depicted in Figure 5.5. They show estimated impulse amplitudes (estimated particle sizes) for all observations in the test set. The test data used here consist of 20 observations of particle impacts at impact positions $z = 0$mm, 20 observations at $z = 10$mm, 20 observations at $z = 20$mm, and so forth. The z-values used here, indicate the distance from the free end of the bar. Values in the graphs at these impact positions correspond to the means of each group of 20 observations with the standard deviations at these impact positions indicated by the error bars. The lengths of the vertical error bars depict the standard deviations.

The graph in Figure 5.5(a) shows raw, uncompensated estimates for the vertical component of vibration. It can clearly be seen how this plot relates to Figure 4.2 which shows the function used to compensate for variation in the impact position.

Figure 5.5(b) is raw, uncompensated estimates for the horizontal component of vibration. These impulse amplitude estimates are solely used to determine the angle of impact. This graph has a similar convex curve to Figure 5.5(a) but the variance, indicated by the error bars, are much bigger than the corresponding variances for the vertical component. This is due to the fact that horizontal impact amplitudes are far more sensitive to the angle of impact than vertical ones.

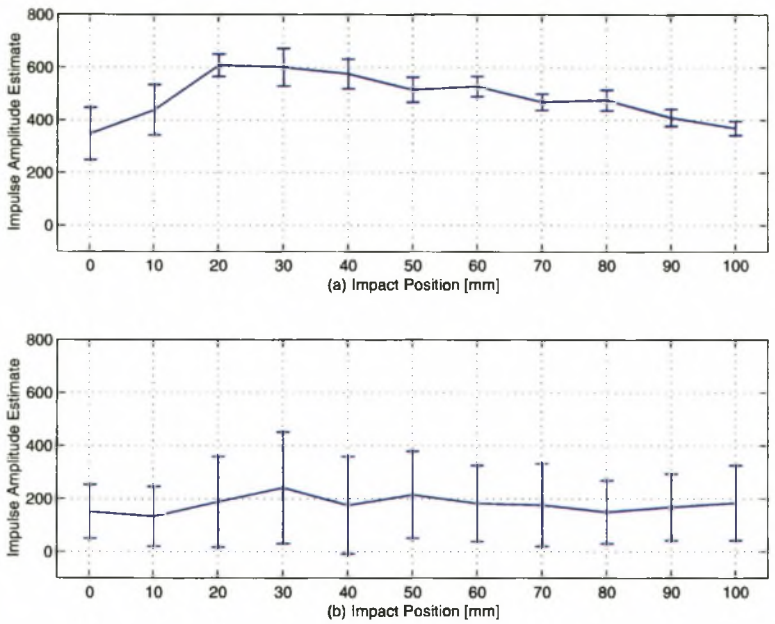

Figure 5.5: Raw impulse amplitude estimates for the round bar vs. position of impact. Vertical component amplitudes are depicted in (a) and horizontal amplitudes in (b).

Because horizontal impulse amplitudes are so sensitive to the angle of impact we use the vertical component amplitudes as indications of particle size. Thus Figure 5.5(a) represents particle size estimates. Since a single particle (uniform mass) was used to generate these results we should ideally get a straight horizontal line for all amplitude estimates shown. This is not the case due to the fact that in this graph we have not compensated for variations in the position of impact on the bar. Compensation for position and angle of impact are discussed in the following two sections.

5.4.1 Impact Position Compensation (IPC)

The concept of compensation for variance of the position of impact along the length of the bar was discussed in Section 4.1. Figure 5.6 shows impulse amplitudes after this compensation was performed. The convex curve of Figure 5.5(a) is completely removed in Figure 5.6. It must be concluded that impact position compensation reduces variance for particle sizes due to variation in the impact position, dramatically.

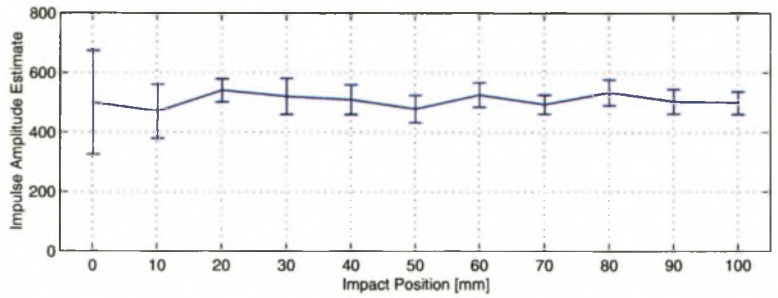

Figure 5.6: Round bar particle size estimates after impact position compensation.

5.4.2 Angle of Impact Compensation (AOIC)

After impact position compensation is performed, the estimated amplitudes are further scaled as to compensate for the angle of impact. Estimated amplitudes after this scaling has been performed are shown in Figure 5.7. A comparison between Figures 5.6 and 5.7 reveals that angle compensation improves amplitude estimates further. The lengths of the vertical error bars in Figure 5.7 are shorter and therefore size estimates have less variance.

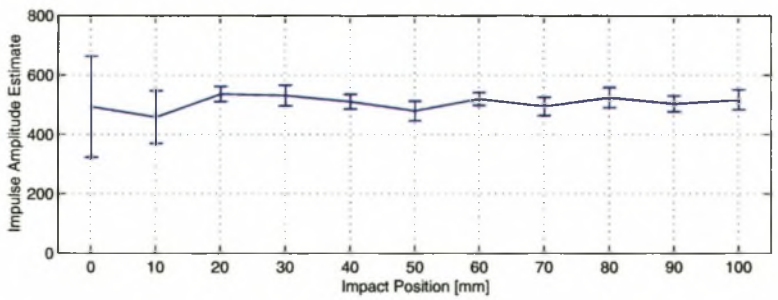

Figure 5.7: Round bar particle size estimates after impact position and angle of impact compensation.

5.4.3 Particle Size Distribution Estimation

From Figure 5.7 it can be seen that amplitude estimates for impact positions at $z = 0$ and $z = 10$mm are extremely erratic in comparison to the rest of the estimates. These estimates correspond to impacts very close to the free end of the bar and we are unable to improve

the variance for impacts in this region. Fortunately this problem can be eliminated using a combination of the following two solutions:

- The physical bar and cantilever configuration is such as to ensure that most particles will not impact near the free end of the bar.
- The exact position of impact for all impacts are determined, Section 4.1. An impulse amplitude estimate can be filtered out non-linearly if this impact was within the range l to $l-10$mm, where l is the length of the bar. Since these estimates are inaccurate they are simply discarded when the size distribution is determined.

The rest of the results given in this section represent size estimates after impacts at position $z = 0$ and $z = 10$ were thrown out. Also size estimates indicated here are after the impulse amplitudes were scaled to represent particle mass in gram. The test particle for this experiment has a mass $m = 19.1$g.

Particle size distributions are conveniently represented by histograms. The three histograms shown in Figure 5.8 depict size estimate results using the round bar with estimates binned into 20 equally spaced containers. The histograms in Figure 5.8(a)–(c) correspond to results shown in Figures 5.5, 5.6 and 5.7 respectively, i.e. Figure 5.8(a) shows raw size estimates, Figure 5.8(b) estimates after impact position compensation and Figure 5.8(c) shows final estimates after combined impact position and angle of impact compensation.

Since the same particle was used in this experiment we should ideally get a distribution with zero variance or a single "spike" distribution. The histogram for uncompensated size estimates in Figure 5.8(a) is very flat and thus not usable. This situation is significantly improved using compensation techniques as shown in the middle and bottom histograms.

The means and variances of these three histograms are given in Table 5.2. Figure 4.11(a) suggests a fairly uniform size estimate across a wide range of impact angles for the round bar. Therefore estimates are not heavily influenced by the angle of impact. This explains the relatively small improvement in the variance from the second to the third row in Table 5.2.

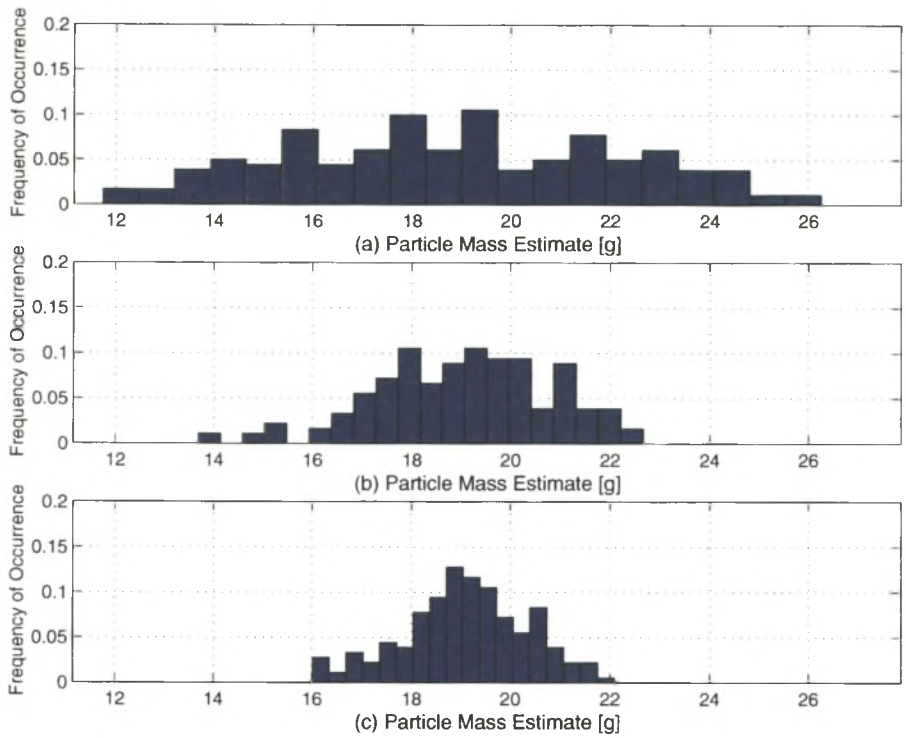

Figure 5.8: Histograms displaying estimated particle size distributions using a round bar. (a) Size distribution using raw data. (b) Size distribution after impact position compensation. (c) Size distribution after combined impact position and angle of impact compensation.

	Mean [g]	Variance
Raw data	18.85	11.03
After IPC	19.05	3.07
After AOIC	19.10	1.56

Table 5.2: Means and variances of round bar size estimates for raw data, after impact position compensation and after combined impact position and angle of impact compensation. Indicated values are for a uniform particle mass of 19.1g.

The third row in the table indicating the mean and variance of the size estimates after combined compensation, can be interpreted that for a uniform particle size, 87.1% of estimated sizes are within a 10% tolerance. This means 87.1% of the estimates are within the ± 1.91g range from the true particle size of 19.1g.

5.5 Empirical Results - Square Bar

A similar experiment to the one described in the previous section for the round bar, was performed using a square bar. Results obtained for these are presented here using the same graph formats as in the previous section. Amplitude estimates for observations at impact positions $z = 0$, 10, 20, 30, 40, 60, 80 and 100mm from the free end of the bar are indicated.

Figure 5.9(a) shows vertical amplitude estimates and horizontal estimates are shown in Figure 5.9(b). Similar to the round bar, the vertical component estimates for the square bar forms a convex curve over impact position. A major difference between the round and square bar is that the horizontal *as well as* the vertical size estimates have a rather large variance as indicated by the error bars. This is because square bar estimates are far more sensitive to the angle of impact than the round bar. We can compensate for this dependency on the angle of impact (Section 5.5.2) but it will be shown that square bar results are inferior to round bar size estimates.

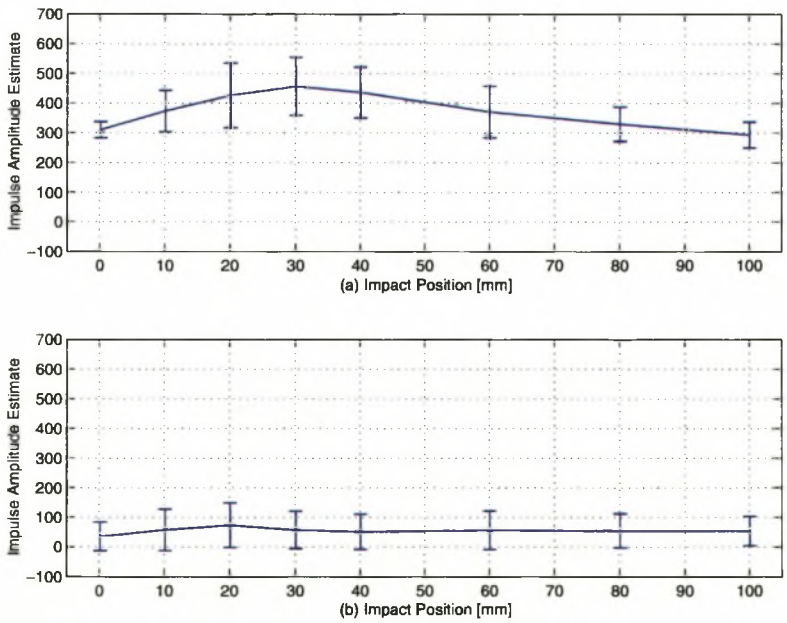

Figure 5.9: Raw impulse amplitude estimates for the square bar vs. position of impact. Vertical component amplitudes are depicted in (a) and horizontal amplitudes in (b).

5.5.1 Impact Position Compensation (IPC)

Figure 5.10 shows size estimates vs. position of impact after impact position compensation has been performed. Again the convex curve of Figure 5.9(top) was completely removed.

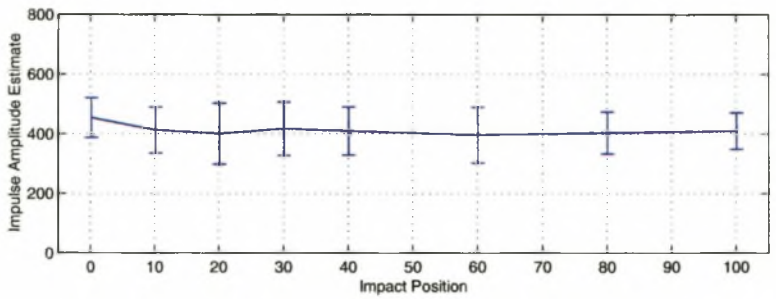

Figure 5.10: Square bar particle size estimates after impact position compensation.

5.5.2 Angle of Impact Compensation (AOIC)

The final compensation needed to be done for square bar size estimates is to attempt to reduce the large variance that are present due to glancing blows. Figure 5.11 shows size estimates after this angle of impact compensation. It can be seen that the situation is much improved but it will be shown in the next section that estimates for the round bar is far better than for the square bar. Some of the estimates for large angle of impacts are over compensated resulting in size estimates that are larger than the true particle size, whilst others have not been compensated enough.

5.5.3 Particle Size Distribution Estimation

Three histograms depicting size estimates using the square bar for raw data, after impact position compensation and after angle of impact compensation are shown in Figures 5.12(a)–(c) respectively.

Figure 5.12(b) shows that the size distribution after impact position compensation for

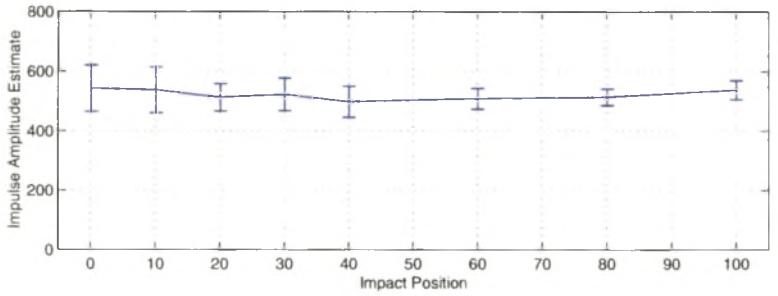

Figure 5.11: Square bar particle size estimates after impact position and angle of impact compensation.

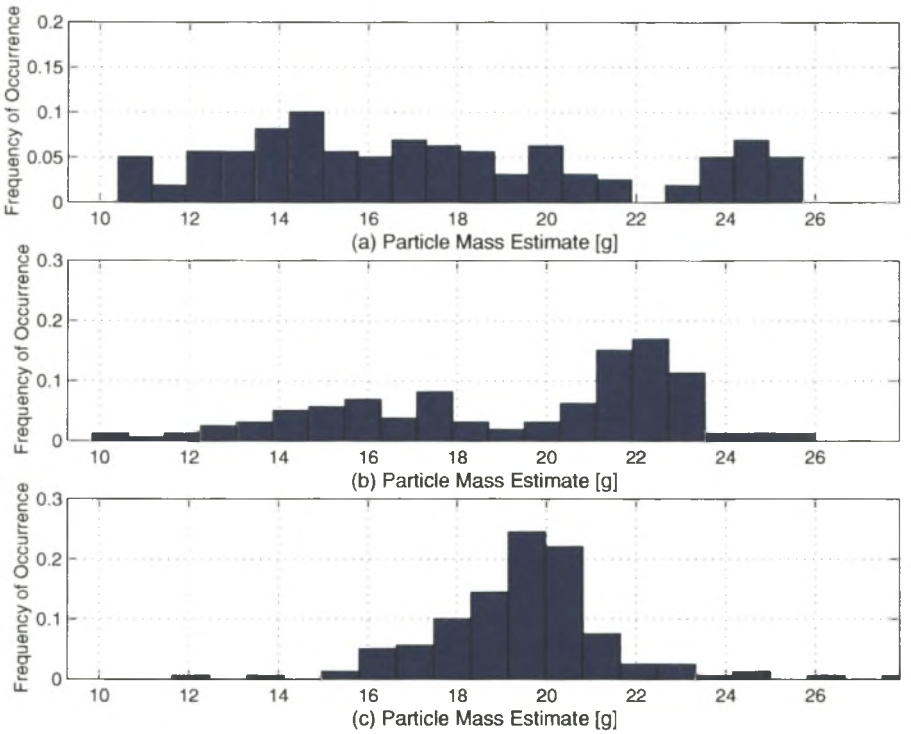

Figure 5.12: Histograms displaying estimated particle size distributions using a square bar. (a) Size distribution using raw data. (b) Size distribution after impact position compensation. (c) Size distribution after combined impact position and angle of impact compensation.

the square bar is still very broad and thus useless. The histogram has two "bumps" for a uniform particle size. This is due to the fact that there are two flat areas at 0° and ±30° for particle size estimates vs. the angle of impact as shown in Figure 4.11(b). Compensation for angle of impact improves this variance as can be seen in Figure 5.12(c).

	Mean [g]	Variance
Raw data	17.5	18.48
After IPC	19.31	13.29
After AOIC	19.45	4.00

Table 5.3: Means and variances of square bar size estimates for raw data, after impact position compensation and after combined impact position and angle of impact compensation. Indicated values are for a uniform particle mass of 19.1g.

Table 5.3 gives the means and variances of particle size estimates before and after compensation corresponding to the three histograms in Figure 5.12. Although variances are reduced after compensation, a comparison between Table 5.2 and Table 5.3 reveals that particle size distribution variance for a uniform particle size is much smaller using the round bar.

5.6 Comparison Between Round and Square Bar Size Estimates

In order to get a clearer picture how results for the round and square bar compare, Tables 5.2 and 5.3 are combined and presented in Table 5.4. From this table it is clear that for similar means the square bar variances are much bigger than corresponding ones for the round bar. As a matter of fact the round bar variance *before* AOIC is already better than the square bar variance *after* AOIC.

5.7 Spike Temporal Resolution

In Section 3.3.3.5 it was discussed how the simple deconvolution output $u_{sd}(n)$ is used to detect when impulses occur in time. The maximum rate of particle flow that can be dealt with is determined by this algorithm. It is essential that the rate of flow is small so that the particles impact on the bar one at a time, otherwise a signal that is larger than it

	Round bar		Square bar	
	Mean [g]	Variance	Mean [g]	Variance
Raw data	18.85	11.03	17.5	18.48
After IPC	19.05	3.07	19.31	13.29
After AOIC	19.10	1.56	19.45	4.00

Table 5.4: Means and variances of size estimates for raw data, after impact position compensation and after combined impact position and angle of impact compensation for both the round and square bar.

should be will be recorded. This type of error is known as coincidence error [3].

Figure 5.13 shows three impact events that were successfully resolved by the detector. The solid line is the simple deconvolution output $u_{sd}(n)$ and the stars show the detected spikes. These three spikes occurred in a time duration of $\Delta t = 3.6$ms. This corresponds to a rate of flow of 550 particles per second.

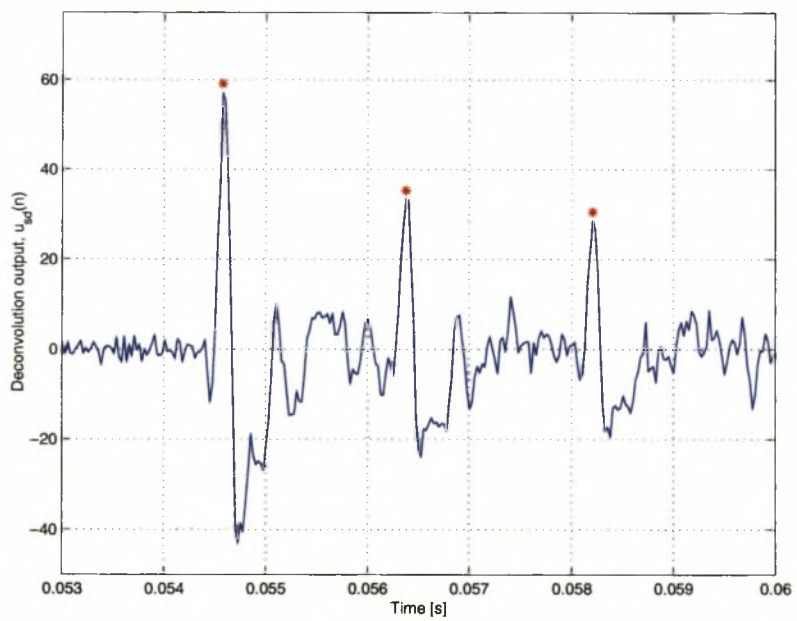

Figure 5.13: Three spikes in a time window $\Delta t = 3.6$ms were successfully located by the detector.

Other factors influencing the maximum rate of flow that can be processed are available processing power and the window length used to determine impact position (see Section 4.1).

Using a window length $N = 120$ samples to classify impact position provide accurate results. At a sampling rate $f_s = 40$kHz this corresponds to a flow rate of 330 particles per second.

5.8 Floating Point Operations

The necessary condition that the system performs on-line size distribution estimation puts a heavy constraint on the maximum rate of particle flow that can be dealt with. This is due to finite processing time that we have available. Processing requirements increase exponentially with increasing number of impacts observed on the bar.

Table 5.5 indicates the number of floating point operations (FLOPS) needed to perform different steps in the size estimation algorithm. Values indicated are calculated over a time period of 1 second for a sampling rate $f_s = 40$kHz and the number of particles 300 per second.

1 - Estimate spike temporal location	
Simple deconvolution	5.2×10^6
Impact event detection	4.3×10^6
2 - Impact position compensation	
Determine reflection coefficients (80,000 flops per impact)	24×10^6
Bayesian classifier (55,000 flops per impact)	16.5×10^6
3 - Estimate impulse amplitude	
MAP estimation (both vertical and horizontal)	12×10^6
Total number of FLOPS	$\mathbf{62 \times 10^6}$

Table 5.5: Number of floating point operations performed during 1 second for different stages of the algorithm. Values correspond to a sampling rate $f_s = 40$kHz with 300 particles per second.

The number of flops needed for Step 1 of Table 5.5 is independent of the number of particles impacting on the bar. Only the number of samples of data available per second influence the flops. Thus, it is only influenced by the sampling rate.

Steps 2 and 3 are dependent on the number of particles. More specifically, Step 2 has a

linear relation for the number of FLOPS to the number of particles.

The number of FLOPS needed for Step 3 increases exponentially with the number of particles. MAP estimation requires that data be windowed into windows of length N each. We use a window length of $N = 1000$. With a sampling rate $f_s = 40$kHz there are 40 windows per second, thus with 300 particles impacting per second there will be approximately $M = 8$ particles per window. The number of particles per window and the window length determine the number of FLOPS needed for MAP estimation. The number of FLOPS needed per window to perform MAP estimation for both channels is approximately given by

$$FLOPS_{\text{map}} = 4 \times [M^3 + NM^2 + NM]. \tag{5.6}$$

Figure 5.14 is a graph for the number of FLOPS vs. the number of impacts per window for a window length $N = 1000$. It can be seen that by doubling the number of particles to about 15 per window, the number of flops increases more than three times.

It was mentioned in Section 3.3.3.4 that the *Cholesky decomposition* may be used to efficiently solve the last step of MAP estimation, (3.38). However, this mainly contributes to the first term of (5.6). But since $N \gg M$, the M^3 term is relatively insignificant when compared to the total number of FLOPS. Therefore, utilisation of the *Cholesky decomposition* will only have a marginal improvement on performance.

The total number of 62×10^6 flops that have to be performed per second can be achieved using standard PC hardware that are available today. An Intel Pentium II running at 450MHz can sustain about 250×10^6 FLOPS per second doing 1-D FFT operations.

5.9 Sampling of Particulate Material

Sampling is the process whereby samples from the entire population are selected and investigated to draw inferences about population parameters [36]. The number of particles, N, used in the sample is termed the sample size. Clearly N has to be large enough so that

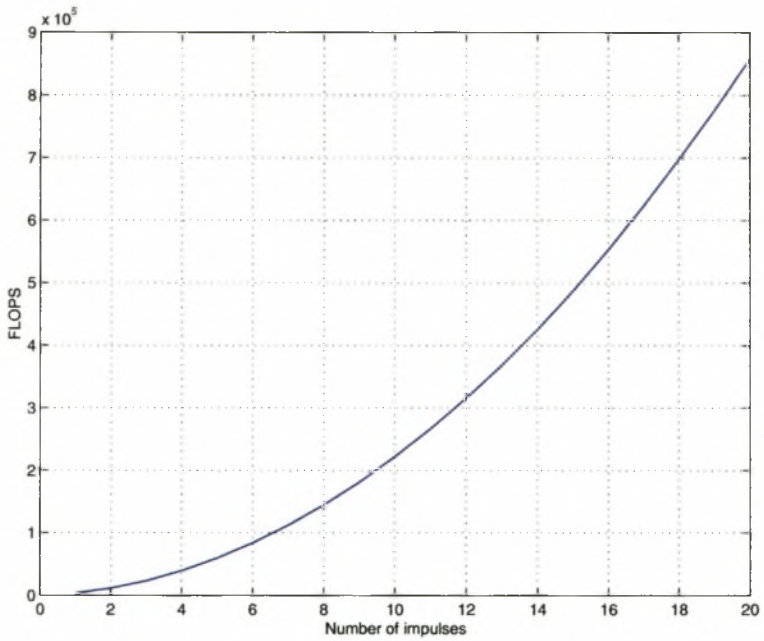

Figure 5.14: The number of FLOPS used for MAP estimation vs. the number of particles in the window for a window length $N = 1000$. The number of FLOPS increases exponentially with the number of particles in the window.

the sample is *representative* of the population. Also, samples should be drawn in such a way that there are no biases in the sample.

Most of the advantages of sampling are obvious [37]. It is cheaper to obtain information from a sample than from an entire population. Also more comprehensive data can be obtained. This is because a small sample may be thoroughly investigated whereas, for a large population, this may be impossible or too costly [37].

In mineral process plants, most automatic samplers operate by moving a collecting device, the cutter, through the material as it falls from a conveyor. Important aspects that need to be fulfilled in order to obtain an unbiased sample using automatic samplers are as follows [38]:

- The cutter has to move at a constant speed.
- A cutter that is too narrow in relation to the size of the largest particles in the mixture will not allow those large particles to pass freely into the cutter.

- Cutter velocities need not exceed a maximum. Gy [22] has established empirically that the safest policy is to restrict cutter velocities to 0.6 m/s.
- The edges defined as the cutting edges need to move at right angles to the stream to be sampled.

Because our acoustic sensor is a stationary bar, it does not have the sampling problems mentioned above. However, the bar performs sampling in space as will be described in the next paragraph. Because we work with a relatively low rate of particle flow (about 300 – 400 particles per second per sensor), it is assumed that the particle stream that will be used to estimate the population particle size is already sampled from the bulk. This "preprocessing" on the bulk is done prior to our sensor and will introduce a sampling error $\mathrm{SE}_{\mathrm{prior}}$. According to Gy [22], all stages of preparation are error-generating and add up to give the total error. The total sampling error SE is the sum of $\mathrm{SE}_{\mathrm{prior}}$ and the sampling error due the bar, $\mathrm{SE}_{\mathrm{bar}}$ [22]:

$$SE = \mathrm{SE}_{\mathrm{prior}} + \mathrm{SE}_{\mathrm{bar}}. \tag{5.7}$$

Because we cannot account for $\mathrm{SE}_{\mathrm{prior}}$, this section deals with specifying the influence of $\mathrm{SE}_{\mathrm{bar}}$.

Assuming we have a particle stream that has to be investigated to determine size characteristics, our sensor still performs additional sampling. Consider Figure 5.15 which is the top view of a conveyor belt and the round cantilever bar underneath it. With a conveyor belt width w_{cb} and bar diameter d_{b} it can be seen that the probability of particles impacting on the bar will be

$$P_{\mathrm{sample}} = \frac{d_{\mathrm{eff}}(r_b, r_p)}{w_{\mathrm{cb}}}, \tag{5.8}$$

where $d_{\mathrm{eff}}(r_b, r_p)$ is the effective width of the bar and is a function of the bar radius r_b and the particle radius r_p.

The result of this is that we have physical sampling in space. In Section 4.3 it was discussed

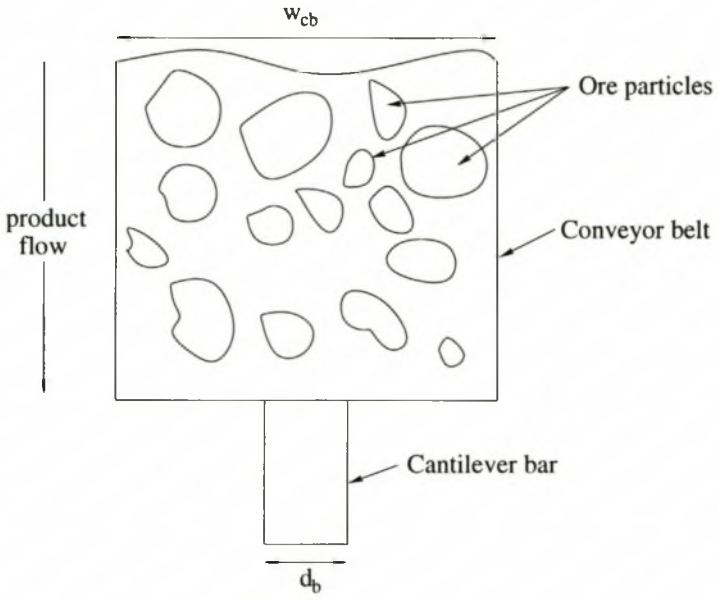

Figure 5.15: Top view of conveyor belt and cantilever bar underneath it.

how impact angles of up to 60° are valid. This means the effective diameter of the bar is more than the true diameter d_b. The concept of "effective diameter" is depicted in Figure 5.16 which is the front view of the round bar and particle at the moment of impact at an angle of impact $\theta = 60°$. The cross section of the bar has a radius r_b and the round particle has a radius r_p. Since we ignore impacts with $\theta > 60°$, the effective radius of the bar r_{eff} is given by

$$\begin{aligned} r_{\text{eff}} &= r_b \cos 30° + r_p \cos 30° + r_p, \\ &= (r_b + r_p) \cos 30° + r_p. \end{aligned} \tag{5.9}$$

Because particles can impact on either side of the bar, the effective diameter is twice the effective radius and is given by

$$d_{\text{eff}} = 2\left[(r_b + r_p) \cos 30° + r_p\right]. \tag{5.10}$$

The effective diameter d_{eff} is larger than the true bar diameter d_b and thus a bigger percentage of the width on the conveyor belt are covered by the bar. From (5.10) it is clear

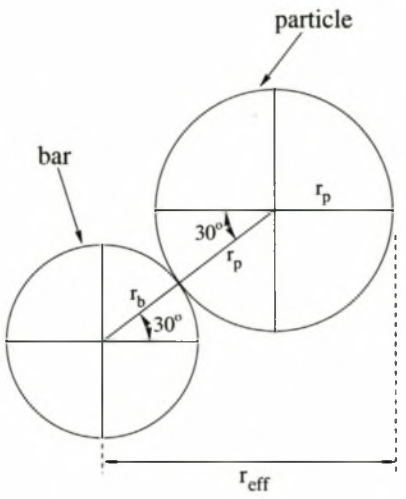

Figure 5.16: Front view of the round bar and particle at the moment of impact at an angle of impact $\theta = 60°$. The effective radius r_{eff} is indicated.

that the effective diameter is dependent on the size of the particle impacting on the bar. Since the particles on the belt are not of uniform size, we use the *a priori* particle size mean when determining $d_{\text{eff}}(r_b, r_p)$. Substituting d_{eff} from (5.10) into (5.8), results in

$$P_{\text{sample}} = \frac{2\left[(r_b + r_p)\cos 30° + r_p\right]}{w_{\text{cb}}}. \tag{5.11}$$

Equation (5.11) gives us the probability of particles on the feed to our sensor that will be investigated per sensor. By using N sensors horizontally across the width of the conveyor the percentage of particles that will be covered by sensors simply multiplies by N.

The use of multiple sensors ($N > 1$) may also be desirable if one considers that particle position across the width of the conveyor belt may be a function of particle size. This may be a result of a conveyor belt that is not perfectly horizontal. Vibrations can cause larger particles to tend to go to the one side whereas smaller particles might tend to be on the other. Size estimates from different sensors can be added together to obtain a size distribution estimate that is more representative of the bulk material.

The sampling method devised by Gy [22] is often used to calculate the size of sample necessary to give the required degree of accuracy [1]. The method takes into account the

particle size of the material, the content and degree of liberation of the minerals, and the particle shape. Gy's basic sample equation can be written as:

$$\frac{ML}{L-M} = \frac{Cd^3}{s^2}, \tag{5.12}$$

where M is the minimum weight of sample required, L is the gross weight of material to be sampled, C the sampling constant for the material to be sampled, d is the dimension of the largest pieces in the material to be sampled and s^2 is the variance of the statistical error committed by sampling. Normally M is small in relation to L and (5.12) approximates to

$$M = \frac{Cd^3}{s^2}. \tag{5.13}$$

The sampling constant C is specific to the material being sampled, taking into account the mineral content and its degree of liberation. How to determine the value of C for a specific situation can be found in [1, p 45].

Having knowledge about all the stages of sampling performed prior to the feeder to our sensor, we can use (5.11) and (5.13) to determine the minimum number of bars N we need to use to obtain a final sample that is within acceptable tolerance.

5.9.1 Biased Nature of Bar Sampling

From (5.10) it is clear that the effective width of the bar is bigger for large particles than small particles. Thus, size distribution estimates will be biased towards larger rocks since small particles are more likely to miss the bar and thus will be under represented. The equation describing how size estimates will be biased is given by (5.11) and can be rewritten as

$$P_{\text{sample}} = \frac{2(\cos 30^\circ + 1)r_p + 2\cos 30^\circ r_b}{w_{\text{cb}}}. \tag{5.14}$$

For a given conveyor width w_{cb} and bar radius r_b, (5.14) is a straight line given by

$$\Gamma_{\text{bias}}(r_p) = Ar_p + B, \tag{5.15}$$

where

$$\begin{aligned} A &= \frac{2(\cos 30^\circ + 1)}{w_{\text{cb}}}, \\ B &= \frac{2(\cos 30^\circ) r_b}{w_{\text{cb}}}. \end{aligned} \tag{5.16}$$

If we were estimating the radii of particles, (5.15) would be the appropriate function to scale the estimated size distribution in an attempt to remove the bias. But, what we measure and use as particle size, is the mass of particles. The relationship between particle mass and radius is given by

$$m = \frac{4}{3}\pi\rho r_p^3, \tag{5.17}$$

where m is the particle mass, ρ the particle density and r_p the radius. By solving for r_p we get

$$r_p = \sqrt[3]{\frac{3m}{4\pi\rho}}. \tag{5.18}$$

Substitute (5.18) into (5.15) to get

$$\begin{aligned} \Gamma_{\text{bias}}(m) &= A\sqrt[3]{\frac{3m}{4\pi\rho}} + B, \\ &= K\sqrt[3]{m} + B, \end{aligned} \tag{5.19}$$

with K a constant. From this it is clear that the sampling bias of the sensor has a cubed-root dependence on the particle mass. This relation is graphed in Figure 5.17 which shows (5.19) for typical rock particles in the 1–35g size range.

Using (5.19), it is easy to remove the sampling bias introduced by the sensor. Once the size distribution has been determined, it is scaled with the function in Figure 5.17.

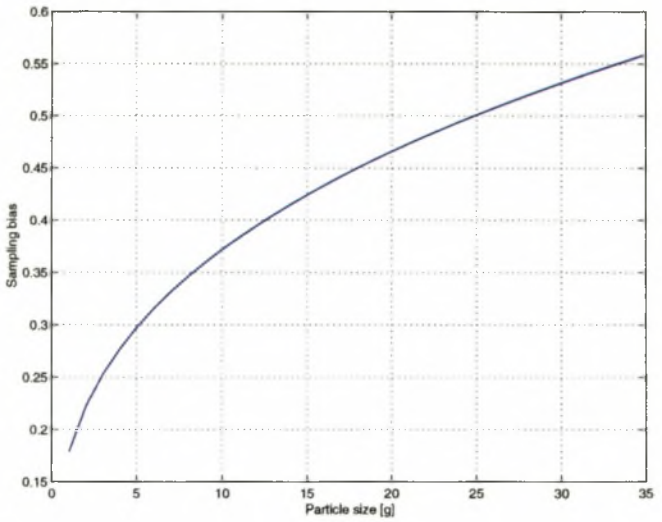

Figure 5.17: The sensor samples particles with a bias towards larger particles. It has a cubed-root dependence on particle mass.

5.10 Summary

A testing system consisting of a cantilever bar, a particle holding device and data acquisition hardware was implemented. Test particles used are various glass marbles of different sizes. Using the PHD accurate experimental data could be generated and thus the feasibility of the sensor as particle size distribution estimator could be determined.

The important conclusions that can be drawn from results presented in this chapter are summarised as follows:

- There is a linear relationship between particle mass and their estimated size amplitudes.
- The difference in height between the object particles fall from (conveyor belt) and the bar affects size estimates linearly.
- Compensation for impact position and angle of impact reduce variance in size estimates considerably. Square bar size estimates due to glancing blows are erratic. Angle compensation improves estimates somewhat, but overall the round bar pro-

vides better results.

- A rate of 300 to 400 particles hitting the bar per second can be dealt with.
- Multiple sensors can be used under each conveyor belt in order to obtain a size distribution estimate which is more representative.
- The sensor introduces a bias towards larger particles during sampling. Small particles are under represented. We remove this bias by scaling estimated size distributions to obtain an unbiased estimated size distribution.

Chapter 6

Conclusions

This work started with the realization of the need for ore particle size distribution measurement in a mineral processing environment. Since grinder efficiency is a function of the particle sizes being ground, size data can be used for control as to ensure that the plant operates optimally. Concepts relevant to particle size measurements were discussed. Specifically, we consider the mass of particles (or equivalently their volumes) as representative of their size. Also particle size data is conveniently presented using histograms.

There are various techniques for determining particle size distributions. These can be divided into two groups, namely on-line and off-line sensors. Because data could be used for control, on-line particle size monitoring is ideal.

We presented a new, acoustic sensor for monitoring particle size distributions on-line. As particles fall of a conveyor belt onto a metal cantilever bar, they cause it to vibrate. This acoustic signal due to bar vibrations, are picked up by strain gauges that are attached to the bar. Strain gauges configured in a full Wheatstone bridge, produce a small signal that is amplified with an instrumentation amplifier. Digital signal processing techniques are utilised to extract information regarding particle sizes contained within bar vibrations.

The sequence of particles impacting on the bar is modelled as an impulse train. Each impulse correspond to a particle impact and its amplitude is linearly related to the size of the particle. Thus, this sensor measures the *mass* of falling particles. The observed acoustic

signal consists of the convolution between the impulse train and the impulse response of the cantilever bar. Using the acoustic signal and information about the bar's response, we estimate the input impulse train. This is an inverse filtering problem where the effect of the bar and additive noise need to be removed from the observed signal in an attempt to reconstruct the input impulse train.

Simple deconvolution (performed by convolving the observed signal with the inverse system response), does not provide accurate impulse amplitude estimates. This situation is improved by quantifying *a priori* knowledge about sparsity of the input impulse train by a statistical model (Bernoulli-Gaussian) and using a maximum *a posteriori* (MAP) estimator for reconstruction.

It was found that the position where the particles impact on the bar, influence particle size estimates. This is clearly undesirable, since it introduces a large variance in particle size estimates due to the variation in impact position. There are two components to this positional problem. Firstly, impact position along the length of the bar plays a big role in size estimates. Secondly, glancing blows affect size estimates owing to the fact that only a portion of the energy in the particle is transferred to the bar. We compensate for these two undesirabilities by determining the exact position of particle impact on the bar and then scaling the initial size estimate as to remove the dependence on the position of impact.

The frequency characteristics of the bar is a function of the impact position along the length of the bar. This is because the amplitudes of the different modes of vibration change with impact position. If the bar is struck on a node (a zero) of a mode, that mode is not exited and thus will not be present in the bar vibration. The further a particle strikes the bar from a node, the greater the amplitude for that corresponding mode. By determining the reflection coefficients of the bar after each impact, a feature vector can be classified to estimate the impact position.

Particle size estimates are determined using the vertical component of bar vibrations. In order to get an indication of the angle of impact due to glancing blows, the horizontal component is also measured. Thus, each sensor produces a two component acoustic signal. An impact is modelled as the vector sum of the amplitudes of the impacts in the vertical

and horizontal directions. By determining the angle between these two components, it is possible to get an indication of the angle of impact and then compensate size estimates.

It has been shown that compensation reduces particle size estimate variances significantly.

The stationary bar sensor introduces a bias during sampling of particles in space. The bias is towards larger particles and smaller particles will be under represented. This biased nature of the bar was quantified with a mathematical model. Using this model, particle size estimate distributions are scaled to remove the inherent bias.

The results shown in the previous chapter demonstrate the sensor is capable of providing accurate size estimates under certain operating conditions. Flow rate of particles needs to be such that not more than 300–400 particles per second impact on the bar. This constrained is mainly due to limited processing time available. The overall flow rate of particles can be increased by using multiple sensors per conveyor belt. The use of multiple sensors also increase the representativeness of the sample by evaluating more particles and thus achieving a sample that is more representative.

It has been demonstrated that the use of an acoustic transducer is feasible for determining particle size distribution estimates. However, results presented were for data generated in a laboratory where we had complete control over the experiment. These were preliminary tests. In order to determine the real value of such a sensor, a mine test unit (MTU) will have to be implemented.

Bibliography

[1] B. Wills, *Mineral Processing Technology, Sixth Edition An Introduction to the Practical Aspects of Ore Treatment and Mineral Recovery.* Butterworth-Heinemann, 1997.

[2] K. Brownlee, *Industrial Experimentation.* Chemical Publishing Co., Inc, 1953.

[3] J. D. Stockham and E. G. Fochtman, *Particle Size Analysis.* Ann Arbor Science Publishers, Inc, 1977.

[4] T. Allen, *Particle Size Measurement, Third Edition.* Chapman and Hall, 1981.

[5] G. Stanley, "Considerations in the applications of autogenous milling," *Journal of the South African Institute of Mining and Metallurgy*, October 1975.

[6] R. C. Crida, *A Machine Vision Approach to Rock Fragmentation Analysis.* PhD thesis, University of Cape Town, 1995.

[7] R. R. Irani and C. F. Callis, *Particle Size: Measurement, Interpretation, and Application.* John Wiley and Sons, Inc., 1963.

[8] J. Astola and P. Kuosmanen, *Fundamentals of Nonlinear Digital Filtering.* New York: CRC Press, second ed., 1997.

[9] T. Lange, *Measurement of the Size Distribution of Rocks on a Conveyor Belt Using Machine Vision.* PhD thesis, University of the Witwatersrand, July 1990.

[10] E. B. Magrab, *Vibrations of elastic structural members.* Sijthoff and Noordhoff, 1979.

[11] P. M. Morse and K. U. Ingard, *Theoretical acoustics.* McGraw-Hill Book Company, 1968.

[12] K. F. Graff, *Wave motion in elastic solids.* Clarendon Press, Oxford, 1975.

[13] W. T. Thomson, *Vibration Theory and Applications.* Prentice-Hall, 1965.

[14] R. A. Serway, *Physics for Scientists and Engineers with Modern Physics.* Saunders College Publishing, 1992.

[15] A. D. Helfrick and W. D. Cooper, *Modern Electronic Instrumentation and Measurement Techniques.* Prentice-Hall International, Inc., 1990.

[16] K. Hoffmann, "Applying the Wheatstone Bridge, HBM Application notes," tech. rep., HBM, 1996.

[17] Hewlett-Packard Co., "Practical strain gage measurements, Application note 290-1," tech. rep., Hewlett-Packard Co., 1981.

[18] Analog Devices, *Amplifier Reference Manual*, 1992.

[19] K. L. Su, *Analog Filters*. Great Brittain: Chapman and Hall, 1996.

[20] C. Bellingan, "Near field, broad band array processing, theory and application," Master's thesis, University of Stellenbosch, November 1999.

[21] A. Rubini, "Dynamic kernels: Modularized device drivers," *Linux Journal*, vol. 23, pp. 10–17, March 1996.

[22] P. M. Gy, *Sampling of Particulate Materials Theory and Practice*. New York: Elsevier Scientific Publishing Company, second ed., 1982.

[23] J. M. Mendel, *Discrete-Techniques of Parameter Estimation*. New York, Marcel Dekker, 1973.

[24] J. Mendel, "Some modeling problems in reflection seismology," *IEEE ASSP Mag.*, vol. 3, pp. 4–17, 1986.

[25] K. F. Kaaresen, "Deconvolution of sparse spike trains by iterated window maximization," *IEEE Trans. Signal Processing*, vol. 45, no. 5, pp. 1173–1183, 1997.

[26] J. M. Mendel, *Optimal Seismic Deconvolution: An Estimation-Based Approach*. New York, Academic Press, 1983.

[27] J. G. Proakis and D. G. Manolakis, *Digital Signal Processing Principles, Algorithms, and Applications*. Prentice Hall, 3rd ed., 1996.

[28] S. M. Kay, *Modern Spectral Estimation: Theory and Application*. Prentice Hall, 1988.

[29] S. Haykin, *Adaptive Filter Theory, Third Edition*. Prentice-Hall International, Inc., 1996.

[30] H. Akaike, "A new look at the statistical model identification," *IEEE Trans. Automatic Control*, vol. AC-19, pp. 716–723, December 1974.

[31] J. Rissanen, "A universal prior for the integers and estimation by minimum description length," *Ann. Stat.*, vol. 11, pp. 417–431, 1983.

[32] P. Z. Peebles, *Probability, Random Variables, and Random Signal Principles*. McGraw-Hill, Inc., third ed., 1993.

[33] C.-Y. Chi and J. M. Mendel, "Viterbi algorithm detector for Bernoulli-Gaussian processes," *IEEE Trans. Acoust., Speech, Signal Processing*, vol. ASSP-33, pp. 511–519, June 1985.

[34] P. A. Devijver and J. Kittler, *Pattern Recognition: A Statistical Approach.* Prentice Hall International, 1982.

[35] L. Neiberg and D. Casasent, "Feature space trajectory (FST) classifier neural network," vol. 2353, pp. 276–292, Nov. 1994.

[36] M. Desu and D. Raghavarao, *Sample Size Methodology.* Academic Press, Inc., 1990.

[37] T. Yamane, *Elementary Sampling Theory.* Englewood Cliffs, N.J.: Prentice-Hall Inc., 1967.

[38] G. Lyman, *Sampling Particulate Materials – A Practical Introduction with Particular Emphasis on Coal and Mineral Processing Applications.* 17 Diosma Street, Bellbowrie, Queensland, Australia 4070, 1998.

Appendix A

Hardware Circuit Diagram

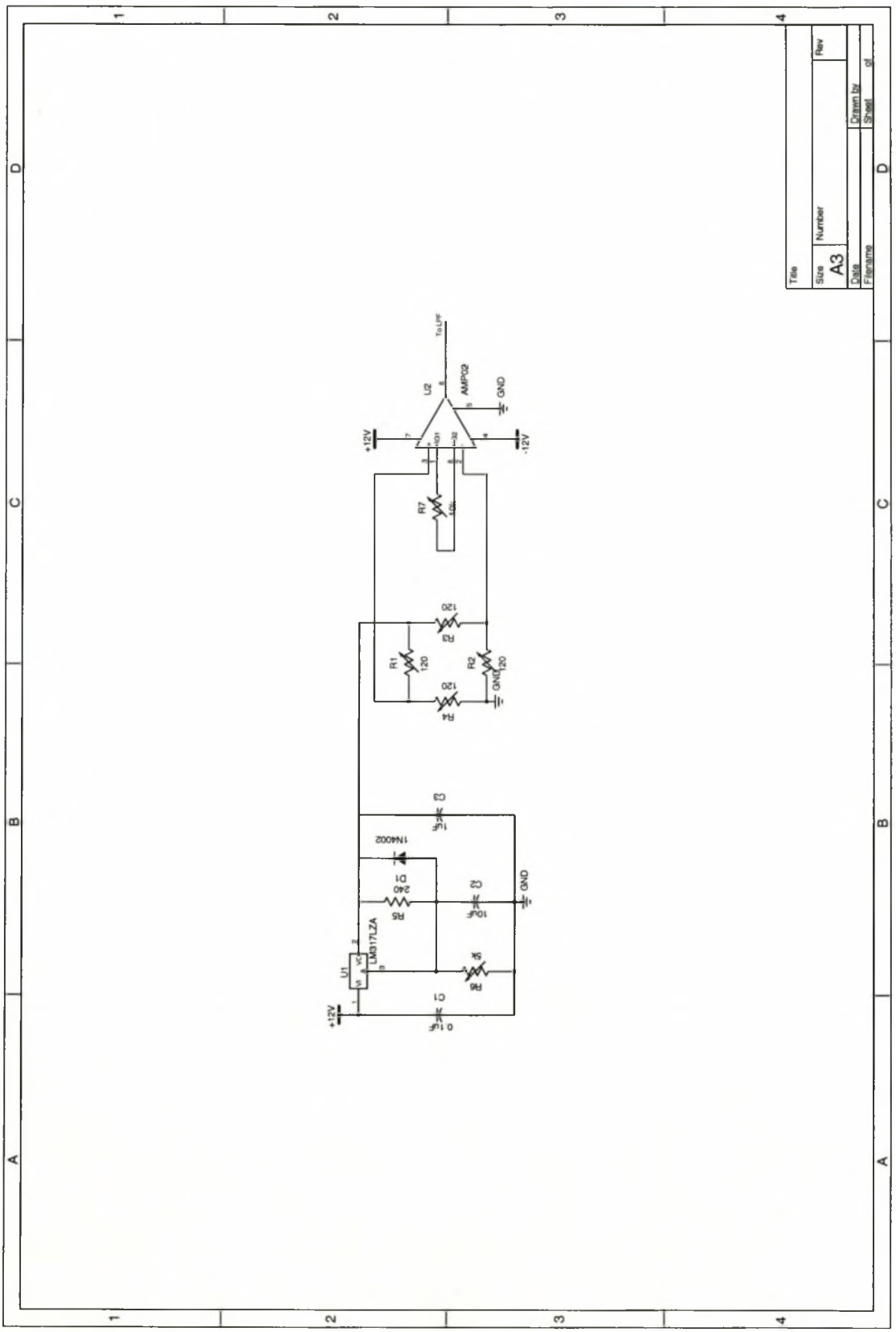

Figure A.1: Schematic diagram for instrumentation amplifier and Wheatstone bridge.

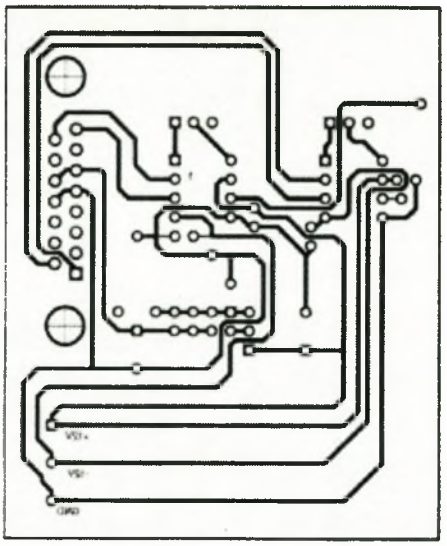

Figure A.2: PC board layout for instrumentation amplifier circuit.

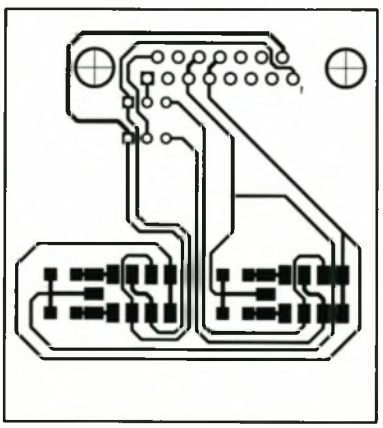

Figure A.3: Wheatstone bridge connections PC board layout.